Liquid Crystals From Linked Discs

by

Oliver Calderon

B.Sc. (Chemistry), Simon Fraser University, 2009

B.A.Sc. (Materials Engineering), University of Toronto, 2001

Thesis Submitted In Partial Fulfillment of the
Requirements for the Degree of
Master of Science

in the
Department of Chemistry
Faculty of Science

SIMON FRASER UNIVERSITY

Summer 2013

Approval

Name: **Oliver Calderon**

Degree: **Master of Science (Chemistry)**

Title of Thesis: ***Liquid Crystals From Linked Discs***

Examining Committee: **Chair:** Neil R. Branda
Professor, Department of Chemistry

Vance E. Williams
Senior Supervisor
Associate Professor, Department of Chemistry

Tim Storr
Supervisor
Assistant Professor, Department of Chemistry

Charles Walsby
Supervisor
Associate Professor, Department of Chemistry

Daniel B. Leznoff
Internal Examiner
Professor
Department of Chemistry

Date Defended/Approved: August 21, 2013

Partial Copyright Licence

Abstract

In the burgeoning field of organic semiconducting devices, molecules able to self-assemble into columnar liquid crystal phases are being investigated due to the unique directional conductivity of their structures. Knowledge of how molecule-level structural features impact the formation of the larger columnar assemblies is of considerable interest.

Studies of liquid crystal phases are already informally divided into shape categories, arising from molecules that are either rod-shaped or disc-shaped. Our interest lay in the middle ground where the basic disc-shape is elongated to a more elliptical one.

In pursuit of this goal, a series of rigid dimers were prepared by condensation of 3,3'-diaminobenzidine with various 2,3,6,7-tetralkyloxyphenanthrene-9,10-diones. Investigation revealed that these dimers assemble into a number of unusual phases, including nematic and columnar oblique mesophases.

In addition, a series of monomeric amide derivatives were synthesized by amidation of 2,3,6,7-Tetrakis(heptyloxy)dibenzo[a,c]phenazine-11-carboxylic acid. These molecules were found to spontaneously align in a homeotropic manner. They also supercooled into persistent glassy phases that preserved their alignment.

Keywords: liquid crystalline phases; self-assembly; rigidly linked covalent dimers; structure-property relationships; phasmids; organic electronic devices.

Dedication

To my family, the bedrock under the foundation.

Acknowledgements

Thanks to my senior supervisor Dr. Vance Williams for being patient and encouraging, I really appreciated your overflowing ideas and enthusiasm for science. Thanks also to my committee, Dr. Charles Walsby and Dr. Tim Storr, as well as my internal examiner Dr. Danny Leznoff for their help and advice.

Everyone in the Williams Lab past and present, especially Kevin Bozek and Emilie Voisin. Fellow students and friends in the department, especially Reagan Belan, Alisa Patterson, Brandy Kinkead, Michael Wong, Danielle Wilson, Tony Wu, and Amir Asidarad, Former colleagues, especially Chris Boyer (for many late night talks in the lab about sports and chemistry) and Chad Warford. You made it a pleasure to be a part of SFU Chemistry, both socially and scientifically.

Those who lent technical assistance, especially Dr. George Agnes for use of the MALDI-TOF; the indispensable help with NMR analysis from Mr. Colin Zhang and Dr. Andrew Lewis; Mr. Frank Haftbaradaran for elemental analysis; and Mr. Hongwen Chen for mass spectrometry.

Those who gave their support in other ways especially the Department office staff: Lynn Wood and Yolanda Broderick. I owe a special debt of gratitude for all the care and advocacy from the staff of Simon Fraser Health and Counselling, most notably Dr. Dianne Vosloo, Mr. Les Reimer, Dr. Erika Horwitz, and Dr. Kasim Al-Mashat.

Table of Contents

List of Tables

List of Figures

List of Schemes

Glossary (Acronyms, Abbreviations, and Symbols)

° C	Degrees Celsius
^{13}C	Carbon NMR
1D	One-Dimensional
^{1}H	Proton NMR
2D	Two-Dimensional
3D	Three-Dimensional
a	Lattice Constant (Å)
Å	Angstroms (1×10^{-9} m)
AcOH	Acetic Acid
b	Lattice Constant (Å)
BCC	Body-centered Cubic
BP	Boiling Point
c	Lattice Constant (Å)
Col	Columnar
Col_h	Columnar Hexagonal
Col_{hr}	Columnar Hexagonal-Rectangular Pseudophase
Col_{ob}	Columnar Oblique
Col_r	Columnar Rectangular
Col_{rh}	Columnar Rectangular-Hexagonal Pseudophase
Col_{square}	Columnar Square
Col_{tet}	Columnar Tetrahedral
Col_X	Unidentified Columnar Phase
Cr	Crystalline Solid
d	In the context of synthesis: Days
d	In the context of X-ray diffraction: Interplanar Spacing (Å)
DBP	Dibenzophenazine
DBPD	Dibenzophenazine Dimer
DCC	N,N'-Dicyclohexylcarbodiimide
DCM	Dichloromethane
d_{hkl}	Planar Spacing (Å) For Plane (hkl)
DMAP	Dimethylaminopyridine

DMF	dimethylformamide
DMSO	dimethylsulfoxide
DSC	Differential Scanning Calorimetry
EDCI	1-Ethyl-3-(3-dimethylaminopropyl)carbodiimide
eq	Molar Equivalents
EtOAc	Ethyl Acetate
EtOH	Ethanol
FCC	In the context of molecular structure: Face-centered Cubic
FCC	In the context of purification: Flash Column Chromatography
g	Grams
h	Hours
hkl	Miller Indices
HR-MS	High Resolution - Mass Spectrometry
I	Isotropic Liquid
IBX	O-iodoxybenzoic acid
J	Joules
K	Kelvin
kJ	Kilojoules
Kα	First "K" Shell Transition
L	Litres
LC	Liquid Crystal
LCD	Liquid Crystal Display
m	Mass (g)
MALDI-TOF	Matrix-Assisted Laser Desorption Ionization Time-of-Flight
MeOH	Methanol
mL	Millilitres
mmol	Millimoles
mol	Moles
MP	Melting Point
MS	Mass Spectrometry
MS-ESI	Mass Spectrometry - Electrospray Ionization
M_w	Molecular Weight (g / mol)
N	Nematic Phase

NaOAc	Sodium Acetate
NBu_4Br	TetraButylammonium Bromide
nm	Nanometers
OLED	Organic Light Emitting Diode
P	Primitive Cubic
POM	Polarized Optical Microscopy
ppm	Parts Per Million
PTFE	Polytetrafluroethylene
q	Heat (Joules)
R_0	Material Thermal Resistance (K/J)
RBF	Round Bottom Flask
SAXS	Small Angle X-ray Scattering
Sm	Smectic Phase
t	Time
T_c	Clearing Temperature (° C)
THF	Tetrahydrofuran
T_m	Melting Temperature (° C)
TOF	Time-Of-Flight
T_t	Transition Temperature (° C)
V	Volume (mL)
VT-XRD	Variable Temperature X-Ray Diffraction
W	Watts
WAXS	Wide Angle X-ray Scattering
X	Unidentified Phase
XRD	X-Ray Diffraction
α	Lattice Angle (°)
β	Lattice Angle (°)
γ	Lattice Angle (°)
Δ	Change
δ	Chemical Shift (ppm)
ΔG	Change in Gibbs Free Energy (Joules)
ΔH	Change in Enthalpy (J / mol)
ΔS	Change in Entropy (J mol-1 K-1)

ΔT	Change in Temperature (°)
θ	Angle in Degrees or Radians
λ	Wavelength (nm)

1. Introduction

1.1. Liquid Crystals

For most people, the three states of matter come readily to mind. Examples of solids, liquids and gases surround us and are a part of our everyday lives. We can think of these traditional states as a trade-off between order and fluidity. At one extreme of the range a crystalline solid is highly ordered – atoms and molecules create a regular periodic array in three dimensions and are often uniformly oriented in order to maximize favourable interactions. But, this high degree of ordering does not afford a crystalline solid the freedom to flow and take the shape of its container[1]. At the other extreme, liquids and gases are fluid precisely because they are extremely disordered. We tend to think of these states as being mutually exclusive; in fact, fluidity is one of the defining characteristics that traditionally separates solids from liquids or gases[2]. This is why liquid crystals are so fascinating; as their name suggests, they combine some of the ordering of a crystalline solid with the fluidity of a liquid[3].

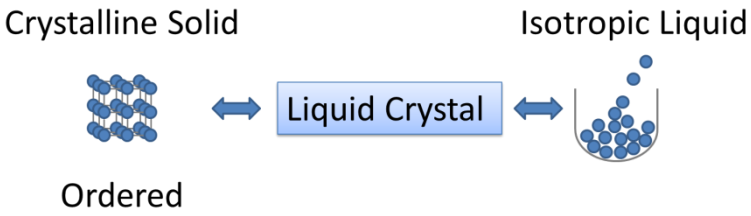

Figure 1.1: Relative ordering of common states of matter.

The fluidity of liquid crystals makes them well suited for applications such as switches that require an orientational change in response to an externally applied stimulus[4]. This property also separates them from glassy phases, whose order is 'frozen' in place. Liquid crystals also self-assemble into many interesting and convenient geometries or mesostructures. As noted above, they lack the bulk periodicity of a crystalline solid; therefore these liquid crystalline states, also known as mesophases,

form assemblies called “mesostructures” whose ordering is anisotropic; that is, their ordering varies along different axes of the material. As a result, bulk liquid crystals exhibit similarly anisotropic optical and electrical properties. Combined with their ability to flow, these properties make liquid crystals promising functional materials for applications such as organic electro-optical devices[5].

1.2. Ordering in Liquid Crystals

Ordering is an important concept when it comes to liquid crystal phases. Again, consider the difference between a crystalline solid and a liquid. Along each of the Cartesian axes, there is perfect positional ordering in a solid crystal grown under ideal conditions. If we pick any arbitrary direction to travel along we will encounter the same atoms in the same sequence and spaced at the same intervals. In the case of many real world applications, this repeating lattice is not limited to molecule-level distances (short-range) but extends to macroscopic distances (long-range) such as the size of an entire jet engine turbine blade[6]. We might consider this type of structure to have perfect, long-range ordering in all directions – it is the ‘maximum’ ordering possible.

In contrast, if we were to pick a direction to travel along in a liquid we would encounter no repeating patterns of atoms at all, let alone a regular spacing between them. This opposite extreme is considered to have no ordering whatsoever.

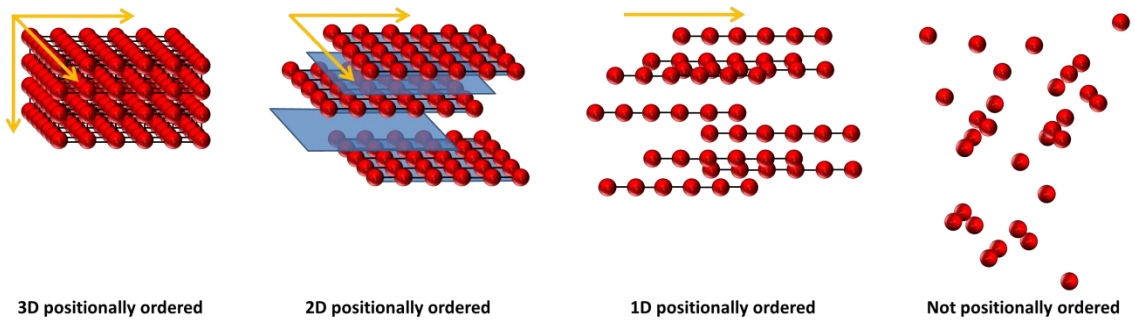

Figure 1.2: Decreasing levels of positional ordering, from left to right: 3-D crystalline lattice to completely disordered isotropic liquid.

Liquid crystals are semi-ordered structures in which there is a repeating and regular organization in some directions but not in others. For example, while a liquid

crystal may be ordered in a given direction, it is a lesser type of ordering compared to the positional ordering we are most familiar with. Directional or orientational ordering is a type of ordering common in liquid crystal phases that possesses more dimensional freedom than the fixed positions of molecules encountered in a crystal and can therefore be considered less ordered. Even in cases where positional ordering exists, it only exists in one out of the three dimensions and is often short-range rather than long-range.

The combination of short-range and mostly non-positional ordering is what makes the liquid crystal phase unique. Ordering of some kind is a prerequisite for a large number of physical properties from anisotropic absorbance to electrical conductivity. Lack of ordering is necessary to achieve fluidity, and fluidity is the dynamic quality that allows a material to react to its environment. It is also why the terms one-dimensional or two-dimensional liquids have been used to describe mesophases – the words evoke a substance that is disordered in one or two of the Cartesian axes.

1.3. Types of Liquid Crystals

Liquid crystal forming molecules, or “mesogens”, can be divided into two broad categories based on the forces driving their self-assembly. Lyotropic mesogens form liquid crystal phases upon interaction with solvent molecules. These lyotropic phases are therefore dependent on both the temperature and concentration of the mixture[7]. Although lyotropic phases are a large and important class of known liquid crystalline materials, they are outside the scope of this thesis and will not be discussed further.

In contrast, thermotropic mesogens do not require a solvent. Their liquid crystalline phases are induced by changes in temperature and are stable over definite ranges of temperature. This is an important distinction between a true liquid crystal phase and the coexistence of two phases, as one would encounter at a transition temperature; or a triple point where the solid, liquid and gaseous phases are present simultaneously. A given mesogen can exhibit multiple thermotropic liquid crystal phases, with more periodic arrangements tending to occur at lower temperatures and less regular arrangements at higher temperatures. The simplicity (compared to lyotropic LCs) of a single-component system and predictable temperature stability of thermotropic liquid

crystals is attractive for most applications. This thesis concentrates on thermotropic mesophases.

Most of the research on thermotropic liquid crystals to date can be classified according to the conceptual shape of the individual molecules. Due to their use in thin film displays, rod-shaped “calamitic” molecules are by far the most widely investigated. Recently there has been considerable interest in disc-shaped “discotic” liquid crystals due to their propensity to form into ordered columnar phases useful in organic semiconductors.

The shape classification is meaningful because certain liquid crystal phases are commonly associated with either disc-shaped molecules or rod-shaped molecules but are rarely observed for both shapes[8]. For example, nematic phases are relatively disordered and are almost exclusively seen in calamitic systems. Meanwhile, columnar phases are primarily formed from disc-shaped molecules due to their predisposition to stack on top of one another. Thus, there is a broad association between the shape of individual molecules and the resulting large-scale mesostructure, which is useful in the molecular design of such thermotropic LC phases[9].

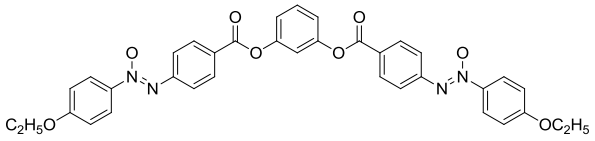

Bent-core (Banana)

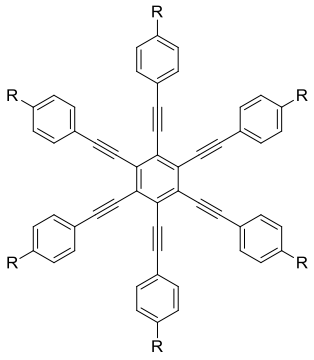

Star

Figure 1.3: Examples of alternative molecular shapes capable of mesophase formation.

There also exist a number of alternative molecular shapes such as the banana (or bent-core)[10,11], star[12,13], bowl[14,15], and branched[16,17] (dendrimeric) that may also give rise to liquid crystalline phases. Although notable for the effect their shapes have on the formation of interesting mesophase assemblies, they are not a primary focus of this thesis.

1.3.1. Calamitic (Rod-Shaped)

The two most common packing arrangements observed for calamitic systems are the nematic (N) and smectic (Sm) structures. A typical example of a calamitic liquid crystal is 5CB (4-cyano-4'-pentylbiphenyl), seen in Figure 1.4, which has an aromatic core consisting of a biphenyl core and perimeter substituents in positions that maximize the length of the molecule compared to its width. This is the basis of the idea that these types of molecules are 'rod' shaped – free rotation about the biphenyl bond as well as the C-C bonds in the alkyl chains should result in a circular cross-section. Thus, calamitic systems have one dimension that is much larger than the other two.

Recall that a crystal-like structure with positional order in three-dimensions would be unlikely to form a liquid crystal phase since it would lack dimensional freedom. The dominant packing arrangements of calamitic liquid crystals have imperfect ordering along at least two of the Cartesian axes.

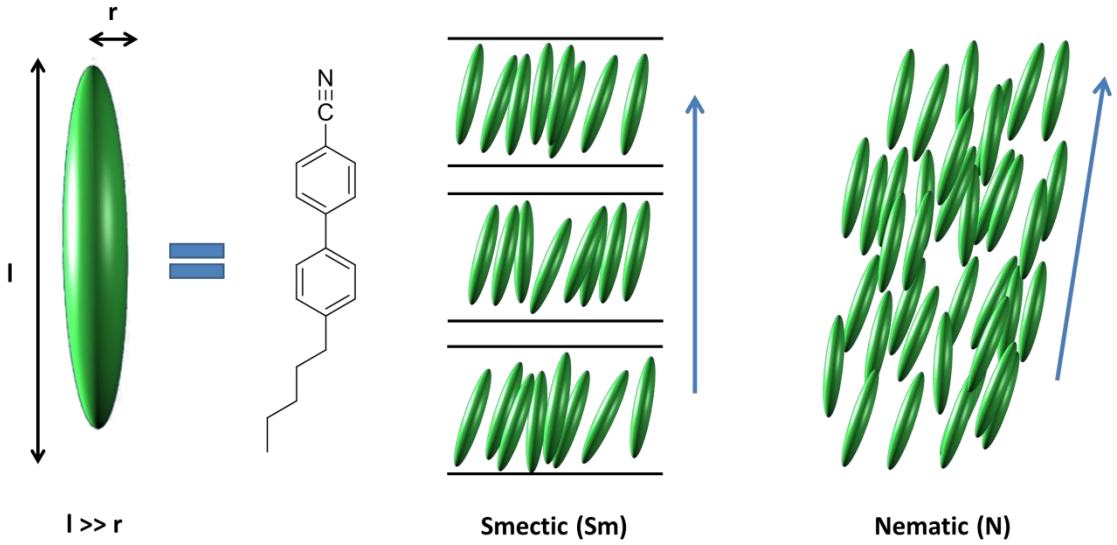

Figure 1.4: "Calamitic" or rod-shaped molecules and their associated mesostructures. Geometric ratio of length to radius defines a "rod-like" shape.

The more ordered smectic phases possess rough orientational order in which the molecules are aligned parallel to a director. The director is a vector used to denote the average orientation of the molecules comprising the liquid crystal phase, as illustrated by the blue arrows in Figure 1.4. Basically, each rod is pointed roughly in the same direction

as the director. Groups of molecules are arranged together into regularly spaced layers known as lamellae; note that these layers are the most ordered aspect of a smectic phase. As discussed earlier, not only is this semi-positional ordering imperfect compared to crystalline arrays in which the spacing and sequence of molecules is uniform in all three dimensions, it is also valid only for short-range domains. Within each smectic layer the component molecules are irregularly packed – it is only the layers themselves that are regularly spaced.

If the smectic phase can be considered to have two types of ordering, it is easy to see how the nematic phase can be said to be less ordered since it only has one; even that is merely orientational rather than positional. In a nematic phase, other than the long-axis of each of the molecules pointing in the same general direction (as described by the director vector), no positional ordering of any kind exists, i.e. molecules do not occupy a specific site in a periodic lattice. Further, the orientation is not ideal since the director represents the average direction of the molecules – each molecule is not perfectly aligned with its neighbours in any long range sense.

1.3.2. Discotic (Disc-Shaped)

Discotic mesogens were the chosen focus of this thesis.

In contrast to calamitics, discotic molecules are much shorter than they are wide. They typically consist of large aromatic cores (often comprised of fused aromatic ring systems) decorated with pendant alkyl groups. Disc-shaped molecules that form liquid crystal phases tend to self-assemble on top of one another to form loose columns. An analogous image would be a messy stack of dishes. Because they form such stacked column structures, their commonly observed phases – columnar rectangular or columnar hexagonal - are based on the different packing schemes preferred by the columns[18].

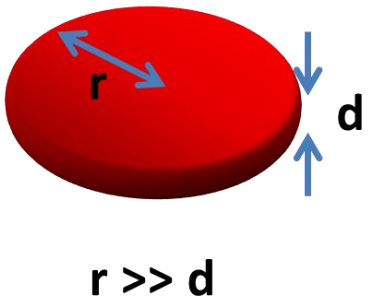

Figure 1.5: Schematic representation of relative aspect ratio of disc-shaped molecules. Radius is much larger than thickness (d).

Thus, columnar liquid crystal phases are usually regarded as being ordered in two dimensions since any regular arrangement of the columns will form a 2D lattice. However, such ordering is limited to the local domain. Compared to the calamitic mesophases described earlier, a typical discotic liquid crystal has three types of ordering but still falls short of the perfect periodicity of a crystalline solid. The vertical dimension is typically regarded as being disordered due to the imperfect stacking of discs within the columns. Because discs are arranged roughly perpendicular to the column's long axis, they can also be considered to have orientational ordering. Within the columns, some order may exist as illustrated in Figure 1.6 but fluctuations in orientation and position cause them to fall short of true three dimensional ordering.

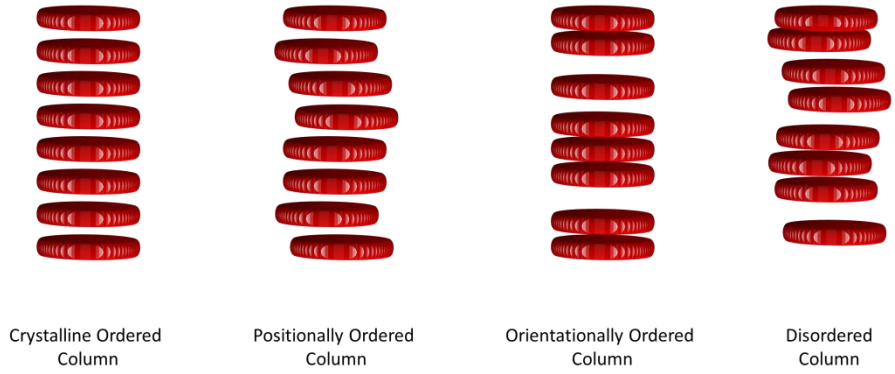

Figure 1.6: Examples of ordering present within columnar structures formed in liquid crystal phases.

The third degree of ordering comes from the packing of the assembled columns themselves (Figure 1.7). Columns packed in a hexagonal manner make up the most commonly observed mesophase by far. Less common are rectangular phases. Layered

phases of discotic molecules, while not unknown, are not common[19]. These phases can be distinguished from each other via the methods described below.

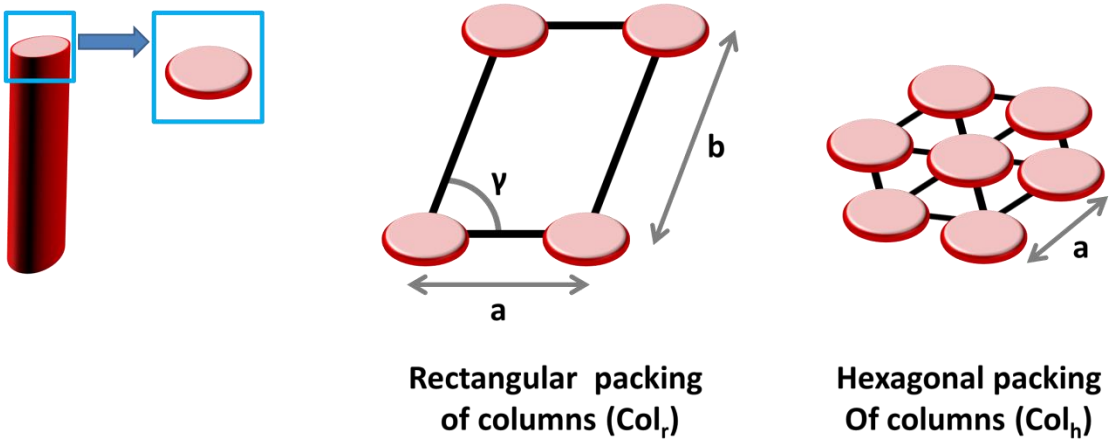

Figure 1.7: "Discotic" or disc-shaped mesogens and their associated liquid crystal phases. Schematic shows how disc self-assembles into columns.

An important consequence of the pillar-like assemblies formed in discotic mesophases is that they can be thought of as molecular 'wires' in which the semiconducting central core is surrounded by an insulating layer of alkyl chains. This is illustrated in Figure 1.8 in which the 'wire' (highlighted in blue) is surrounded by the 'insulation' (in red). This leads to a number of advantageous electric properties and has driven much of the recent investigation into discotic liquid crystal phases.

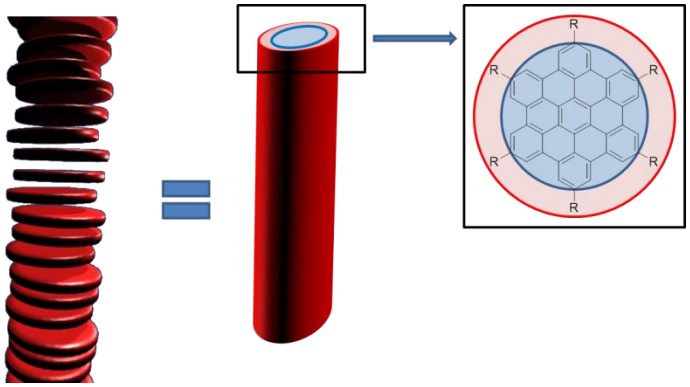

Figure 1.8: Orientationally ordered columnar phase as "'molecular wire": red insulating layer surrounding blue semiconducting core[20].

1.4. Applications

1.4.1. Applications of calamitic liquid crystals

Rod-shaped molecules that form liquid crystalline phases have changed display technology, enabling the production of ever larger and thinner screens. At this point there are more liquid crystal displays than people in the world.[21] These devices take advantage of the difference in the optical behaviour of nematic phases as they are aligned by applied electric fields to control the passage of light through pixel elements. Changing the alignment of the mesophase either blocks or allows the transmission of light from the source. The fluidity of the self-assembled structure allows it to respond to the external stimulus provided by the electric field, and this orientational response is the archetypical example of how a mesophase can be used as a switching device. A schematic of such a device is included in Figure 1.9, a detailed treatment of liquid crystal displays[22] is beyond the scope of this thesis and will not be discussed further.

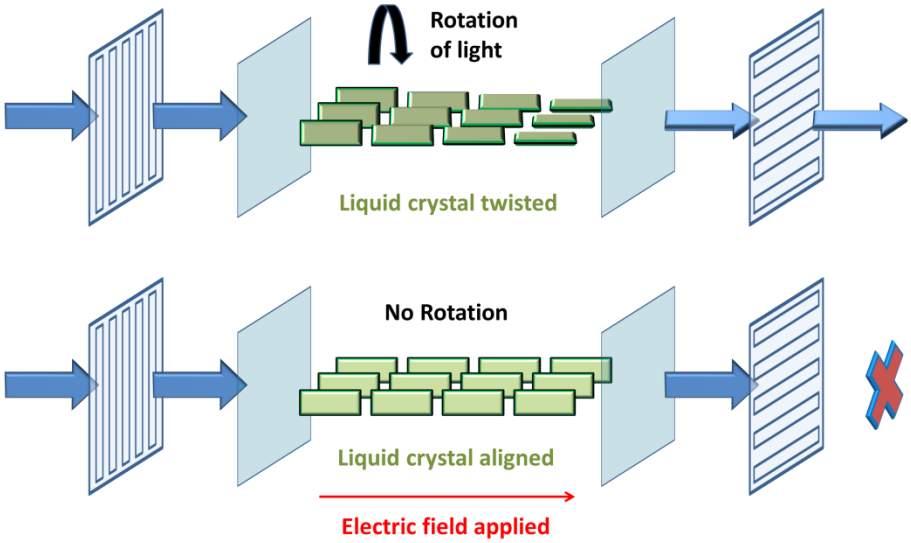

Figure 1.9: Simplified diagram of typical calamitic liquid crystal display (LCD). Normally each pixel is in the 'on' state and light from the backlight is allowed through. Alignment of the liquid crystal caused by application of an electric field prevents polarized light from passing through each pixel element, representing the 'off' state.

1.4.2. Applications of discotic liquid crystals

The aforementioned ability of discotic mesogens to form wire-like columnar phases makes them well suited for roles in organic semiconductors[23,24]. The central aromatic core provides high charge mobility while the peripheral alkyl 'insulation' allows for fairly efficient packing but without the formation of disadvantageous grain boundaries. For instance, charge mobility in perylene-cored mesophases have been reported to approach 1.3 $cm^2\ V^{-1}\ s^{-1}$, compared to $10^{-4}\ cm^2\ V^{-1}\ s^{-1}$ for semiconducting conjugated polymers[25].

Higher charge mobility is directly related to the structure of the columnar phase. The stacked discs are in an optimal position for increased overlap of their π-orbitals. Thus, electrical conductivity in the columnar architecture is anisotropic - much higher along the length of the column, which is also the direction that allows charge to be transferred from one aromatic core to another[26].

In addition to the generally superior magnitudes of both conductivity and mobility, the directionality of those properties in a columnar mesophase can be exploited to

optimize the requirements of the specific application. For example, most organic photovoltaics consist of bulk heterojunction arrangements in which there are significant domains of mixed n-type and p-type organic materials[27]. Interpenetrating domains of the donor and acceptor type materials create increased surface area for charge separation of excitons created by the photovoltaic effect.[28] After the charge carriers are separated, they must diffuse to their corresponding electrodes. This process is greatly facilitated by devices created with vertically stratified layers; these homeotropically aligned layers direct the carriers directly towards the metal junctions as opposed to the undirected transfer that occurs through a typical bulk film[29].

Another example of the advantages of static alignment of the columns are field-effect transistors and photovoltaics/OLEDs. In the case of thin films, this should allow charge transport to be highest in the desired direction – for example, parallel to the film for field effect transistors and perpendicular to the film for the optoelectronic devices. A common solution is to heat the material, align the mesophase and then cool it into a glassy phase that freezes the alignment. Thus, in addition to a liquid crystal phase whose morphology can be controlled, it is important to understand whether the potential mesogen will cool into a glassy phase as opposed to further ordering into a crystalline phase.

In several cases, surface treatment is used to attain the desired mesostructural alignment by rubbing[30,31], and/or coating with various substances such as PTFE[32] or polyimides[33]; recently studies have utilized a substrate[34] with a compatible surface. Often, this is insufficient and further thermomechanical processes such as annealing are required to minimize the amount of unwanted domains. It would be advantageous to design a liquid crystal phase that spontaneously aligned with substrate surfaces rather than relying on the extra cost and manufacturing complexity that comes with additional manipulation.

The packing of the self-assembled columns themselves can also result in a number of interesting mesostructures with features such as pores, channels and aligned domains that are suitable for gas storage[35,36,37], ionic conduction[38,39], and polarizing films[40,41] respectively.

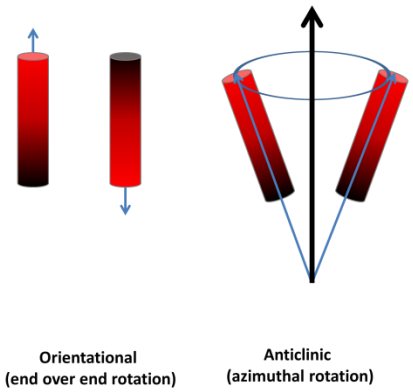

Figure 1.10: Types of reorientation in liquid crystals responding to external stimuli such as an electric field. Most devices currently rely on an end-over-end rotation (left) compared to a change in azimuthal angle relative to a central axis (right).

An exciting and recent development is the possibility of utilizing discotic mesogens as switches. The reorientation-based optical switching described previously for calamitic systems is unwieldy for much larger columnar structures that are often in well-packed arrays, unlike the practically disordered calamitic nematic phase. Figure 1.10 illustrates the common types of reorientation in such optical devices. Rotational re-orientation, also termed electroclinic-type switching is a viable geometric response to external stimulus for a closely packed material such as a discotic columnar mesophase[42]. This has been demonstrated quite recently by Takezoe[43], and offers the possibility of efficient magnetic, electrical or optical switches created with discotic mesogens.

Despite the promising potential of discotic liquid crystals as organic semiconductors, to date they have only been commercially deployed as optical compensation layers that serve to increase the viewing angle of traditional LCDs[44]. Ironically, these applications require the unusually disordered discotic nematic phase and not the columnar assemblies which normally furnish discotic liquid crystal phases with their desirable conductivity, alignment and morphology.

Finally, like most organic materials discotic liquid crystals provide unique advantages compared to their inorganic semiconducting counterpart, including relatively low cost, low-temperature processability and flexibility.

1.5. Characterization of Liquid Crystals

Within the field, when identifying a liquid crystalline phase, a triumvirate of characterization techniques is employed: POM, XRD, and DSC. Due to the unusual nature of liquid crystals, we must rely on the corroboration of all of these methods in order to confidently identify a suspected mesophase. Fortunately, the strengths and weaknesses of each technique complement one another. Each method will be discussed briefly.

1.5.1. Polarized Optical Microscopy

Polarized Optical Microscopy (POM) is used to qualitatively test for the presence of two important characteristics of liquid crystals: order and fluidity. Again, liquid crystals are often referred to as 1D or 2D liquids; that is, they are ordered along one or two orthogonal axes and disordered along the remaining directions. Therefore the structural features of liquid crystal phases tend to be highly anisotropic – that is, dependent on direction within the material. Compare this to common isotropic liquids, which are disordered along all of the Cartesian axes because of the constant random motion of the molecules. The refractive index of a material is the ratio of the speed of light in that material to that in a vacuum. Light propagating through an anisotropic material will have a different refractive index depending on its direction of travel through the material. Orientations with higher packing density and higher polarizabilities should refract light more strongly due to the relationship between bulk polarization (α) and index of refraction as described by the Lorentz-Lorentz equation.

Equation 1.1

$$n_{xx} = \sqrt{\frac{1 + 2\left[\alpha_{xx}\rho_{xx}\left(\frac{N_A}{3M}\right)\right]}{1 - 2\left[\alpha_{xx}\rho_{xx}\left(\frac{N_A}{3M}\right)\right]}}$$

Materials with at least two different direction dependent indices of refraction are called birefringent. Light can be represented by a two-dimensional tensor propagating in a direction that is not parallel to the optical axes. A birefringent material will refract light differently along the x and y directions – thus the x and y components of the light vector

will be affected differently. The upshot of this situation is that light travelling through a birefringent material will experience refraction, even if the incident wave is normal to the surface.

As mentioned previously, by definition liquid crystal phases possess non-three dimensional partial ordering, so both their density and polarizability are anisotropic. Birefringence is therefore a typical quality of mesophases, so its existence in a sample is a strong indicator of the presence of a liquid crystal. In addition, since birefringence is dependent on ordering, the textures found under crossed polarizers can provide evidence of the type of mesophase present. Therefore, polarized optical microscopy is an important tool in the characterization of liquid crystal phases.

In the specific case of the polarized optical microscope, the method of operation is nearly identical to a conventional optical microscope in which light from a source is transmitted through a sample and observed through a system of lenses. The important difference is that one polarizing filter is placed between the source and sample, and another between the sample and lens. The first filter plane linearly polarizes the incident light, and can be adjusted to various angles with respect to the second polarizer. If the two polarizers are set at right angles to each other, light from the source will not pass through the second polarizer and a uniformly dark field will be observed. The introduction of an optically isotropic sample between the polarizers will have no effect since it does not change the light's polarization.

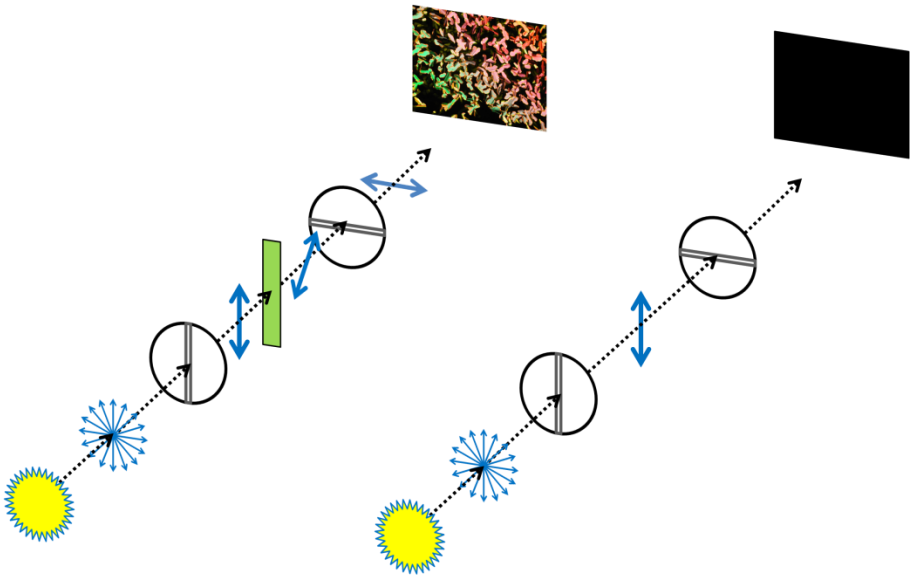

Figure 1.11: Schematic representation of a polarized optical microscopy (POM) apparatus. Left: light from the source is linearly polarized and then that polarization is shifted by a birefringent material (green box). This allows light to pass through the second polarizer and an image is observed. Right: light from the source is linearly polarized and cannot pass through the second polarizer.

In the case of a birefringent sample, the initial polarization of light from the source will be changed as it passes through the material; the anisotropy of the material 'twists' the polarization. Some of the polarized light can now pass through the second polarizer. Going forward, pictures of the light transmitted through the polarizers will be referred to as photomicrographs.

Due to the random orientation of individual domains within the liquid crystal phase as well as the wavelength dependence of refraction, optical textures will be observed instead of a completely black field. The exact distribution, colour and intensity of such textures in a particular photomicrograph are unpredictable. However, specific textural patterns such as brushes or dendrites have been empirically correlated with certain mesophases.

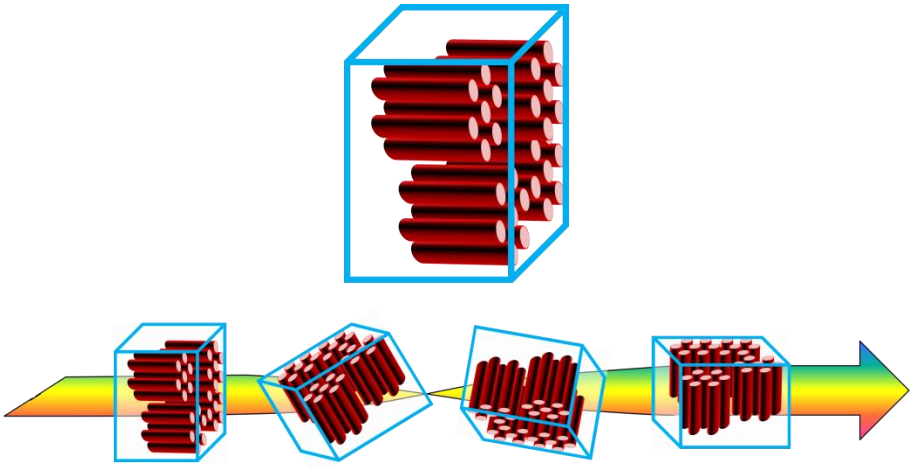

Figure 1.12: Schematic representation of aligned domains in a liquid crystal. Top: the domain (blue cube) may consist of orientationally aligned columns. Bottom: a random distribution of such aligned domains will still diffract light due to the presence of all types of domain orientations.

As mentioned previously, specific self-assembled structures are commonly associated with certain types of mesogen. These structures have characteristic POM textures that reflect their underlying microscopic arrangement. Nematic phases, usually formed by rod-shaped molecules, have a characteristic schlieren texture. Disc shaped molecules tend to self-assemble into columns and the textures observed are often indicative of how those columns are packed together. For example, branched (or dendritic) structures are often seen in photomicrographs of columnar phases. Dendritic structures with obvious six-fold 'snowflake' symmetry and non-orthogonal branching are seen for columnar hexagonal phases. A rectangular packing of the columns also gives rise to dendritic textures, but with four-fold symmetry and orthogonal branching (Figure 1.13). Note that the inter-branch angle for these textures is orthogonal for the rectangular (360° / 4) and 60° for the hexagonal texture (360° / 6).

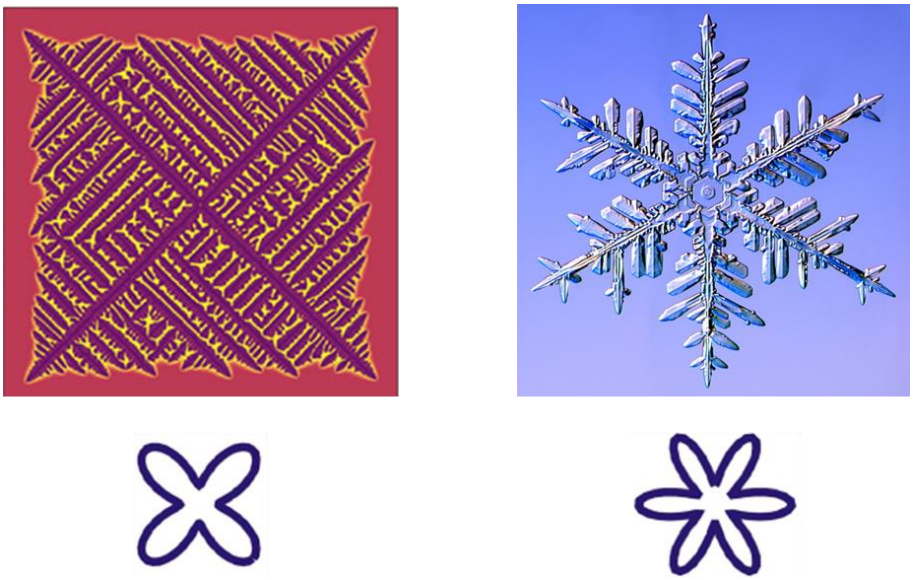

Figure 1.13: Examples of dendritic growth patterns for PEO[45] (polyethylene glycol, left) with a fourfold symmetry and snow[46] (right) with six fold symmetry.

Since the sample is usually prepared as a thin film sandwiched between a glass microscope slide and a cover slip, POM also provides information on the fluidity of the material. The cover slip can be subjected to pressure and the change (if any) in the texture can be observed. In a fluid sample, the pressure should reorient random domains within the liquid crystal phase, causing different domains to be revealed and others to be hidden as they reorient into or out of orientations that would create a black field. A change in colour is not uncommon due to the wavelength dependence of birefringence. If the material is fluid, removing the pressure should result in another reorientation. If this reorientation is not observed, the material may be plastic or crystalline instead of fluid. This test is vital since many materials are birefringent – it is the combination of fluidity and birefringence that distinguishes liquid crystal phases from the rest.

POM is also able to identify another property of liquid crystals: their alignment. Some mesostructures display a marked tendency to align with their underlying substrate in either a parallel (planar alignment) or perpendicular (homeotropic alignment) fashion. Each of these alignments is important for particular applications.

The test for fluidity may also reveal whether alignment is present in a liquid crystal phase. Before applying pressure, a homeotropically aligned sample shows up as a uniform field with no apparent texture. This is because there is little to no birefringence if all the molecules are aligned and light travels down the long axis of the columns. As pressure is applied, texture should appear in the microscope field since the aligned domains are being tilted. This indicates that the molecules are homeotropically aligned with the substrate. For most cases, releasing pressure should result in a return to the aligned state as evidenced by the reappearance of the optically uniform field.

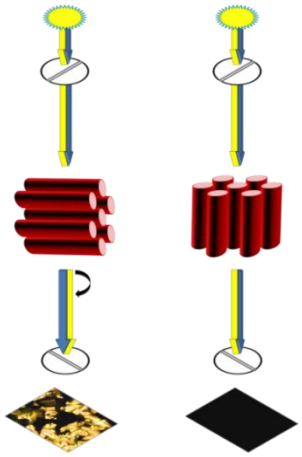

Figure 1.14: Orientation effects of columnar mesophases. Left: normal POM image observed due to birefringence. Right: No texture observed when looking down along the long axis of the columns.

Finally, uncrossing the polarizers often reveals the borders of liquid crystal domains. The presence of such domains are not particularly useful for un-aligned samples since their textures will be apparent under crossed polarizers. However for aligned samples where initial visual inspection will appear to be featureless it is often useful to observe that fluid domains have indeed been formed.

1.5.2. Differential Scanning Calorimetry

Calorimetry in general measures the change in heat of a compound due to a physical or chemical change. In the case of liquid crystals, it is used to identify the temperature and enthalpy of phase transitions. With increasing temperature, transitions are typically observed for transformations between the crystalline, liquid crystal, and isotropic liquid states.

The term ‘differential’ is the key to understanding the underlying mechanism of DSC – these calorimeters measure the difference between the thermal state of an empty reference pan and a pan containing the sample to be analyzed. Data from the instrument is applied to the heat equation (Equation 1.2) , where R_0 is the fixed resistance of the system. Conventional calorimetric instruments measure this heat differential in one of two ways: heat flux or power compensation.

Equation 1.2

$$q = \left(\frac{-\Delta T}{R_0}\right)$$

Power compensation based approaches separate the sample and reference into their own thermally isolated calorimeter chamber, complete with thermocouple and furnace. The amount of power required to raise the temperature of each pan is recorded and a feedback loop is created that increases or decreases power to either the sample, reference, or both as required to maintain the pans at the same temperature. This enables both endo- or exothermic events to be measured by the relative amount of power added or removed from the sample pan (Figure 1.15). This method is considered by some to be thermodynamically ‘pure’ since it directly measures the amount of energy flowing into or out of the sample. The major advantage of such systems is that a direct measurement of power gives higher resolution. In addition, independent calorimeters allow for higher heating and cooling rates.

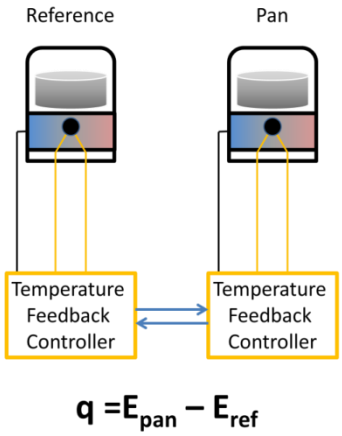

Figure 1.15: Schematic representation of power compensation DSC instrument. Each pan has its own heater, furnace and feedback controller that measures the power supplied to the sample in reference to the amount of power supplied to the reference pan.

In heat flux instruments, both reference and sample pans are enclosed in a single furnace. A path is created along which the heat will flow – from the ambient temperature within the furnace, through the pan (and sample if present) and finally through an underlying material of known thermal conductivity to a thermocouple. Each pan has its own thermocouple, whose readings are used to measure the difference in temperature between the reference and sample (Figure 1.16). This temperature difference is recorded by the machine and converted to energy via the heat flow equation. The advantages offered by the heat-flux method route are increased baseline stability and cell durability.

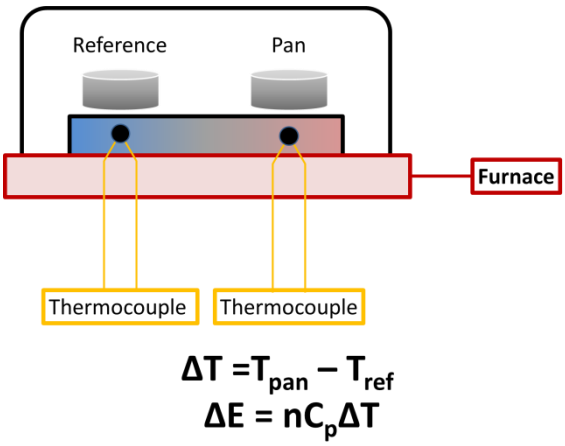

Figure 1.16: Schematic diagram of heat flux DSC controller. Reference and sample pans are in the same furnace and the temperature difference is used to calculated the heat exchanged.

Curves in a DSC trace obtained from heating a sample are referred to as endotherms since heat must flow into the pan. Conversely, curves produced on cooling are called exotherms since heat is typically evolved from phase transitions induced by lowering the temperature. In a modern instrument, the vertical orientation of an endotherm or exotherm is arbitrary and can be set to either up or down. All DSC traces presented in this thesis use a convention in which endotherms point down and exotherms point up, as illustrated in Figure 1.17.

Assuming equilibrium (i.e. non-kinetic) phase transitions, the obtained values should be independent of scan rate. However, DSC data can be highly scan rate dependent[47], but this can be alleviated with proper calibration of the instrument at the anticipated scan rates. In any case, DSC data is typically obtained at various scan rates to determine if such dependence is applicable.

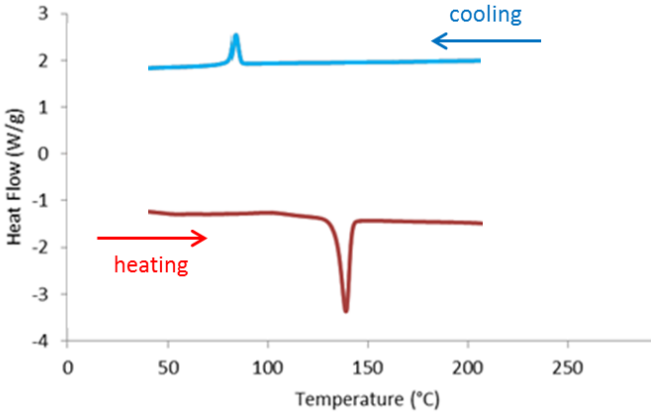

Figure 1.17: Typical DSC trace showing endotherms (red trace) on heating and exotherms (blue trace) on cooling. Change in enthalpy can be determined by integrating the area under the curve.

As previously mentioned, the presence of an extra peak between the crystalline solid to isotropic liquid transition strongly suggests the presence of a liquid crystal phase. The range and absolute temperatures of these two transitions provide important information. The temperature at which the crystalline phase transforms into a liquid crystalline phase is called the melting temperature (T_m) since the more ordered structure is 'melting' into the relatively disordered mesophase. The phase transition from mesogen to isotropic liquid is termed the clearing transition (T_c) since the visually opaque mesophase 'clears' into the transparent, optically isotropic liquid phase.

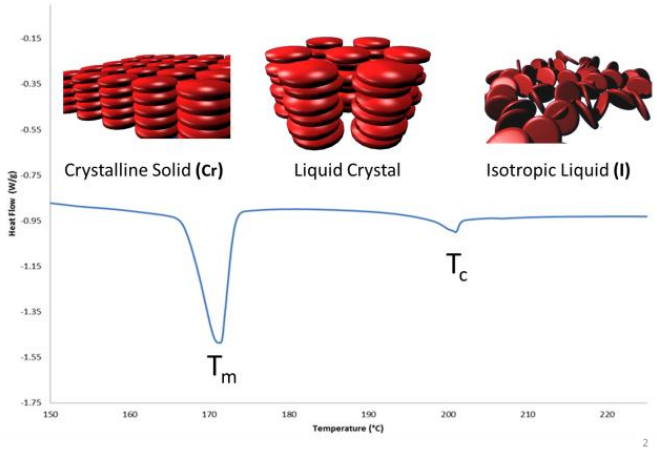

Figure 1.18: Example of DSC trace produced on heating. T_m is the melting temperature marking the transition from a crystalline solid to a liquid crystal. A peak with a much smaller enthalpy is observed at the clearing temperature (T_c) when the mesophases 'clears' into an isotropic liquid.

The enthalpy of a given transition is calculated from the area under the peak, giving a quantitative measure of the associative interactions that drive the self-assembly of the phase under transition. For example, large enthalpies (30 – 50 kJ/mol) are associated with a transition from a highly ordered substance like a crystalline solid to a disordered substance such as an isotropic liquid. For a more subtly ordered structure like a columnar liquid crystal, the enthalpy of isotropization is much smaller (4 – 6 kJ/mol). Enthalpies associated with even smaller changes in order such as nematic-to-liquid (1 - 2 kJ/mol) or mesophase-to-mesophase transitions are accompanied by proportionally smaller phase change enthalpies (<1 kJ/mol).

Equation 1.3

$$\Delta G = \Delta H - T\,\Delta S$$

The amount of ordering can be further analyzed using the change in entropy, which is determined using the Gibb's free energy equation and the experimentally determined enthalpy and transition temperature. This is especially important for a liquid crystal phase since the change in entropy, especially at the transition from crystal to liquid crystal, is often the dominant term in the equation.

1.5.3. Variable Temperature X-Ray Diffraction

X-ray diffraction is effective at determining the long-range ordering of a material. Since the studies in this thesis concern thermotropic liquid crystals, it is necessary to determine the molecular structure at higher temperatures where the liquid crystal phase may be stable. Thus, variable temperature X-ray diffraction (VT-XRD) allows us to determine the limited ordering present in a mesophase.

Determining structure is accomplished by taking advantage of Bragg's Law (Equation 1.4).

Equation 1.4

$$n\lambda = 2dsin\theta$$

A beam of monochromatic X-rays is produced from a source (usually copper, λ = 1.5418 Å) and focused through a graphite collimator onto the desired target. X-rays striking the sample at a given angle will be diffracted by each layer of the structure. The Bragg equation tells us that constructive interference will result if the Bragg parameters of angle (θ) and layer spacing (d) are proportional to an even number multiple of the X-ray wavelength. This is best understood by considering a periodic 2D lattice, as in Figure 1.19.

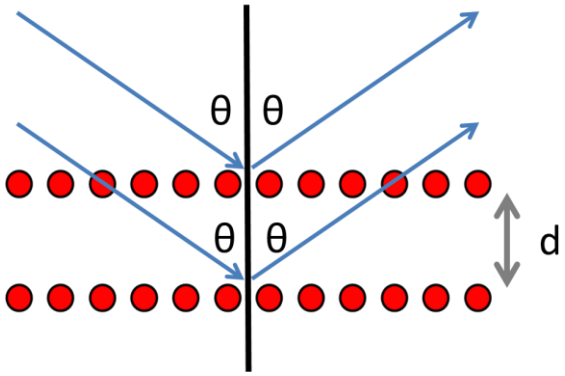

Figure 1.19: Diffraction of incident waves according to Bragg's Law.

This simplistic model is sufficient to understand how an incident beam could be scattered by 2θ, also referred to as the Bragg angle. However, in practice materials are three-dimensional. The direction of travel through the material will determine the types of

planes the X-ray beam will encounter. This is evident even in the simplified model, as shown in Figure 1.20, in which some of more commonly encountered planes are illustrated.

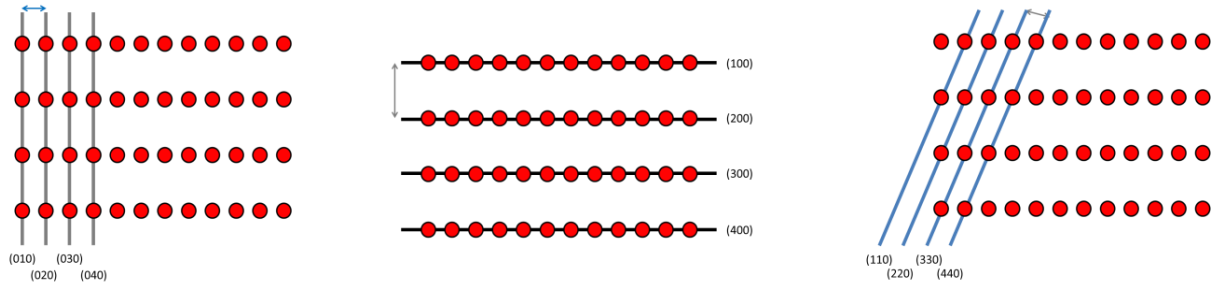

Figure 1.20: Commonly encountered Miller indices for a 2-D periodic lattice.

Miller indices are a convenient notation system used to distinguish one set of planes from another. The Miller Indices of a given plane of atoms or molecules is a 'normalized' version of what is essentially a simple Cartesian coordinate system. The columnar mesostructures that this thesis is primarily concerned with tend to aggregate into structures that are essentially two dimensional so the third numeral can be omitted.

The characterization of mesomorphic substances is considered to be a powder method since the sample should contain a statistical distribution of all possible random orientations of its liquid crystal domains. In a powder method, it is expected that X-rays should encounter every orientation that results in constructive Bragg interference. The end result is that a given set of planes scatters X-rays to produce a diffraction ring. These rings are integrated to give their positions in terms of 2θ, and the resulting total pattern can then be related to distance using Bragg's Law (Figure 1.21).

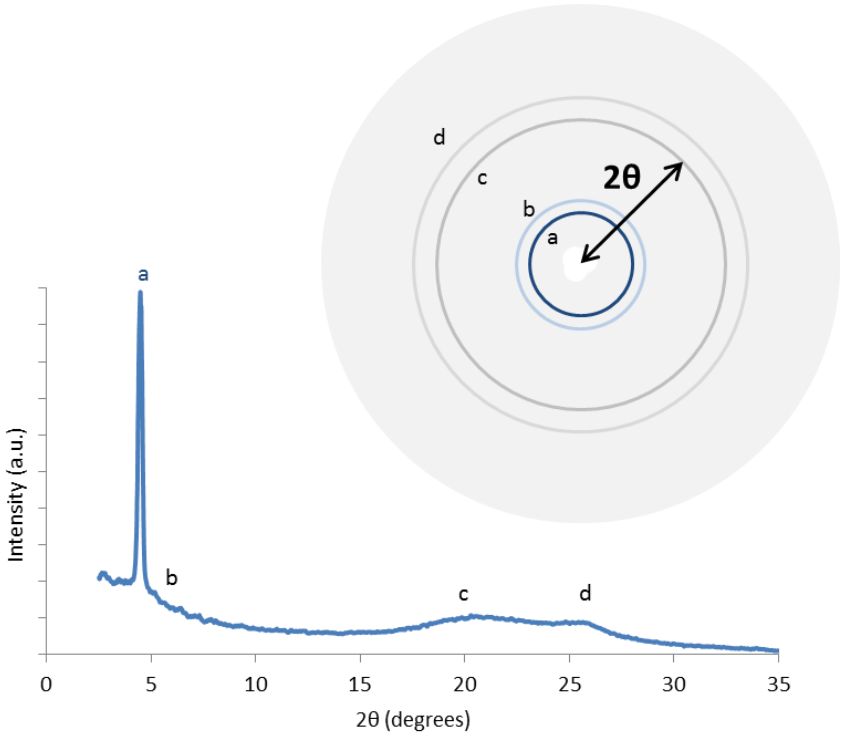

Figure 1.21: Sample XRD diffraction pattern and resulting trace for a typical columnar hexagonal liquid crystal.

Due to the limited ordering present in most mesophases, indexing the obtained peaks to a particular packing scheme is more difficult than for inorganic samples. For example, reports of typical columnar hexagonal phases often depend on only two peaks ((100) and (110)) to identify the packing; with sufficient corroborating evidence it is generally accepted that one peak is sufficient. Despite this inherent deficiency in data, there is a substantial body of peak patterns that have been empirically correlated to the typical mesophases discussed in the previous section.

Smectic phases of rod-shaped liquid crystals are easily identified by the repeating arrangement of their lamellae, which results in evenly spaced rings in the diffractogram corresponding to the (00n) planes created by layers. Nematic phases are not usually analyzed by XRD due to their inherent lack of ordering.

For columnar phases arising from disc-shaped molecules, the packing of the columns is most often hexagonal. XRD patterns for this hexagonal (Col_h) arrangement often consists of a sharp (100) peak followed by the broader and less intense peak

corresponding to the (110) plane. Well defined examples may also give rise to a (200) peak. Liquid crystal phases with rectangular (Col_r) packing usually have diffractograms consisting of two peaks of equal intensity that represent the (110) and (200) peaks.

Two distinguishing features often associated with the formation of a mesophase are broad peaks at high angles centering around 3.5 Å and 4.5 Å. These correspond, respectively, to the π- π stacking and alkyl halo components common to liquid crystal phases.

In addition to obtaining information as to the unit cell parameters of the structure of the mesophase, the relative sharpness of each peak can provide a measure of the amount of ordering in the mesostructure. Sharper peaks suggest a highly ordered arrangement, and sharper π- π stacking and alkyl halo peaks usually correspond to a greater degree of each in the overall structure. These latter, high-angle peaks (for disordered structures) are often too broad to observe.

In this work, variable temperatures were attained using a capillary furnace developed previously in the Williams group[48]. In this configuration the liquid crystal is placed in a capillary that is positioned in close proximity to two heating elements. Temperature was controlled and maintained using a feedback system consisting of a thermocouple placed slightly above the capillary and a voltage controller connected to the furnace.

1.5.4. Liquid Crystal Phase Identification

As mentioned at the outset, proper identification of a mesophase requires the use of XRD, POM and DSC in tandem (Figure 1.22). For the most part, one technique cannot adequately determine whether a phase is liquid crystalline.

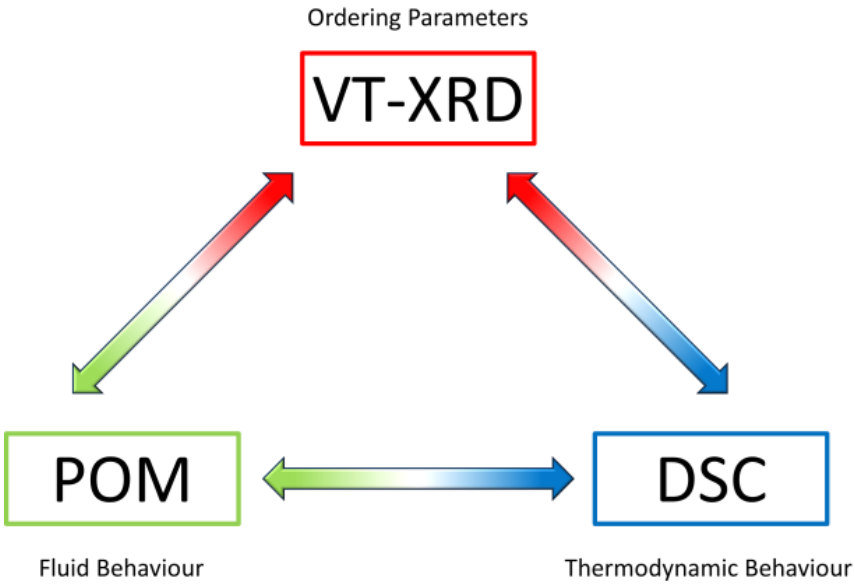

Figure 1.22: Schematic diagram of how POM, DSC and XRD complement one another in the characterization of liquid crystal phases.

For example, polarized optical microscopy (POM) is often used as an initial assessment to determine if a liquid crystal phase is present at all. Any observed textures will suggest the presence of birefringence and by association the anisotropy that is characteristic of a mesophase; to a limited degree the phase type of the mesophase can also be inferred. Another important part of this analysis is the use of applied pressure to determine the fluidity of the sample.

With some idea about whether there is a mesophase present, differential scanning calorimetry (DSC) is able to report the temperature and enthalpy of each of a sample's phase transitions. Barring multiple crystalline states, a non-mesogenic material should have only one peak in its DSC trace, corresponding to the solid to liquid transition. Therefore, the presence of more than one peak within that temperature range suggests that a liquid crystal phase is present. This can be confirmed by comparing the phase change enthalpies as discussed previously. Thus, calorimetry is able to provide all of the pertinent thermodynamic information about the potential mesophase.

Although DSC cannot unequivocally determine the presence of a liquid crystal phase, the transition temperatures determined from calorimetry are valuable in identifying the temperature ranges that must be explored in further investigations.

At this point, the substance being investigated is very likely liquid crystalline provided that POM has shown that it is fluid and has some degree of ordering, and DSC has demonstrated that this phase is stable over a well-defined range of temperatures. However, nothing quantitative is known about the mesostructure. Variable temperature X-ray diffraction comes into play here and can provide us with an assessment of the periodic structure of the material. The unit cell parameters are the final piece of evidence that confirms the type of ordering previously hinted at initially by POM textures.

1.6. Structure Property Relationships

There are still many unanswered questions concerning the self-assembly of liquid crystalline phases[49]. Traditionally, studies have endeavoured to determine how structural modifications impart changes in the phase behaviour of the material, specifically the effect on transition temperatures[50]. Many reports have been published concerning modifications to rod- or disc-shaped base systems: the nature of the aromatic core, the number and length of peripheral alkyl chains[51], and the effect of electron-withdrawing or donating substituents[52,53] are among the structural factors that have been shown to impact transition temperatures as well as the types of mesophases present.

Recently there has been an increased emphasis on the intrinsic morphologies of the mesophases themselves. The geometries of certain mesostructures have been shown to couple well with specific applications. For example, certain chiral columnar mesophases have been shown to form aligned structures that can undergo unique conformational changes which could provide drastic improvements in switching technology. Materials created with liquid crystal scaffolds[54,55] are another example of a field in which the actual pattern and spacing of the mesostructure is of paramount concern.

This thesis is primarily concerned with the structures of discotic molecules and their associated phase behaviours. The idea that it is possible to achieve uncommon mesophases through molecular design is a compelling motivator for further study.

1.6.1. Shape Factors

Let us place calamitic molecules and their associated smectic and nematic phases on one end of a range of possibilities, and discotic molecules with their columnar hexagonal or rectangular phases at the other end (Figure 1.23). The two shapes represent the extremes of structural possibilities. There must exist a continuum of intermediate shapes between these two endpoints. Surprisingly, there has been little to no inquiry[56] into the range of possible shapes that might exist between the extremes of rods and discs.

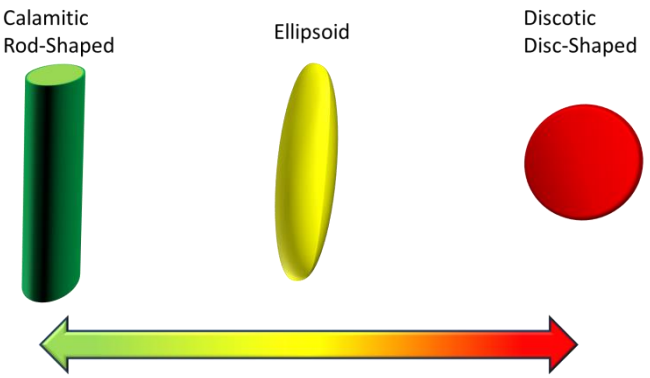

Figure 1.23: Schematic representation of the range of shapes that may exist between the extremes of rod (length is largest dimension) and disc (radius is largest dimension).

It should be noted that phasmid materials – compounds that exhibit both discotic and calamitic type phases[57] - have been previously reported in the field of polycatenars and metallomesogens[58,59]. However, these molecules have either complex structures or the presence of groups such as metal centers whose influence cannot be reasonably decoupled from the effect of the overall shape of the molecule. In general, there has been a preponderance of studies in which the focus has been modification of the LC core or peripheral chains – leaving ample room to study the role of shape for molecules known to produce mesogenic behaviour.

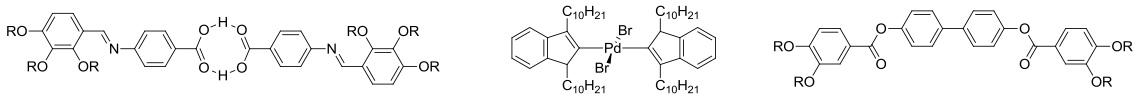

Figure 1.24: Examples of phasmid materials. Molecule types (mesophase formed) from left to right: hydrogen bonded (nematic)[60], metallomesogenic (lamellar)[61], polycatenar (cubic)[62].

For example, disc-shaped molecules have been shown to exhibit nematic phases. Has the flat, circular shape been changed to one that is more cylindrical? One way to do this would be to consider the columns formed as cylinders. However, although many discotic liquid crystals form columnar phases, very few form nematic phases[63]. Even if these columns are 'rod-like' in shape, they do not appear to form the matching mesostructures. The other way of doing this would be modification of the basic disc-shape in a way that increases the length of the molecule at the expense of its width. Recent studies have shown that under certain circumstances an 'atypical' phase may be induced that might not be expected from that particular molecular shape. For example, there are several examples of nematic phases exhibited by discotic mesogens. Since the shape (rod or disc shaped) of the molecule has been widely demonstrated to result in specific types of mesostructures, these reports raise interesting questions. Is there a point at which the influence of shape is diminished? If so, what factors take over? If a structure associated with a 'rod-shape' such as the nematic phase is attained by a molecule that is shaped like a disc, is it possible that the shape of the molecule has been altered to make it more 'rod-like' instead of 'disc-like'? Or is the cause something else altogether?

1.6.2. Dimers

It is a troubling task to elongate a disc-shaped molecule into more of a rod shape simply by changing the alkyl or pendant substituents. In the case of the numerous rod-like biphenyl derivatives, the pendant alkyl chains are most often located in the 3- or 4-position. By extending the length of these alkyl chains, the length of the entire molecule is increased and the shape as a whole will become more 'rod-like'. For most disc-shaped liquid crystals, owing to synthetic accessibility the alkyl chains are often positioned in more spread out positions. It is difficult to extend particular chains in the same way that is possible for calamitic molecules, especially if the alkyl chains are distributed evenly

along the perimeter of the aromatic core. Also, at some point the influence of these alkyl moieties becomes dominant in the self-assembly and the mesophase may be inhibited.

Conceptually, an easier way of elongating the overall shape of the molecule is to take two of the circular cross sections and connect them. As shown in Figure 1.25, an ellipse can be drawn over two such cross-sections; in 3-D the overall shape would be the aforementioned ellipsoid. Thus, the creation of dimers of known discotic mesogens may enable us to design a more rod-like molecule that might realize the associated rod-like phases such as smectic or nematic. This idea is borne out by reports of the formation of nematic phases by disc-shaped molecules that are joined together by hydrogen-bonded dimers[64,65,66].

The Williams Group has reported a number of liquid crystal forming molecules based on a dibenzophenazine (DBP) core. Although most of these molecules formed columnar hexagonal phases, the carboxylic acid derivatives formed a columnar rectangular phase followed by a nematic phase at higher temperatures. This difference in behaviour was rationalized by positing the formation of hydrogen bonded dimers that elongated the overall shape of the molecule. Note that an ellipsoid fits neatly between the proposed extremes of rod and disc. This change in morphology affected the packing within each column, disrupting the compact periodicity of the hexagonal phase, and resulted in the complete destabilization of the columnar packing as evidenced by the presence of the disordered nematic phase at higher temperatures.

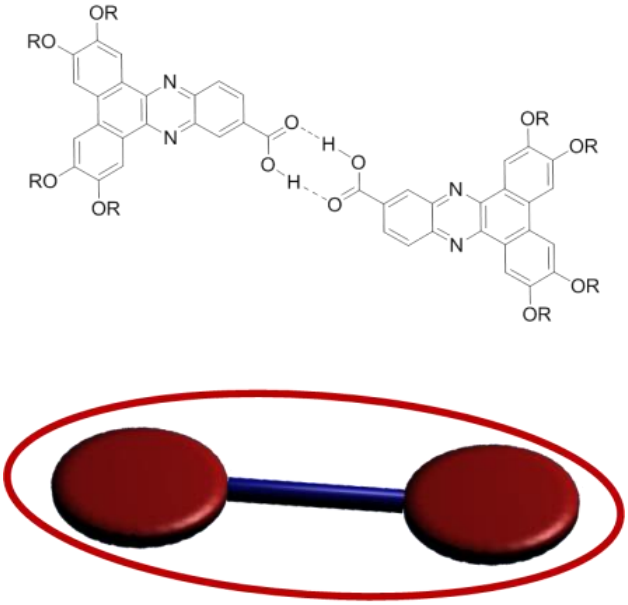

Figure 1.25: Extended dimer model of DBP cores linked by hydrogen bonding.

Since that study, several workers have described the formation of nematic phases in discotic dimer systems[6768,]. We were therefore motivated to further investigate the role of dimers in the self-assembly of discotic liquid crystal phases.

1.6.3. Dimer Models

Considering the body of literature regarding discotic mesogenic dimers described above, we felt it would be useful to develop a schematic model to aid us in the identification and conception of possible dimer molecules.

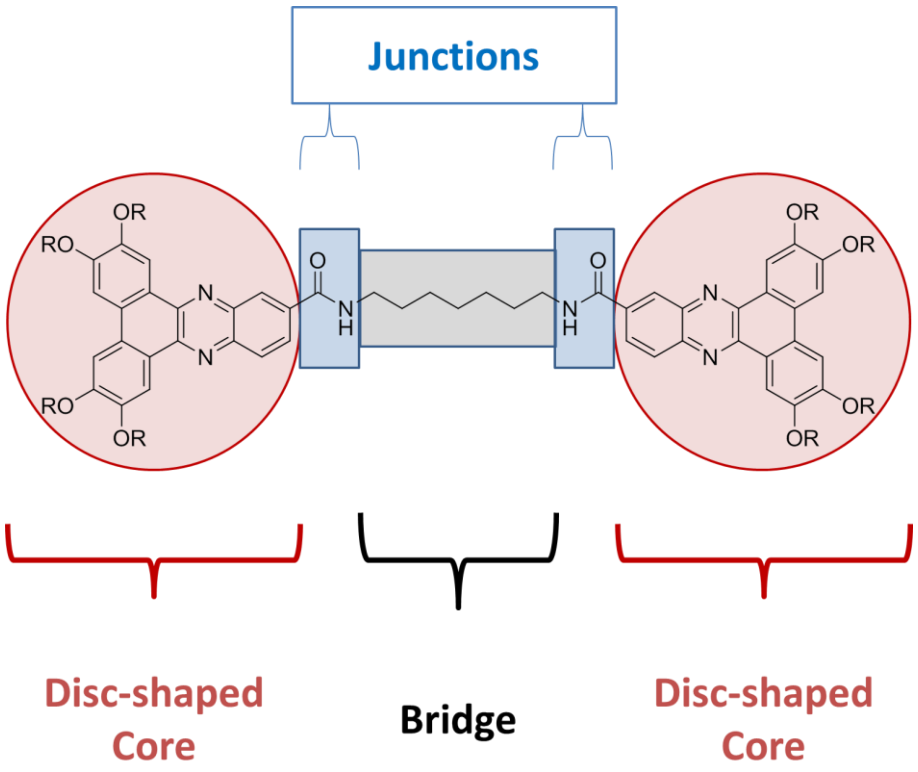

Figure 1.26: Schematic model of disc-shaped dimers. Red circle: disc-shaped aromatic core; Blue box: junction functional group; Grey box: bridge moiety.

The essential elements of a discotic dimer are the two disc-shaped molecules, henceforth referred to as monomers, that are to be connected in some fashion. The connection itself has two components: the actual bridge and the junction moieties used to connect each dimer to the bridge. Of the dominant trends in the field of discotic liquid crystals, one of the most prevalent is the use of triphenylenes as the aromatic core of the potential mesogen. There have been several reports of dimer molecules in which two triphenylenes were linked together. In the majority of studies, an ether junction was used to link the monomers to a flexible alkyl bridge.

In our studies we decided to continue with the use of DBP cores since: their chemistry is well-developed within the lab; they offer a versatile range of substitution methods; and their mesogenic behaviours are reasonably well understood. After

choosing the type of disc-shaped ‘unit’, a dimer can be designed by deciding on an appropriate linking group (Figure 1.26).

The substantive work of this thesis has been centered around relatively rigid bridges. The major advantages of such a system compared to those most prevalent in the literature are the elimination of factors which might play a significant part in the self-assembly of liquid crystal phases. For example, the ether linkages utilized in most studies have an inductive influence that complicates the analysis of the liquid crystalline phase behaviour. Compared to flexible linkers, rigid linkers provide less possible conformations to consider. Finally, the use of rigid linkers may result in extended conjugation between the aromatic cores that in turn could favourably affect attributes such as band gap or conductivity.

1.6.4. Direction of studies

Several molecular systems were investigated during the course of the studies presented herein, but only two bore fruit. Therefore they form the bulk of the discussion in this thesis. However, they are notable steps towards answering our questions about the relationship between liquid crystalline phase behaviour and dimer structure. In Chapter 2, a series of molecules is discussed that can be thought of as rigidly linked but without a junction or bridge. In Chapter 3, we will discuss work towards the study of dimers with rigid phenyl bridges connected via amide junction groups. These types of molecules combine the hydrogen bonding abilities of known dimer systems with a covalently bonded linker.

2. Benzidines

2.1. Introduction

To reiterate, in general we can regard dimers as an assembly of three major components: the two disc-shaped cores, the bridge structure linking those discs, and the linker moiety that lies between them.

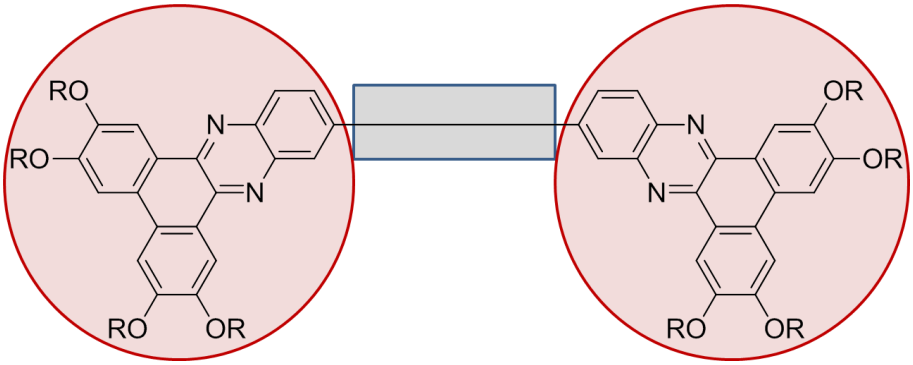

Figure 2.1: Schematic model of disc-shaped benzidine-based dimer and their primary components. C-C bond elongated for emphasis.

Previously reported acid derivatives (Figure 1.25) from the Williams group can be thought of as two cores with carboxylic acid linkers forming a non-covalent bridge[99]. The hydrogen bonding interaction is a relatively rigid bridge; although several studies exist involving mesogens capable of hydrogen bonding, studies utilizing a rigid, covalently-bonded bridge are limited to only a handful of reports. One notable exception is the triphenylene dimer reported by Kumar[69,70], in which the discs are connected via an acetylene bridge. The acetylene bridge itself is significant since to the best of our knowledge it represents the only reported example of a rigid, covalent bridge, and it also exhibits unusual phase behaviour in the form of a nematic phase.

A question came immediately to our minds: what kind of phase behaviour would be observed from a rigid dimer with the simplest possible bridge? Based on our previous

success with dibenzophenazines, we looked into the possibility of creating a dimer that connected two such cores with a single carbon-carbon bond.

In pursuit of this goal, we employed a simple amine condensation catalyzed by a hypervalent iodine catalyst: *o*-iodoxybenzoic acid. The resulting series of dibenzophenazine cores connected by a single carbon-carbon covalent bond will hereafter be referred to as benzidine dimers and abbreviated as DBPD-6, DBPD-8 and DBPD-10, where the numeric suffix reflects the length of each of the eight peripheral alkyl chains

2.2. Synthesis

The DBP derivatives were synthesized from the corresponding quinone, Quinone-n where n is the length of the peripheral alkoxy chain. These diketones have been condensed with a variety of *o*-phenylenediamines, resulting in dibenzophenazine mesogens that have been widely explored in the Williams group. Normally this is a facile reaction with near quantitative yields – for example a large excess of 3,4-diaminobenzoic acid is simply refluxed in acetic acid to afford the aforementioned carboxylic acid molecules. Therefore it was a natural step to use this same strategy but using a 3,3'-diaminobenzidine in which the biphenyl linkage had already been established.

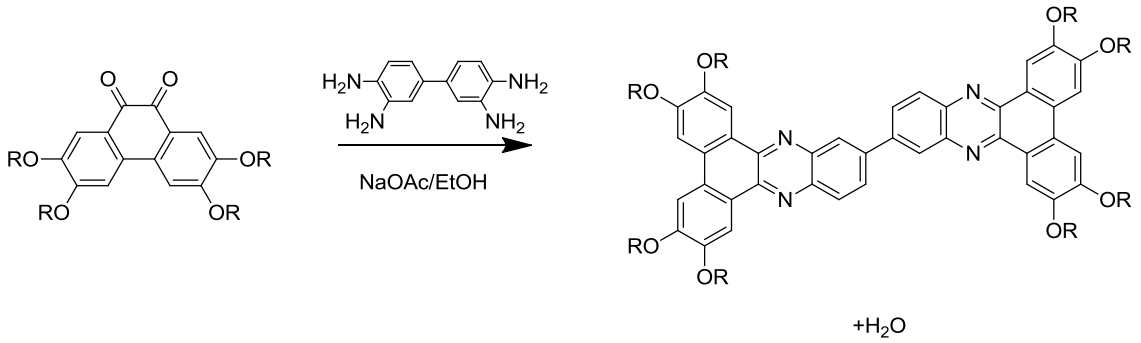

Scheme 2.1: Proposed synthetic pathway for dibenzophenazine (DBP) dimers from the phenanthrene dione via condensation.

However, the synthesis of these compounds was not as straightforward as originally anticipated. As seen in Scheme 2.1 the overall reaction can be seen as a simple condensation reaction between two diketones and a tetramine to form a pair of

bridged dibenzophenazines, which should be driven by the formation of an aromatic heterocycle. We foresaw several possible issues with these types of reactions, such as the production of excess water and a decrease in efficiency due to the coupling of the nucleophile with a relatively unreactive electron rich carbonyl.

Initial efforts utilized standard basic conditions to neutralize the hydrochloride salt of the benzidine *in situ*. To that end, the reaction was carried out in a large amount of sodium acetate in refluxing ethanol. Unfortunately, ^{1}H NMR of the crude mixture indicated that none of the target molecule was formed; only starting material and trace amounts of side products. Attempts to identify the side products by ^{1}H NMR and mass spectrometry were unsuccessful.

In order to overcome these difficulties, we investigated alternative synthetic methodologies. Heravi and co-workers efforts[71] in quinoxaline synthesis demonstrated the increased efficacy of condensation reactions between aryl 1,2-dicarbonyl compounds and *o*-phenylenediamines in the presence of a catalytic amount of *o*-iodoxybenzoic acid (Scheme 2.2) which is most well known as an mild oxidant[72].

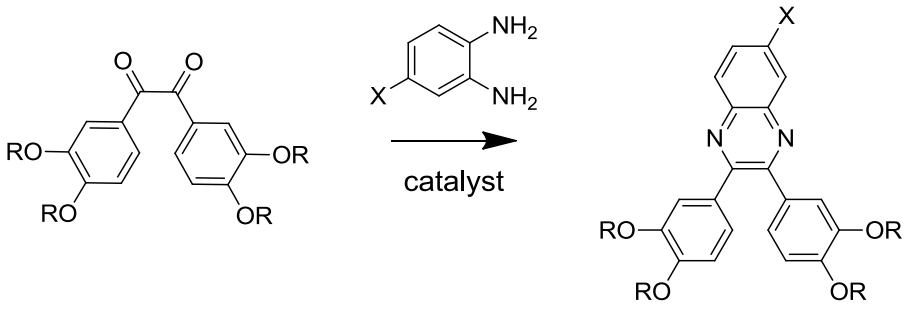

Scheme 2.2: Quinoxaline diamine condensation route as proposed by Heravi, in which quantitative yields were realized with both electron withdrawing and electron donating functional groups (X=H, NO_2, CH_3).

The high yield (>98%) and mild conditions (room temperature) made this one-pot procedure quite attractive, especially since high yields were reported to be independent of different combinations of electron-withdrawing and electron-donating groups on both starting materials. This led us to a route in which the reaction is carried out at room temperature in glacial acetic acid with a catalytic amount of o-iodoxybenzoic

acid (IBX). In addition to the mild conditions, the procedure required only a stoichiometric amount of quinone.

Considerable effort was expended in the subsequent optimization of this reaction using Heravi's conditions and others. Some of the conditions attempted are outlined in Table 2-1. Overall, catalyzing the reaction with IBX at moderate temperatures in DCM one pot seemed to provide the best yield.

Table 2-1: Summary of optimization studies of the dimer condensation using IBX as the catalyst. Yields determined by NMR of crude.

	Compound	Reagent	Solvent	Temperature (°C)	Time (h)	Crude Yield (%)	
Yield↑ as T↑	C_6	IBX (cat)	AcOH	RT	24	31%	Yield↑ as time↑
	C_6	IBX (cat)	AcOH	RT	48	46%	
	C_6	IBX (cat)	AcOH	40	24	56%	
Yield↓ as time↑	C_8	IBX	AcOH	40	48	63%	Yield↓ as time↑
	C_8	IBX	AcOH	40	72	41%	
	C_8	IBX	AcOH	70	72	14%	
	C_{10}	IBX	AcOH	RT	48	2%	Yield↓ as time↑
	C_{10}	IBX	AcOH	RT	72	0%	
	C_{10}	IBX	AcOH	40	24	46%	Yield↓ as time↑
	C_{10}	IBX	AcOH	40	48	28%	

The final dimer series was synthesized in one pot by adding a stoichiometric amount of the diketone to the commercially available free-amino form of 3,3'-diaminobenzidine along with a catalytic amount of IBX. The reaction was carried out in glacial acetic acid at 40°C for 24 hours. After purification, the resulting molecules were produced in acceptable yields (Scheme 2.3, 21-36%).

The final compounds were successfully purified by column chromatography, but due to their limited solubility in common organic solvents (with the exception of chloroform) they were difficult to recrystallize. They were also susceptible to contamination by long chain alkyl impurities common to those solvents and were therefore isolated using a combination of washing and centrifugation.

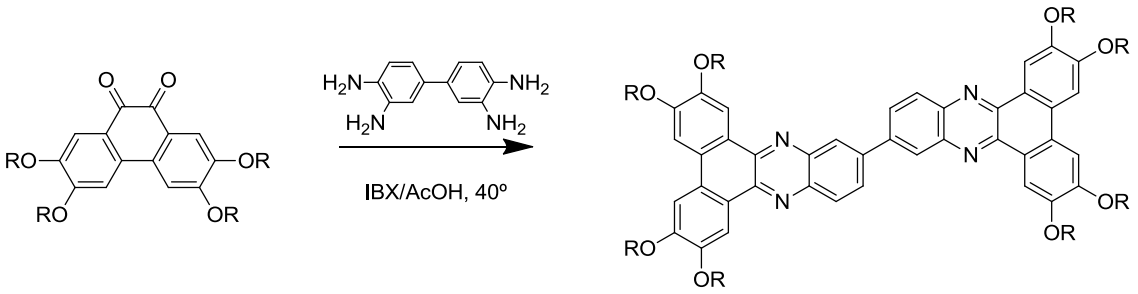

DBPD-6: R=C_6H_{13} (21%)
DBPD-8: R=C_8H_{17} (36%)
DBPD-10: R=$C_{10}H_{21}$ (23%)

Scheme 2.3: Final synthetic pathway for synthesis of DBP dimers DBPD-X from the phenanthrene dione with varying alkoxy chain lengths.

2.3. Results and Discussion

The liquid crystalline properties of each molecule were characterized by polarized optical microscopy (POM), differential scanning calorimetry (DSC) and variable-temperature X-ray diffraction (VT-XRD) as described in the introduction (1.5.3).

2.3.1. DBPD-6 Results

Polarized Optical Microscopy

Polarized light photomicrographs of DBPD-6 taken just below the isotropic transition exhibit schlieren textures on both heating and cooling, which are characteristic of a nematic phase. A plastic phase formed at lower temperatures, as evidenced by the lack of flow when the sample was subjected to pressure applied to the glass cover slip using a spatula. Once the nematic phase was fully formed on cooling, several distinct textures were observed growing out of the nematic phase (Figure 2.2) at different rates, sometimes in combination with each other. This observation suggests that there is cooling-rate dependent polymorphism of the sample.

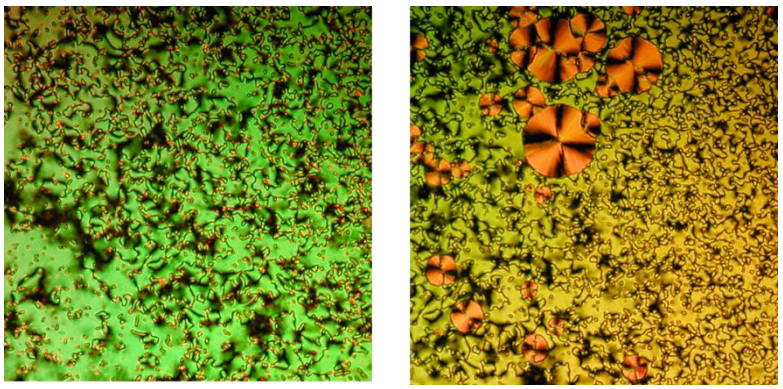

Figure 2.2: Polarized Optical Micrographs (POM) of DBPD-6 through crossed polarizers. Left: schlieren texture characteristic of a nematic phase. (~204° C, 8x magnification, -10° C/min) Right: 'Maltese-cross' textures "growing in" amidst the now yellow nematic phase. (~189° C, 8x magnification, -5° C/min)

The most consistent pattern obtained from photomicrographs was the growth of dendritic structures from the nematic region with roughly orthogonal branches (Figure 2.3, left). More rapid cooling rates from below the clearing temperature resulted in the formation of round domains featuring Maltese-cross type patterns (Figure 2.3, right).

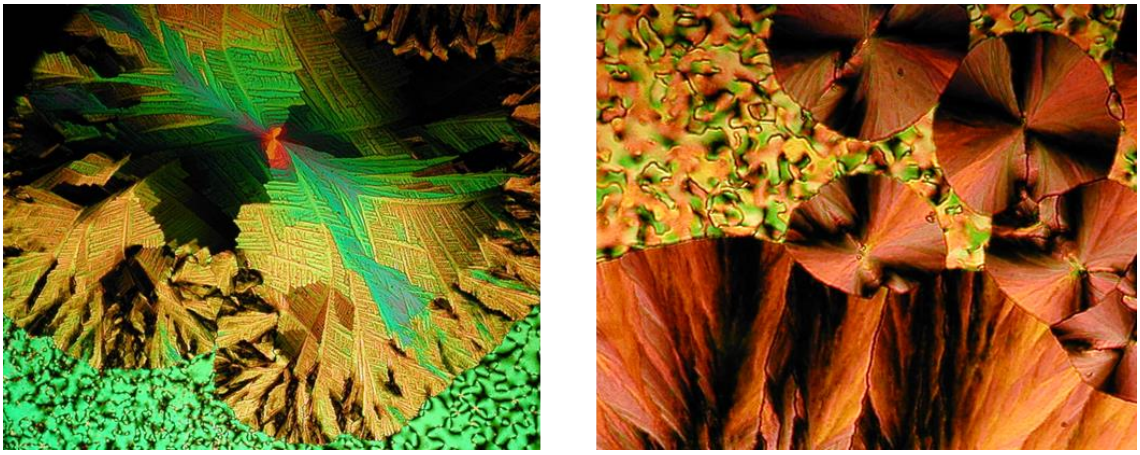

Figure 2.3:Polarized Optical Micrographs (POM) of DBPD-6 through crossed polarizers. Left: Dendritic texture growing out of green Schlieren texture. (~189° C, 8x magnification, -1° C/min) Right: 'Maltese-cross' textures growing out of yellow nematic phase. (~189° C, 8x magnification, -5° C/min)

These observations were the first indication that these molecules had unusual phase behaviour. Recall that most disc-shaped mesogens form columnar hexagonal liquid crystal phases, and these phases are accompanied by dendritic textures whose inter-branch angle is around 60° (1.5.1). Figure 2.4 outlines the differences between the textures. In top and bottom insets of Figure 2.4, the boundary of the structures are clearly delineated. Lines have been added to emphasize the relative orientations of the dominant features in each structure – the wedge and branch shapes in the fan and dendrite, respectively. In both cases these features are nearly but not quite orthogonal to one another as opposed to the six-fold symmetry expected for a columnar hexagonal phase. This points towards a structure that is different from the normally observed Col_h.

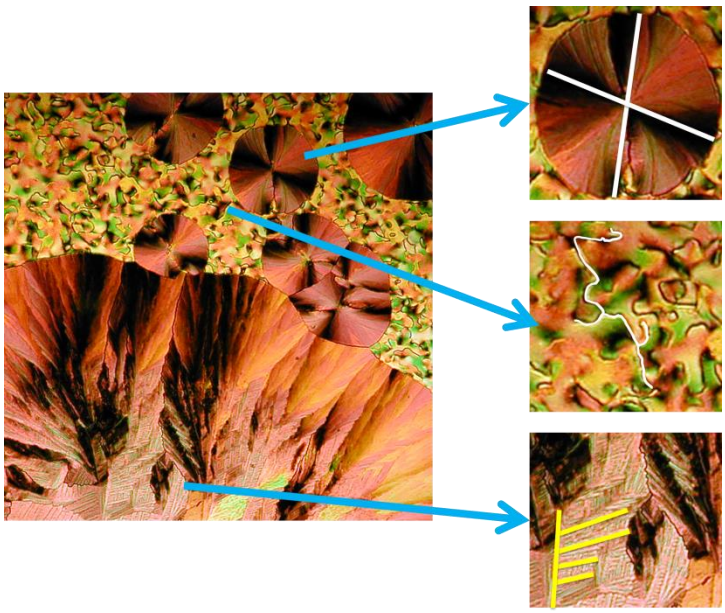

Figure 2.4: DBPD-6 POM (~189° C, 8x magnification, -5° C/min) detailing different textures: Maltese cross (top inset) with 4-fold features highlighted with white line; schlieren (middle inset); and dendritic (bottom inset) with branch growth highlighted with yellow lines.

In stark contrast to these geometries are the curved lines meandering through randomly and multiply coloured areas between which have no obvious boundaries. These dark lines are referred to as brushes and this pattern of irregularly shaped regions is known as a schlieren texture. We can qualitatively assess the relative amount of order in the phases observed: the fan and dendritic textures should correspond to relatively more ordered structures, while the seemingly random schlieren texture should be reflective of the more disordered nematic phase.

Differential Scanning Calorimetry

The hexyl dimer (DBPD-6) produced DSC traces that showed three significant peaks on heating and two on cooling, which was representative for the series as a whole. This is most apparent in the first heating data (Figure 2.4, left). The number and breadth of the peaks observed for the series suggests the formation of two liquid crystal phases. There were also a number of broad diffuse peaks that indicated that multiple polymorphs may form in addition to the stable mesophases (Figure 2.4, right bottom inset). Although these peaks were persistent through different heating and cooling rates, note that they are not present in the first heating run DSC. This suggests that such

polymorphs arise out of glass phase LCs created on supercooling. However, no evidence of these polymorphs was apparent in the POM results mentioned in the previous section. This is not surprising since polymorphs for liquid crystal phases are a mixture of co-existing mesostructures (e.g. a mixture of fan and dendritic type columnar phases) that may be present at extremely short length scales. At lower temperature, supercooling may render these liquid crystal phases into glasses. Crystalline phases may also contribute to the polymorph – note that in Figure 2.5(right) the distinct T_m peak appears as two peaks in the sample with thermal history, which would indicate partial crystallization of the sample. It is no coincidence then that such a sample exhibits polymorphic peaks at low temperatures as the proportions of glassy and crystalline phases change with temperature.

Notably, DSC data for the DBP derivative with hexyl side chains (DBPD-6) includes a small non-hysteretic peak at high temperature and a distinct shoulder on the middle transition peak on cooling. This may indicate another liquid crystal phase but due to the overlap it was beyond our technical capabilities to determine the actual structure present using X-ray diffraction.

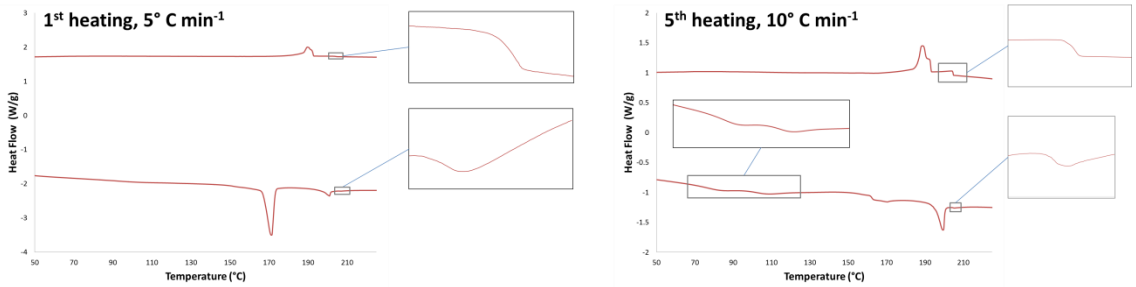

Figure 2.5: Differential Scanning Calorimetry traces for DBPD-6. Left: 1st heating of sample, 5° C min-1. Right: sample with thermal history but reference rate of 10° C min-1. Insets left: magnified view of nematic to isotropic liquid transition. Inset right: magnified view of diffuse peaks corresponding to possible polymorphs. Inset far right: magnified view of nematic transition peaks.

The nematic phase postulated for DBPD-6 can now be positively identified since the DSC provides us with the second of two characteristic properties: the schlieren texture observed in the POM together with a consistent small-enthalpy peak that shows almost no hysteresis in the DSC (Figure 2.11, left insets). Since the nematic phase is relatively disordered, we expect a small energy barrier to its formation. Further, the

formation of a nematic phase does not require extensive re-ordering of the self-assembled structures on cooling, and thus should also be less susceptible to super-cooling effects commonly seen in liquid crystal phase transitions. These two factors contribute to the lack of hysteresis observed for the DBPD-6 nematic phase in the DSC, and the phenomenon is persistent over several heat/cool rates despite thermal history (Figure 2.5 insets left and far right).

The final DSC data for DBPD-6 is in Table 2-2.

Table 2-2: Differential Scanning Calorimetry (DSC) results for DBPD-6 at 5°C/min. Transition: T_t, °C (Enthalpy, J/g)

Compound	Phase	Transition	Phase		Phase	Transition	Phase
DBPD-6 (R=C_6H_{13})	Cr	171.3° (26.0) →	Col_{ob}	201.0° (3.2) ⇌ 189.6° (7.3)	N_D	206.9° (0.1) ⇌ 204.8° (0.1)	I

X-Ray Diffraction

Typical diffractograms produced by DBPD-6, when examined by variable temperature XRD (140° C to 180° C), consisted of a relatively sharp prominent peak at low angles, at least one significant peak at a slightly higher angle, then followed by several diminishingly intense peaks. The last observed features at high angles were broad peaks at 3.5 Å and 4.5 Å, which were assigned to the π-π stacking and alkyl halo peaks respectively (Figure 2.6). All peaks reported were persistently observed at approximately the same diffraction angles despite changes in the cooling rate, temperature and sample within the appropriate temperature range for a phase. The peaks also disappear when XRD is performed after the clearing transition.

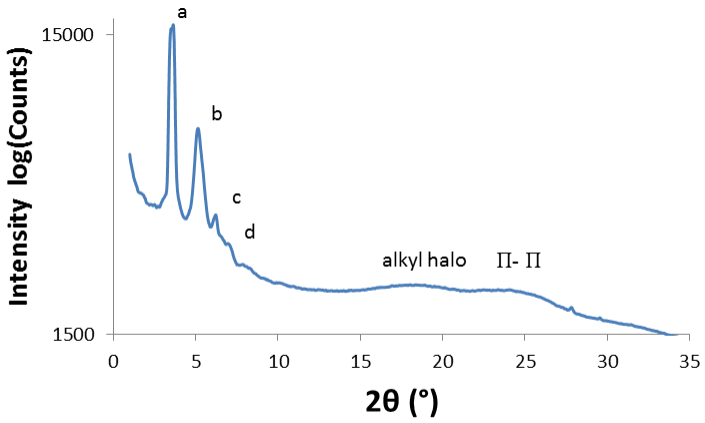

Figure 2.6: XRD diffractogram for DBPD-6 (142° C) with the four most intense peaks (a-d) labelled as well as the alkyl halo and π-π peaks at high angles.

Despite the familiar textures observed by POM, the XRD results were inconsistent with those typically reported. For example, a Col_h phase usually exhibits two peaks whose d-spacing ratio is 1:√3, corresponding to Miller indices (100):(110) in a hexagonal packing. Col_{square} or Col_{tet} packing typically give rise to peaks with a ratio of 1:√2 for (100):(110).

Since the data did not match the established patterns for common liquid crystal phases, a more general approach was taken (a detailed treatment is available in the Appendix). The essential process is to take the reciprocal d-spacing's of the peaks relative to the most intense one. Patterns called 'systematic absences' arise from the type of ordered structure present, as illustrated in Table 2-3.

Table 2-3: Examples of systematic absences for cubic structures. Obtained by taking the reciprocal of the d-spacing, then taking the ratio of these reciprocals relative to the most intense peak at low angles.

Structure Type	Reciprocal d-spacing ratio relative to most intense peak
Primitive Cubic	$\mathbf{1:\sqrt{2}:\sqrt{3}:\sqrt{4}:\sqrt{5}}$
Body-centered Cubic (BCC)	$\mathbf{1:\sqrt{2}:\sqrt{4}:\sqrt{6}:\sqrt{8}}$
Face-centered Cubic (FCC)	$\mathbf{1:\sqrt{3}:\sqrt{4}:\sqrt{8}:\sqrt{11}}$

At this point in the analysis, we considered phases that are very uncommon for liquid crystals in general. In comparison to the above patterns a cubic phase would be consistent with 1:√2:√3:√4, but would also yield an optically isotropic texture; while the DBPD-6 dimer appeared optically isotropic in both the POM sample and XRD capillaries there were significant peaks that did not correspond to the pattern. The BCC and FCC cubic lattices were similarly rejected. The rarely reported pseudo-hexagonal phases Col_{hr} and Col_{rh} as reported by Guillon[73] and Ohta[74,75] were considered at this point but ultimately rejected because the √2 value could not be obtained in such a two-dimensional lattice. The difficulty of indexing the phase is represented in Table 2-4 – note that at best only 3/5 of the expected d-spacing ratios can be matched with those observed. Conventional peak patterns consistently failed to account for all observed peaks.

Table 2-4: XRD summary chart for several possible packing arrangements. Each column corresponds to a peak observed in the XRD, represented by its reciprocal ratio with the most prominent peak. Values are rounded to the nearest integer radicand wherever possible. Peaks used are from DBPD-6 at 142° C.

	1	1.15	$\sqrt{2}$	1.49	$\sqrt{3}$	$\sqrt{4}$
Cubic	Yes	No	Yes	No	Yes	Yes
Hexagonal	Yes	No	No	No	Yes	Yes
Tetragonal	Yes	No	Yes	No	No	Yes
Hex/Rec	Yes	No	No	No	Yes	Yes

It was therefore decided to consider a two-dimensional columnar oblique phase. By fitting the ratios of the three most intense peaks to all possible combinations of low-valued Miller indices, we were able to determine several solutions for the possible unit cell parameters for a Col_{ob} phase (Figure 2.7).

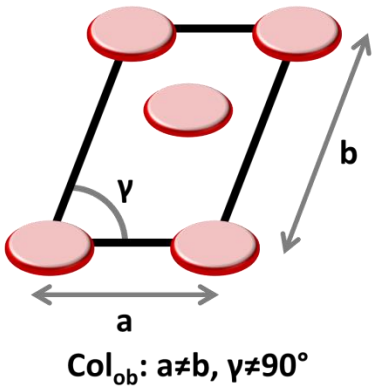

Figure 2.7: Schematic diagram of a columnar oblique phase. Circles represent tops of columns for clarity

However, as mentioned in the POM discussion the dendritic textures of the DBPD-6 compound appear to be nearly orthogonal. As expected, solutions with the least error between the calculated and observed peaks corresponded to those whose γ_{calc} fell between ±10° of 90°. We were therefore confident that the method of fitting was sound. In addition, the dendritic textures observed were similar to those previously reported[76] for a metallomesogenic columnar oblique phase (Table 2-1).

Table 2-5: X-ray Diffraction (XRD) results for DBPD-6.

Compound	Temperature (°C)	d-spacing (Å) Calculated	Observed	Assignment (hkl)	Phase
R=C_6	181	24.3	24.3	(1-1)	Col_{ob}
		17.0	17.1	(2-1)	(a = 40.9 Å, b = 29.7 Å,
		14.1	14.2	(-12)	γ = 91.3°)
		13.9	13.6	(12)	
		12.5	12.5	(-31)	
			4.8	*alkyl halo*	
			3.6	*π-π*	
R=C_6	142	24.1	24.1	(200)	Col_{ob}
		20.8	20.8	(-2-10)	(a = 48.3 Å, b = 35.7 Å,
		17.2	17.2	(-1-20)	γ = 84.8°)
		16.2	16.1	(1-20)	
		14.2	14.1	(3-10)	
		12.5	12.5	(320)	
			4.8	*alkyl halo*	
			3.6	*π-π*	

2.3.2. DBPD-8 Results

Polarized Optical Microscopy

Viewed through crossed polarizers, dendritic-type textures were also observed for DBPD-8 but this is evident only at high magnification just below the clearing temperature. As seen in Figure 2.8, these dendritic structures do not have an obvious fourfold or six fold character, and as they grow larger they form random shapes. This makes it difficult to use POM as a determination for the type of liquid crystal phase present. Interestingly, the birefringent domains do not follow typical liquid crystal behaviour; they do not grow to take up most of the field of view with relatively few dark areas. Instead, there seems to be much more ‘dark field’ when viewed through crossed polarizers. A preponderance of dark field is a hallmark of a cubic as well as homeotropically aligned columnar structures.

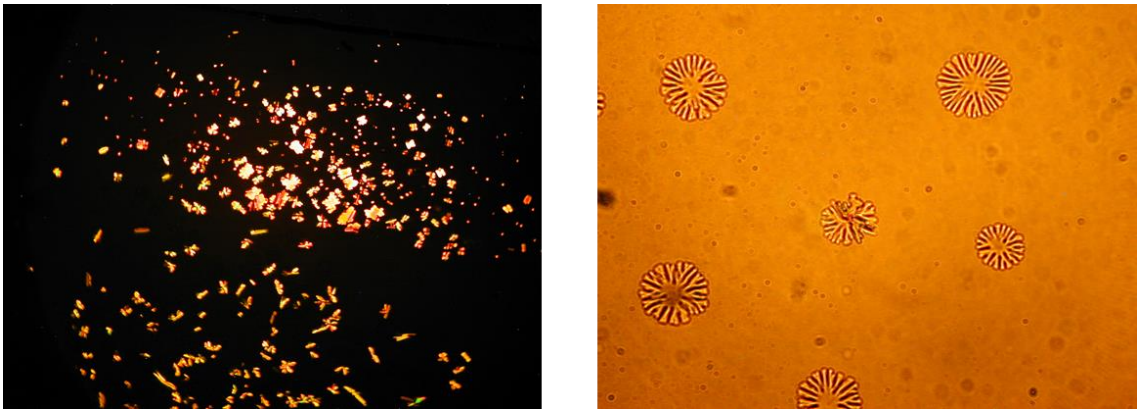

Figure 2.8: POM of DBPD-8. Left: Scattered birefringent areas against a "black field" background (~195° C, 8x magnification, -1° C/min) Right: Dendritic formation of domains seen at left as seen through uncrossed polarizers (~195° C, 80x magnification, -1° C/min)

Since cubic phases are quite rare for discotic mesophases[77,78], the pervasive lack of texture observed through crossed polarized is likely indicative of a homeotropically aligned material. This concept is covered in depth in 1.4.2, but Figure 2.9 is provided as an in-chapter reference. Looking down vertically along the long axis of the self-assembled columns will result in black featureless areas in the POM images. Since some degree of alignment is unavoidable in a randomly oriented sample, the lack of texture must be a dominant feature of the POM image in order to identify a homeotropically aligned phase.

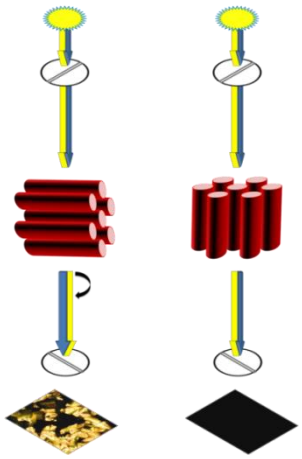

Figure 2.9: In-chapter reference for Figure 1.14 . Orientation effects of columnar mesophases. Left: normal POM image observed due to birefringence. Right: No texture observed when looking down along the long axis of the columns.

After further investigation these dendritic textures were found to be homeotropically aligned with the glass slide and cover slip as displayed in Figure 2.10. These large, aligned, plastic domains were found to coalesce into a single aligned background or monodomain at lower temperatures (Figure 2.10). This result is important on its own. Again, alignment of mesostructures is important in many applications (1.5.1) and much effort has been expended by industry towards forcing such structures to align in a certain orientation relative to the film and/or substrate. Furthermore, the homogeneity of those aligned materials is important. Since both uniformity and orientation are typically achieved using external modification such as treating the substrate or annealing the device, the potential benefits of a material that spontaneously aligns and forms its own monodomains are very attractive.

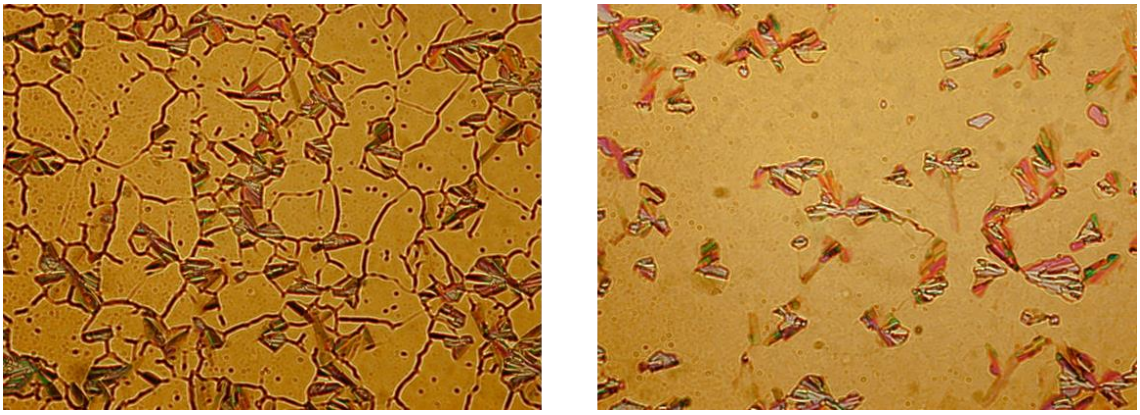

Figure 2.10: POM of DBPD-8 through uncrossed polarizers. Left: Birefringent areas against a background of homeotropically aligned domains (195.3° C, 20x magnification, -1° C/min) Right: Formation of homeotropically aligned monodomains. (~140° C, 20x magnification, -1° C/min)

Differential Scanning Calorimetry

In contrast to DBPD-6, peaks for DBPD-8 are conventional, with no discernible nematic peak as shown in Figure 2.11. However, some undulations are present similar to those seen for the previous compound (Figure 2.11, right inset); these may indicate the presence of additional polymorphs.

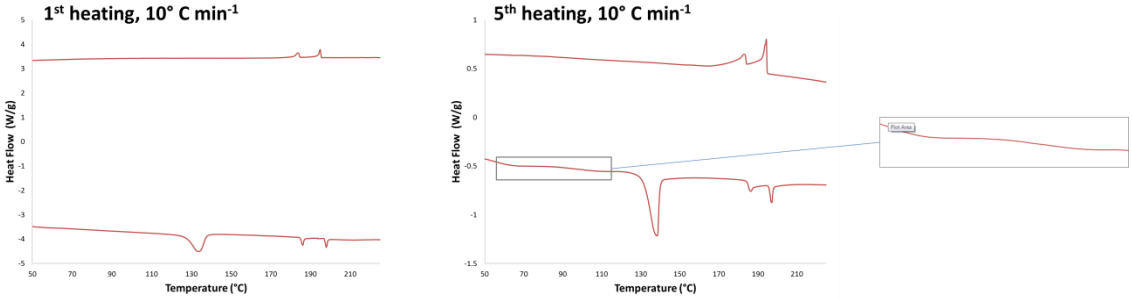

Figure 2.11: Representative differential scanning calorimetry (DSC) traces for DBPD-8. Left: 1st heating of sample, 10° C min-1. Right: sample with thermal history but reference rate of 10° C min-1. Insets right: magnified view of diffuse peaks corresponding to possible polymorphs.

Note that although the first cooling peak may seem large, its actual enthalpy is on the same order as that for the corresponding heating transition, and both transitions have energies one tenth of that observed for the melting transition. The lack of a melting peak on cooling indicates that a glass is formed. Compared to the previous dimer, here

the peaks at higher temperatures are separate and distinct from one another; their presence clearly suggests the presence of two liquid crystal phases.

Table 2-6: Differential Scanning Calorimetry (DSC) results for DBPD-8 at 10°C/min. Transition: T_t, °C (Enthalpy, J/g)

Compound	Phase	Transition	Phase		Phase	Transition	Phase
DBPD-8 (R=C_8H_{17})	Cr	133.9° (17.0) →	Col_{ob}	186.0° (1.5) ⇌ 184.6° (1.1)	Col_h	197.9° (1.4) ⇌ 195.4° (1.4)	I

Again, comparison of the 1st heating against a sample with thermal history shows that diffuse peaks do not show up in the originally heated sample. This reinforces our theory that these peaks are due to polymorphism of the liquid crystalline phase formed on cooling.

X-Ray Diffraction

Typical diffractograms produced by DBPD-8 are similar to those described for DBPD-6, with two significant peaks at low angles and the broad π-π stacking and alkyl halo peaks at high angles.

In contrast to the nematic phase of compound DBPD-6 and its clearly discernible schlieren textures, the polarized micrographs do not provide strong corroborating evidence for an explicit phase. As mentioned earlier, the dendritic structures present do not clearly associate with either rectangular or hexagonal columnar structures. Positive determination of the liquid crystalline ordering of DBPD-8 is further complicated by the compound's proclivity to form homeotropically aligned phases that obscure obvious 'snowflake'-type textures. It therefore falls upon XRD to provide supporting evidence as to the structure present which will in turn inform us as to the type of phase present.

After a fitting process similar to that discussed previously, the octyl dimer (DBPD-8) was also determined to have a columnar oblique structure. However, data collected at lower temperatures was essentially identical to that presented in Table 2-7. It was determined that due to the relatively small temperature range between the two mesophases that our X-ray data was of the Col_{ob} only. Experimental limitations of the

current apparatus prevented us from obtaining data of the higher temperature liquid crystal phase; it is assigned as columnar hexagonal since due to the dendritic structures and fluid behaviour observed by microscopy, and the DSC data indicating the presence of a mesophase at that temperature.

Table 2-7: X-ray Diffraction (XRD) results for DBPD-8.

Compound	Temperature (°C)	d-spacing (Å) Calculated	Observed	Assignment (hkl)	Phase
R=C_8	191	26.5	26.5	(1-1)	Col_{ob}
		18.9	18.9	(12)	(a = 43.4 Å, b = 39.2 Å,
		15.7	15.7	(22)	γ = 80.1°)
		14.2	14.1	(31)	
		12.5	12.1	(32)	
		12.0	11.4	(23)	
		9.4	9.5	(42)	
			4.9	*alkyl halo*	
			3.6	*π-π*	

2.3.3. DBPD-10 Results

Polarized Optical Microscopy

The sample with the longest alkyl constituents tends to homeotropically align to an even greater degree than DBPD-8. Very few birefringent regions can be seen in photomicrographs taken through crossed polarizers (Figure 2.12) at temperatures near the transition from isotropic, and the tendency to form these homeotropic domains is reproducible at different cooling rates.

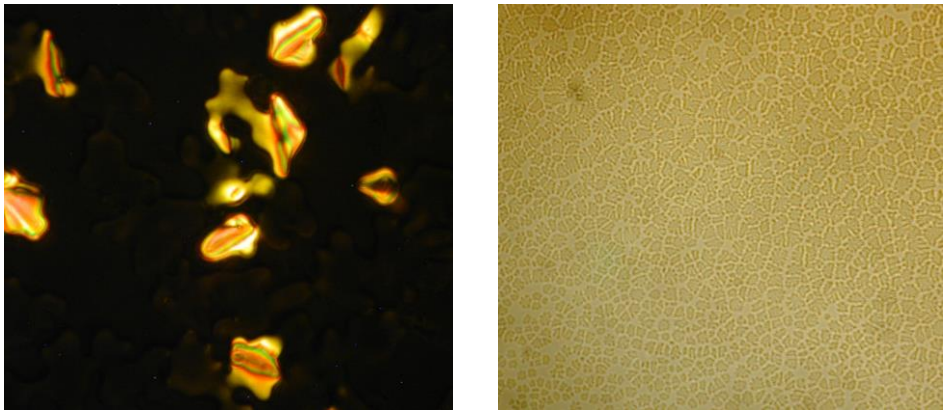

Figure 2.12: POM of DBPD-10. Left: Ambiguously textured growth of birefringent texture as seen through crossed polarizers (191.1° C, 80x magnification, -1° C/min) Right: Homeotropically aligned monodomains (black field in the left-hand photo)can be clearly seen when the polarizers are uncrossed. (~185° C, 8x magnification, -1° C/min)

The birefringent domains for this compound are also scattered over a large "black field", which upon uncrossing the polarizers is revealed to be a number of small, formless domains. Despite the clearly dendritic textures of both optical features they do not unambiguously characterize the mesophases present.

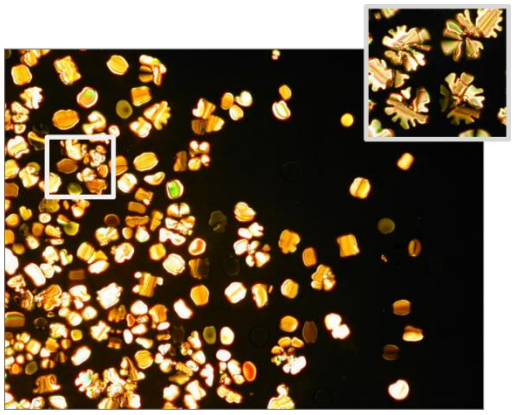

Figure 2.13: POM of DBPD-10 at lower temperature (174° C, 20x magnification, -0.1° C/min) showing black field background and birefringent domains. Inset: magnified view of ambiguous dendritic textures.

Differential Scanning Calorimetry

DBPD-10 is similar to the other dimer compounds in that it displays three peaks on heating and two on cooling. As with the other molecules in the series, diffuse peaks are observed for samples with thermal history but not the 1st heating. . The position of

these peaks and their enthalpies are consistent over a variety of heating and cooling rates.

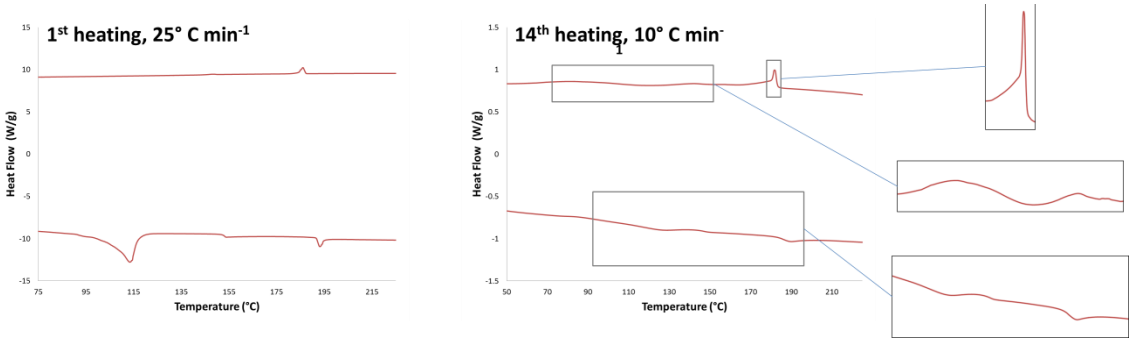

Figure 2.14: DSC traces for DBPD-10. Left: 1st heating, 25° C min-1. Right: sample with thermal history but reference rate of 10° C min-1.Right Insets: magnified view of diffuse peaks observed while heating and cooling.

The presence of multiple peaks indicate that at least one liquid crystal phase is present, as does the progression in enthalpies as reported in Table 2-8.

Table 2-8: Differential Scanning Calorimetry (DSC) results for DBPD-10 at 10°C/min. Transition: T_t, °C (Enthalpy, J/g)

Compound	Phase	Transition	Phase	Transition	Phase	Transition	Phase
DBPD-10 (R=$C_{10}H_{21}$)	Cr	113.4° (39.8) →	Col_{h1}	153.9° (0.7) ⇌ 148.1° (0.2)	Col_{h2}	193.2° (2.6) ⇌ 187.3° (1.7)	I

X-Ray Diffraction

XRD results for the C_{10} (DBPD-10) compound were markedly different than those obtained for the other two compounds. The single prominent peak at low angles is noticeably broader, and there are no significant secondary peaks save a broad shoulder. Due to instrument uncertainty with the temperature controller, in this run no lower temperature data was obtained. The characterization of Col_h is unchanged since this is in keeping with many reported examples of columnar hexagonal phases that do not exhibit a (110) peak.

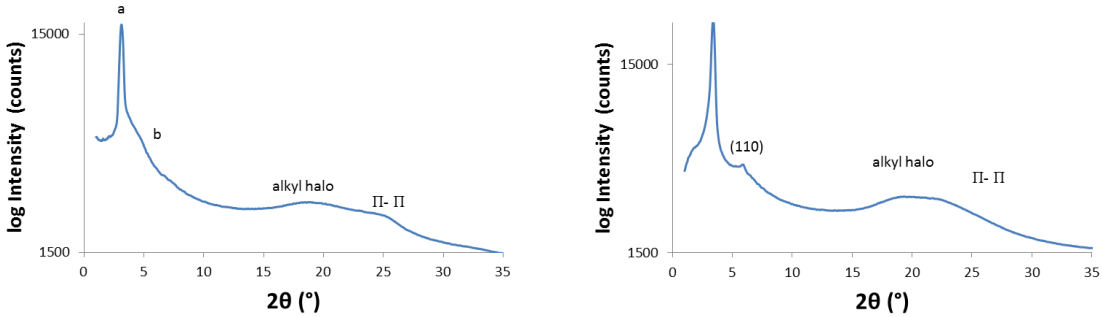

Figure 2.15: XRD diffractogram for DBPD-10 (left: 180° C). The prominent peak marked (a) corresponds to a Miller index of (100). A definite shoulder at (b) occurs at higher angles, followed by the usual alkyl halo and π-π stacking peaks. Right: DBPD-10 XRD at 116° C illustrating appearance of (110) peak.

A second run with a fresh sample to avoid thermal history was performed, and at lower temperatures (117° C) a secondary peak does emerge. This led us to identify the lower temperature phase as a distinct structure with its own unit cell parameters, as reported in Table 2-9.

Table 2-9: X-ray Diffraction (XRD) results for DBPD-10.

Compound	Temperature (°C)	d-spacing (Å)	Assignment (hkl)	Phase
DBPD-10	180	28.2	(100)	Col_h
		4.7	*alkyl halo*	(a = 32.6 Å)
		3.8	*π-π*	
	116	25.9	(100)	Col_h
		15.0	(110)	(a = 29.9 Å)
		4.5	*alkyl halo*	
		3.4	*π-π*	

2.3.4. Discussion

Upon viewing the series of dimers through crossed polarizers, a wide range of textures was discovered. Notable results included the presence of several textures including the relatively unstructured schlieren as well as more typical dendritic types. As a general trend the progressive lack of texture with increasing alkyl chain length was another significant feature of the data.

Although common for mesogenic molecules of all kinds, in this case the strong tendency for these dimer molecules to form glassy phases due to supercooling is significant. For DBPD-8 and DBPD-10, the glassy phase preserves the aligned columns formed in the liquid crystal phase which could be desirable for potential organic semiconducting devices. Further studies are required to determine the persistence of these glassy phases since DBPD-10 seems to have maintained this state for two months but XRD data is conflicting.

As mentioned previously (1.4.2), a tendency to homeotropically align is desirable for certain types of magnetic and optical applications, such as the construction of waveguides[79,80], polarizing layers, non-linear optical filters[81], and even ferroelectrics[82,83]. It is therefore quite significant that the studied dimers also show an unusual tendency to homeotropically align with the under- and over-lying substrates. This tendency has been observed previously but is uncommon in disc-shaped liquid crystals. Since XRD results ruled out the presence of a cubic structure, the featureless textures and relative dearth of birefringent domains observed in photomicrographs of DBPD-8 and DBPD-10are sufficient evidence of alignment in our molecules.

In the end, the peaks seen in the XRD results for compounds DBPD-6 and DBPD-8 were indexed to a columnar oblique phase with a γ near 90° using extensive calculations (available in the Appendix). The presence of a columnar oblique phase at lower temperatures for compounds DBPD-6 and DBPD-8 is extremely rare for discotic liquid crystals[84].

Despite the generally good agreement of the calculated Col_{ob} d-spacings to those observed, one perplexing aspect to the data was that there was no inverse relationship between peak intensity and 2θ. Commonly the most intense peaks at low angles correspond to Miller indices with ‘small‘ values. As stated earlier, the most common peaks observed for a columnar hexagonal phase start with the (100) peak, followed by the (110) and the (200). The (100) peak is the most intense and is observed at the smallest angle. The (200) peak, if present, is the least intense and is normally seen at the highest angle. Similar trends are common for cubic systems. Fortunately, despite their rarity within disc-shaped liquid crystals, there are a few published reports of oblique liquid crystalline phases within the field of bent-core molecules[85] as well as

metallomesogens[86]. It was reported that these bent-core molecules share these unusual behaviours and some have been shown to have 'non-traditional' Miller indices as the most intense peaks[87,88,89]. One example of this is the dipeptide derivative recently reported by Takezoe[43].

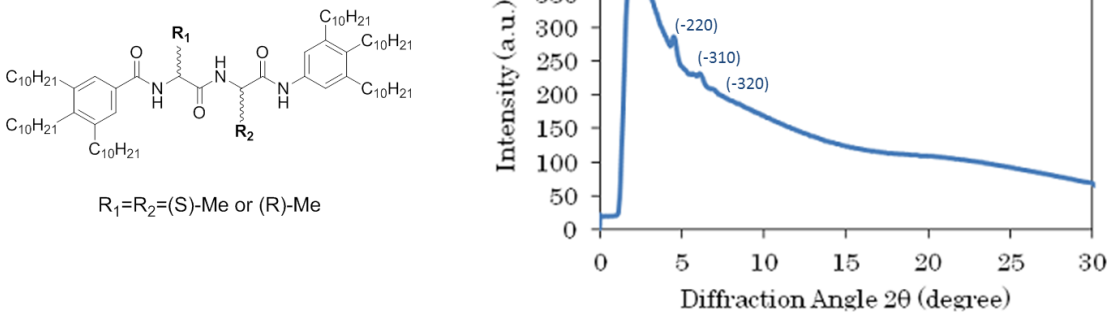

Figure 2.16: Dipeptide derivative found to form a Col_{ob} phase[87], with XRD diffractogram and assigned Miller indices including the unusual (-120) index as the most intense peak.

2.3.5. Molecular Modelling

Molecular modelling was performed. Using SPARTAN and the DFT basis set B3LYP 6-31G, the following lengths were calculated for the optimized geometry of these molecules: C_6 = 36.8 Å, C_8 = 41.7 Å and C_{10} = 46.5 Å.

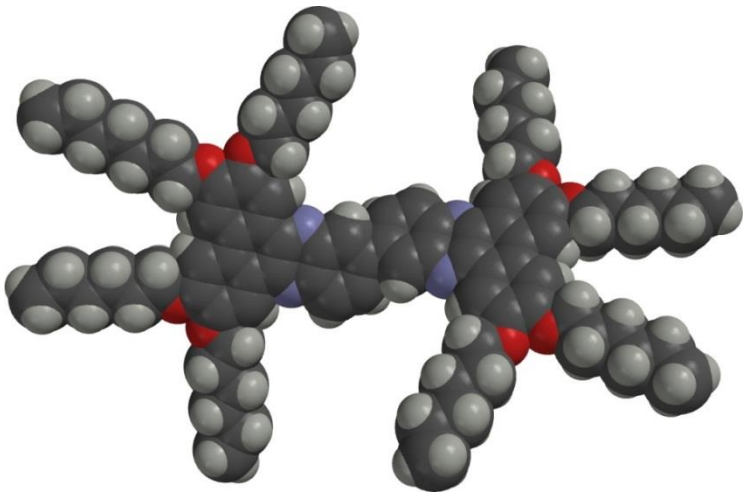

Figure 2.17: Space-filling model of DBPD-6 using SPARTAN.

Using Gaussian 09 to corroborate the results from Spartan, the core of the molecule without attached alkyl chains was optimized, resulting in a dihedral angle of 42° between rings. This is close to the literature value of 44° for biphenyl. The end result is not a flat planar molecule but a shape that is similar to that of a propeller, as illustrated in Figure 2.17.

The twisted geometry of the dimer may be important because several other liquid crystal systems with unusual shapes have been shown to behave differently from rod or disc shaped systems[90].

However, biphenyl systems themselves are only twisted in the gas phase[91,92], which is also the default phase for molecular modelling. The usual parameters for an ideal gas phase model such the elimination of intermolecular interactions are probably inapplicable to a neat liquid crystal phase; biphenyl systems have been shown to have little to no torsional angle in the presence of nematic liquid crystal solvents[93]. Such interactions between individual molecules are intrinsic to a self-assembled columnar phase, as are interactions between those columns on a larger scale. Nonetheless, computer modelling has shown the twisted conformation to be a viable alternative to a purely planar or elliptical shape. These possibilities must be kept in mind when attempting to provide future analysis of the packing behaviour of these molecule based on the obtained XRD parameters such as cell dimensions and Z. However, a comprehensive computational study of shape on the stacking effect taking into account

intermolecular and intercolumnar interactions would require a much more extensive model and is outside the scope of this thesis.

2.3.6. Conclusion

A series of dibenzophenazine dimers linked by a single, rigid carbon-carbon bond was presented in this chapter. These molecules exhibit a remarkable range of phase behaviour over a relatively small range of alkyl chain length, from unusual nematic and oblique mesophases for DBPD-6; DBPD-8 representing an intermediate stage with both oblique and columnar hexagonal LC phases; and finally the longest chain molecule DBPD-10 with only Col_h phases. With increasing alkyl chain length, the series tends towards more efficiently packed mesostructures as reflected by smaller unit cell parameters (40 Å to 29.9 Å).

One of the most striking features of the benzidine compounds is their propensity to form different types of liquid crystal phases that are rarely observed for disc-shaped mesogens[94]. For example, nematic phases such as those observed for DBPD-6 are more typically formed by rod-shaped molecules. Literature precedents for nematic phases exhibited by disc-shaped molecules involve molecules that include a metal center that disrupts packing of the molecular cores[95]. As mentioned earlier, our lab and Kumar's have reported dimers of linked disc-shaped molecule that also formed nematic phases; the present compounds appear to follow this trend since they represent the simplest possible covalently-linked dimer, and like those compounds can be thought of as having a shape approximating an ellipsoid.

Given that these molecules align homeotropically, it is also quite interesting that they form aligned monodomains on simply cleaned glass substrates. A primary application of discotic liquid crystals is electro-optical coatings for displays, in which they can be utilized to provide wide viewing angles and higher contrast ratios. In these circumstances it is quite desirable to attain a uniform alignment over the whole area of the device. Normally this is accomplished by the use of silane-treated or rubbed substrates – therefore the apparent tendency of these molecules to spontaneously align with untreated glass slides and cover slips is potentially useful.

The efficiency of devices that require such aligned domains are invariably improved with increasing homogeneity of the thin film. This is usually accomplished by 'freezing' the alignment in place through a variety of methods, including the previously described surface treatments, then subjecting the device to thermal annealing. This increases the uniformity since the smaller domains are simply converted into larger ones. However, a material whose tendency is to form large monodomains as opposed to many small domains would be an advantage over the annealing methods.

Another interesting result from the characterization of these molecules is their tendency towards polymorphism. Due to instrument limitations, it is beyond our capabilities to correlate multiple textures as observed via POM directly with those whose unit cells have been analyzed in the XRD. The temperature controller utilized cannot cool or heat at a specified rate – thus rendering certain mesomorphs unobservable in the XRD. There is also no way to observe the microscopic textures necessary to qualitatively confirm the phase being observed – for example, all columnar phases appear to be 'cloudy' on macroscopic visual inspection, but more than one columnar phase may be present. Despite this, it seems certain that the compounds studied are susceptible to the formation of polymorphs as evidenced by small, reproducible peaks in the DSC as well as distinct textures observed under crossed polarizers. Identification of these polymorphs would be interesting fodder for further studies.

2.4. Synthesis

The overall synthetic pathway for the synthesis of the Quinone-n material is presented in Scheme 2.4.

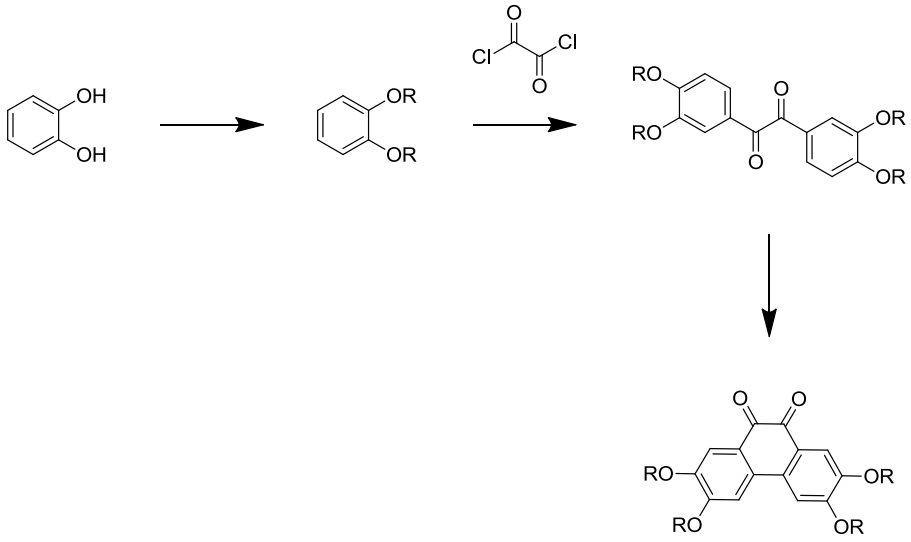

Scheme 2.4: Synthesis of phenanthrene dione from catechol.

General procedure for the preparation of 1,2-bis(alkyloxy)benzene (Alkoxy-n) derivatives:

The following procedure has been previously reported[96]. Catechol (45.4 mmol), bromohexane (99.9 mmol, 2.2 eq) and tetrabutylammonium bromide (4.5 mmol, 0.1 eq) were dissolved in butanone and purged with nitrogen for 10 minutes. Under positive N_2 pressure K_2CO_3 (204 mmol, 4.5 eq) was added and nitrogen bubbled through the mixture for 5 minutes. The suspension was stirred under reflux for 24 hours. The mixture was cooled to room temperature and poured over ice (250 mL). The organic phase washed three times with water (200 mL) and once with brine (150 mL). The organic phase was dried over $MgSO_4$, gravity filtered and concentrated under reduced pressure. The product was purified by column chromatography (eluent system hexanes:ethyl acetate ratio 96:4), forming a light yellow or orange oil.

1,2-bis(hexyloxy)benzene (Alkoxy-6):

As above where catechol (15.05 g, 136.7 mmol), bromohexane (40 mL, 279.6 mmol, 2.1 eq) and tetrabutylammonium bromide (4.42 g, 13.71 mmol, 0.1 eq) were reacted with K_2CO_3 (75.5 g, 546.3 mmol, 4 eq) to form a clear yellow oil (36.525 g, 131.2 mmol, 96% yield). ^{1}H NMR (500 MHz, $CDCl_3$) δ 6.91 – 6.85 (m, 4H), 3.99 (t, J = 6.7 Hz, 4H), 1.82 (dt, J = 14.7, 6.7 Hz, 4H), 1.52 – 1.44 (m, 4H), 1.40 – 1.29 (m, 8H), 0.94 – 0.87 (m, 6H).

1,2-bis(octyloxy)benzene (Alkoxy-8):

Here, catechol (10.0 g, 90.82 mmol), bromooctane (34.50 mL, 38.5854 g, 199.8 mmol, 2.2 eq) and tetrabutylammonium bromide (2.3422 g, 7.265 mmol, 0.1 eq) were reacted with K_2CO_3 (55.2288 g, 399.6 mmol, 4.4 eq) to form a clear, yellow tinted oil (25.2490 g, 75.47 mmol, 83% yield). ^{1}H NMR (500 MHz, $CDCl_3$) δ 6.91 – 6.89 (m, 4H), 4.01 (t, J = 6.7 Hz, 4H), 1.88 – 1.80 (m, 4H), 1.54 – 1.47 (m, 4H), 1.42 – 1.26 (m, 16H), 0.92 (dd, J = 7.2, 6.3 Hz, 6H).

1,2-bis(decyloxy)benzene (Alkoxy-10):

This molecule was synthesized and purified by Johan Foster and was previously reported[97].

General procedure for the preparation of 3,3',4,4'-tetraalkyloxybenzil (Benzil-n) derivatives:

Following literature procedure[98], Alkoxy-n (17.99 mmol) and $AlCl_3$ (10.80 mmol, 0.6 eq) were suspended in dry CH_2Cl_2 (125 mL) and purged with nitrogen for 15 minutes while stirring over an ice-water bath. Oxalyl chloride (2M, 9.800 mmol, 0.55 eq) was added dropwise by syringe and the reaction was left to slowly warm to room temperature. The reaction mixture was stirred for 24 hours, then poured over ice. The solution was extracted with dichloromethane (50 ml) three times and the extracts were combined and washed twice with water (200 mL) and once with brine (150 mL). The organic phase was dried over $MgSO_4$, gravity filtered and concentrated under reduced pressure. The product was purified over a short silica plug (eluent system distilled CH_2Cl_2), yielding a red-tinged white solid. The final fluffy white crystals were obtained by recrystallization from hot hexanes.

3,3',4,4'-tetrahexyloxybenzil (Benzil-6):

Alkoxy-6 (23.084 g, 82.30 mmol), $AlCl_3$ (6.60 g, 49.50 mmol, 0.6 eq) and oxalyl chloride (2M, 20 mL, 4.549 g, 35.84 mmol, 0.49 eq) were combined as described in the general procedure to afford the final product (18.59 g, 30.43 mmol, 73% yield). ^{1}H NMR (400 MHz, $CDCl_3$) δ 7.56 (d, J = 2.0 Hz, 2H), 7.43 (dd, J = 8.4, 2.0 Hz, 2H), 6.85 (d, J =

8.5 Hz, 2H), 4.06 (td, J = 6.6, 2.0 Hz, 8H), 1.90 – 1.77 (m, 8H), 1.46 (dd, J = 13.8, 8.2 Hz, 8H), 1.40 – 1.29 (m, 16H), 0.96 – 0.84 (m, 12H).

3,3',4,4'-tetraoctyloxybenzil (Benzil-8):

Alkoxy-8 (10.0 g, 16.86 mmol), $AlCl_3$ (2.4534 g, 18.40 mmol, 0.6 eq) and oxalyl chloride (2M, 8.45 mL, 2.1400 g, 16.86 mmol, 0.6 eq) were combined as described in the general procedure to afford the final product (5.8318 g, 8.065 mmol, 54% yield). ^{1}H NMR (400 MHz, $CDCl_3$) δ 7.56 (d, J = 2.0 Hz, 2H), 7.43 (dd, J = 8.4, 2.0 Hz, 2H), 6.84 (d, J = 8.5 Hz, 2H), 4.05 (td, J = 6.6, 3.2 Hz, 8H), 1.88 – 1.79 (m, 8H), 1.50 – 1.41 (m, 8H), 1.40 – 1.23 (m, 32H), 0.88 (td, J = 7.0, 4.6 Hz, 12H).

3,3',4,4'-tetradecyloxybenzil (Benzil-10):

Alkoxy-10 (10.0 g, 25.60 mmol), $AlCl_3$ (1.3670 g, 10.25 mmol, 0.4 eq) and oxalyl chloride (2M, 4.90 mL, 1.243 g, 9.794 mmol, 0.4 eq) were reacted together as described, forming the final orange-white powder (3.2730 g, 3.918 mmol, 31% yield). ^{1}H NMR (500 MHz, $CDCl_3$) δ 7.57 (d, J = 2.0 Hz, 2H), 7.43 (dd, J = 8.4, 2.0 Hz, 2H), 6.85 (d, J = 8.4 Hz, 2H), 4.06 (td, J = 6.6, 2.4 Hz, 8H), 1.87 – 1.80 (m, 12H), 1.47 (s, 12H), 1.34 (dt, J = 7.3, 3.5 Hz, 24H), 1.25 (s, 8H), 0.94 – 0.87 (m, 20H).

General procedure for the preparation of 2,3,6,7-tetraalkyloxyphenanthrene-9,10-dione (Quinone-n) derivatives:

The following procedure has been previously reported[98,99,100]. Benzil-n (3.806 mmol) was dissolved in dry CH_2Cl_2 (100 mL) under a nitrogen atmosphere in a ice/water bath. BF_3•Et_2O (12.30 mmol, 3.2 eq) was added using a syringe and the mixture was allowed to stir for ten minutes. VOF_3 (11.50 mmol, 3 eq) was then added and the mixture was stirred for two hours.The reaction mixture was poured over an aqueous solution of citric acid (10 g / 100 mL) and stirred for another hour or overnight. The solution was extracted by dichloromethane (50 ml) three times and the extracts were combined and washed twice with water (200 mL) and once with brine (150 mL). The organic phase was dried over $MgSO_4$, gravity filtered and concentrated under reduced pressure. The product was purified by column chromatography (eluent system distilled CH_2Cl_2),

yielding a red solid The final purple-red needle-like crystals were obtained by recrystallization from hot acetone.

2,3,6,7-tetrahexyloxyphenanthrene-9,10-dione (Quinone-6):

As described in the general procedure Benzil-6 (2.322 g, 3.806 mmol) was reacted in the presence of BF_3•Et_2O (12.30 mmol, 3.2 eq) and VOF_3 (11.50 mmol, 3 eq) to form a final product of purple-red crystalline needle (2.0738 g, 3.399 mmol, 90% yield). ^{1}H NMR (400 MHz, $CDCl_3$) δ 7.55 (s, 2H), 7.11 (s, 2H), 4.13 (dt, J = 46.1, 6.6, 6.6 Hz, 8H), 1.95 – 1.79 (m, 8H), 1.53 – 1.45 (m, 8H), 1.36 (s, 16H), 0.92 (s, 12H).

2,3,6,7-tetraoctyloxyphenanthrene-9,10-dione (Quinone-8):

This molecule was prepared by Kevin Bozek from the aforementioned Benzil-8 (2.132 g, 2.43 mmol) with VOF_3 (1.210 g, 9.761 mmol, 3.3 eq) and BF_3•Et_2O (0.937 mL, 0.739293 g, 5.2089 mmol, 1.8 eq). Purple crystals were recovered after recrystallization from hot acetone (1.326 g, 1.839 mmol, 63% yield) ^{1}H NMR (400 MHz, $CDCl_3$) δ 7.54 (s, 2H), 7.11 (s, 2H), 4.13 (dt, J = 46.9, 6.5, 6.5 Hz, 8H), 1.96 – 1.79 (m, 8H), 1.51 (ddd, J = 23.6, 15.3, 7.8 Hz, 16H), 1.43 – 1.21 (m, 24H), 0.89 (dd, J = 8.6, 4.6 Hz, 12H).

2,3,6,7-tetradecyloxyphenanthrene-9,10-dione (Quinone-10):

This molecule was prepared by Christine Laviguer, as reported. ^{1}H NMR (400 MHz, $CDCl_3$) δ 7.54 (s, 2H), 7.11 (s, 2H), 4..20-4.06 (dt, J = 46.9, 6.5, 6.5 Hz, 8H), 1.96 – 1.79 (m, 8H), 2.00-1.74 (ddd, J = 23.6, 15.3, 7.8 Hz, 8H), 1.43 – 1.18 (m, 48H) 0.89 – 0.86 (t J = 8.6, 4.6 Hz, 12H).

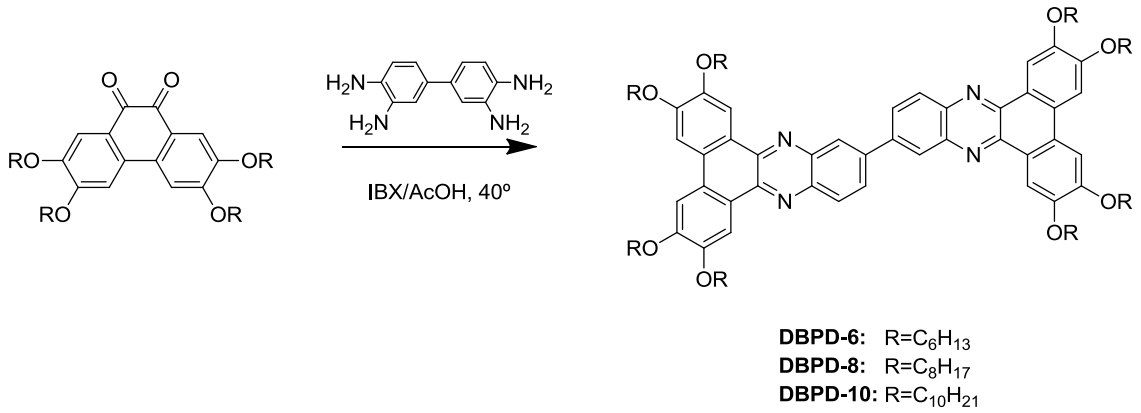

Scheme 2.5: Synthesis of dibenzophenazine (DBP) dimers 1a-1c from the phenanthrene dione with varying alkoxy chain lengths.

General procedure for the synthesis of 2,2',3,3',6,6',7,7'-octakis(alkyloxy)-11,11'-bidibenzo[a,c]phenazine also known as benzidine dimer compounds (DBPD-n):

The Quinone-C_n (0.1232 mmol) was added along with 3,3'-diaminobenzidine (0.0587 mmol, 0.48 eq) and a catalytic amount of *o*-iodoxybenzoic acid (0.0110 mmol) to dry CH_2Cl_2 (~25 ml). A water condenser was fitted to the RBF and the resulting red-black solution was stirred open to the atmosphere over an oil bath maintained at 40°C overnight. The resulting solution was extracted by chloroform (50 ml) twice and the extracts combined and washed once with water (100 mL), followed by 10% HCl solution (100 mL), once again with water and finally with brine (100 mL). The organic phase was dried over $MgSO_4$, gravity filtered and concentrated under reduced pressure. The solid product was purified by column chromatography (eluent system EtOAc:hexanes ratio 1:4), yielding an orange-yellow solid. Fractions containing the final product were concentrated under reduced pressure, then left to stand in ether overnight. The purified product was recovered by centrifugation.

2,2',3,3',6,6',7,7'-octakis(hexyloxy)-11,11'-bidibenzo[a,c]phenazine (DBPD-6):

As described above, a portion of 3,3'-diaminobenzidine (0.1998 g, 0.1503 mmol) was reacted with Quinone-6 (0.1998 g, 0.3282 mmol, 2.2 eq) was added along with the catalyst o-iodoxybenzoic acid (0.0040 g, 0.0158 mmol, 0.1 eq) to produce the final

orange solid (0.0430 g, 0.0316 mmol, 21% yield). ^{1}H NMR (600 MHz, $CDCl_3$) δ 8.95 – 8.74 (m, 6H), 8.42 (dd, J = 54.1, 8.7 Hz, 4H), 7.75 (s, 4H), 4.41 – 4.13 (m, 16H), 2.06 – 1.94 (m, 16H), 1.61 (s, 16H), 1.43 (d, J = 6.7 Hz, 32H), 0.95 (q, J = 6.9 Hz, 24H); ^{13}C NMR (151 MHz, $CDCl_3$) δ 152.05, 152.03, 149.67, 149.66, 142.64, 142.25, 142.24, 142.23, 141.95, 141.49, 140.56, 129.86, 128.91, 128.89, 127.49, 126.81, 124.04, 124.00, 108.95, 108.87, 106.66, 106.65, 69.84, 69.81, 69.34, 69.30, 31.84, 29.50, 29.45, 26.03, 26.02, 25.98, 22.83, 22.82, 14.23, 14.21; MALDI-TOF for [$C_{88}H_{118}N_4O_8$] calculated (found): 1359.89 (1359.67); HR-MS for [$C_{88}H_{118}N_4O_8$-H^+] calculated (found): 1359.9022 (1359.9022).

2,2',3,3',6,6',7,7'-octakis(octyloxy)-11,11'-bidibenzo[a,c]phenazine (DBPD-8):

For this compound 3,3'-diaminobenzidine (0.0206 g, 0.0961 mmol) was reacted with Quinone-8 (0.1478 g, 0.2050 mmol, 2.1 eq) and *o*-iodoxybenzoic acid (0.0029 g, 0.0114 mmol, 0.1 eq) to produce the final yellow powder (0.0554 g, 0.0350 mmol, 36% yield). ^{1}H NMR (600 MHz, $CDCl_3$) δ 8.91 – 8.76 (m, 6H), 8.41 (dd, J = 53.3, 8.0 Hz, 4H), 7.74 (s, 4H), 4.45 – 4.14 (m, 16H), 1.98 (d, J = 14.3 Hz, 16H), 1.60 (s, 16H), 1.44 (s, 16H), 1.35 (d, J = 31.2 Hz, 48H), 0.90 (dd, J = 11.2, 5.6 Hz, 24H); ^{13}C NMR (151 MHz, $CDCl_3$) δ 152.05, 152.04, 149.68, 149.66, 142.64, 142.23, 141.96, 141.48, 140.58, 129.96, 128.90, 127.48, 126.82, 126.81, 124.05, 124.00, 108.96, 108.91, 106.70, 106.67, 69.85, 69.83, 69.35, 69.31, 32.05, 32.02, 29.66, 29.57, 29.52, 29.50, 26.37, 26.37, 26.34, 22.88, 22.86, 14.29, 14.27; MALDI-TOF for [$C_{104}H_{150}N_4O_8$] calculated (found): 1584.15 (1584.09); HR-MS for [$C_{104}H_{150}N_4O_8$-H^+] calculated (found): 1585.1560 (1585.1560).

2,2',3,3',6,6',7,7'-octakis(decyloxy)-11,11'-bidibenzo[a,c]phenazine (DBPD-10):

3,3'-diaminobenzidine (0.0182 g, 0.0849 mmol) was reacted with Quinone-10 (0.1434 g, 0.1721 mmol, 2 eq) and *o*-iodoxybenzoic acid (0.0023 g, 0.0091 mmol, 0.1 eq), affording a yellow-orange powder (0.0349 g, 0.0193 mmol, 23% yield). ^{1}H NMR (600 MHz, $CDCl_3$) δ 8.88 – 8.77 (m, 6H), 8.41 (dd, J = 53.1, 8.7 Hz, 4H), 7.74 (s, 4H), 4.44 – 4.23 (m, 16H), 1.99 (dd, J = 16.5, 9.3 Hz, 16H), 1.67 – 1.57 (m, 16H), 1.44 (t, J = 10.2 Hz, 24H), 1.38 (s, 16H), 1.35 – 1.27 (m, 56H), 0.94 – 0.78 (m, 24H); ^{13}C NMR (151

MHz, $CDCl_3$) δ 152.03, 152.02, 149.67, 149.65, 142.63, 142.22, 141.95, 141.46, 140.56, 129.95, 128.89, 128.88, 127.48, 126.81, 126.79, 124.04, 123.99, 108.95, 108.88, 106.67, 106.66, 69.84, 69.83, 69.34, 69.30, 32.12, 32.10, 32.09, 29.87, 29.80, 29.71, 29.70, 29.57, 29.55, 29.52, 29.51, 26.39, 26.37, 26.35, 22.86, 22.85, 14.29, 14.27, 14.26; MALDI-TOF for [$C_{120}H_{182}N_4O_8$] calculated (found): 1808.40 (1808.04); HR-MS for [$C_{120}H_{182}N_4O_8$-H^+] calculated (found): 1809.4064 (1809.4064).

3. Amide Monomers

3.1. Introduction

The work carried out for this thesis was primarily concerned with rigid, covalently-linked dimers. The benzidine-derived system presented in the previous chapter was essentially a minimal length linker between the two dibenzophenazine cores. Formation of future dimers will most likely be through synthetically accessible functional groups that will make the bridge between disc-shaped molecules at least one atom long.

As mentioned previously, several studies have reported flexible bridges between predominantly triphenylene cores. However, even in the case of a rigid linker, a baseline needs to be established in order to ascertain whether the behaviour of the dimer is significantly different than the monomers from which it is composed. This is especially important in the case of amide compounds in which hydrogen bonding may occur intermolecularly or intramolecularly. In general, we wish to decouple the influence of simple alterations in geometry due to extension or contraction of alkyl chains as opposed to those due to dimer formation. For example, the acetylene linked molecule reported by Kumar would benefit from comparison with the behaviour of a single acetylene functionalized triphenylene.

As discussed in the previous chapter, one of the most compelling reasons to study discotic dimers is their apparent propensity to form unusual liquid crystal phases. One possible mechanism for this phenomenon is the expansion of the overall shape of the dimer when compared to the basic disc shape of a typical monomer. In the case of rigid dimers, elongation is theorized to be responsible for disrupting the normal packing modes observed for monomeric molecules, often resulting in rarely observed phases such as the oblique and nematic mesophases. For example, in the contrasting case of a flexibly linked dimer, intramolecular stacking can result in a conformation that might not be demonstrably different than a stack of two free monomers. Studying the phase

behaviour of the monomer is therefore crucial to confirm the validity of dimer formation as a causal factor for any unusual phases.

Dimers may also be formed via functional groups that offer ease of synthesis as well as the potential for intra- or intermolecular interactions such as hydrogen bonding. Since these effects can overwhelm the usual π-π effects that dominate liquid crystal formation, they might represent factors competing with the extended shape of the dimer. One example of this is amide-linked dimers (Figure 3.1) which could afford both rigid and flexible bridges through well-known amidation pathways.

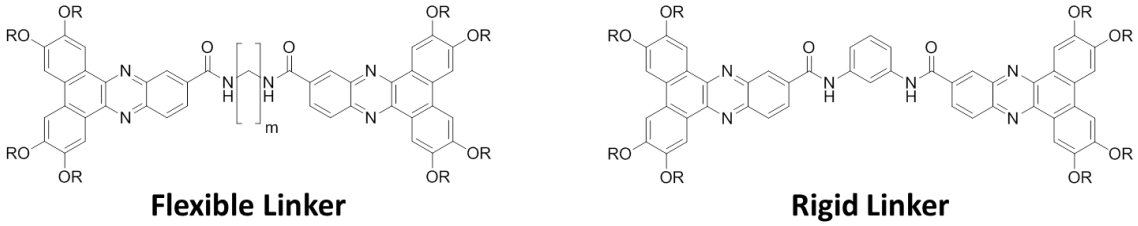

Figure 3.1: Examples of potential flexible and rigid linkers connecting dibenzophenazine cores via amide functional groups.

In the present chapter, a series of amide monomers with a single DBP core (Scheme 3.1) was synthesized to serve as a reference for amide bridged dimers. Note that the peripheral alkoxy chains for all molecules in the series have seven carbons. Therefore they are distinguished from each other by the length of alkyl chain decorating the amide moiety, and will hereafter be referred to as (**Mono-n**), where 'n' denotes the length of that alkyl chain.

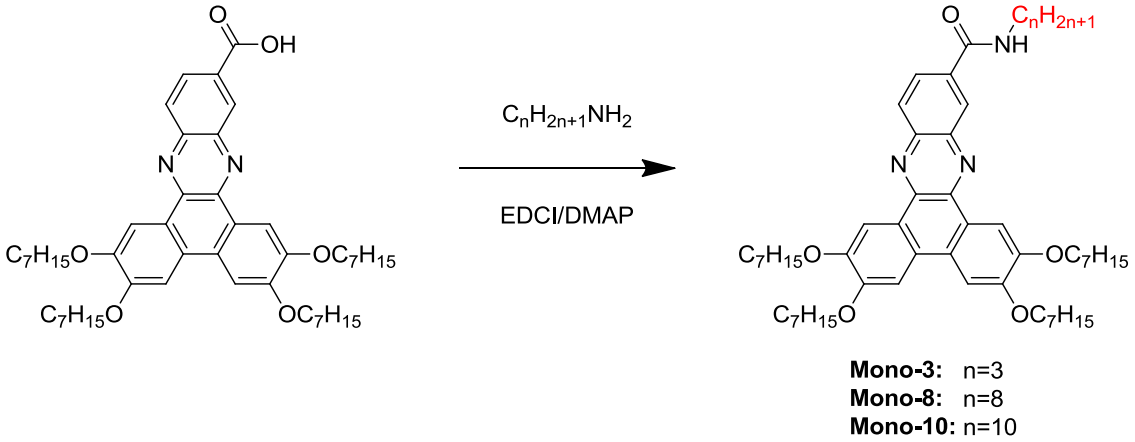

Scheme 3.1: Final synthetic pathway for the synthesis of the amide monomer series, except Mono-2 (Scheme 3.4a).

3.2. Synthesis

A dibenzophenazine core functionalized with a carboxylic acid group was attractive since it opened up potential synthetic pathways to dimer molecules through the formation of ester, amide, and numerous other moieties.

The quinone with heptyl side chains (**Quinone-7**) was condensed with 3,4-diaminobenzoic acid to produce the dibenzophenazine structure decorated with a carboxylic acid functional group in quantitative yields (Scheme 3.2).

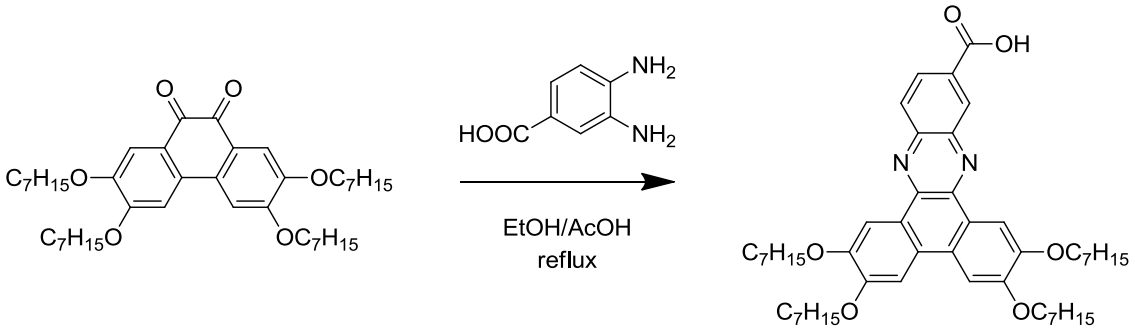

Scheme 3.2: Synthesis of carboxylic acid functionalized DBP core (Acid-7).

With the acid in hand, initial efforts centered on the subsequent formation of the acid chloride. Thionyl chloride proved to be too harsh for this reaction, so oxalyl chloride was used instead; catalytic amounts of DMF were found to aid the oxalyl chloride

reaction. In the same reaction vessel, the acid chloride was first dried under vacuum to remove excess oxalyl chloride, then reacted with the appropriate amine added as a solution with pyridine in dry dichloromethane. In the case of reactions with the smaller 1-ethylamine and 1-propylamine, this reaction proved inefficient and initial trials yielded only the acid chloride despite the use of a large excess of amine. This was attributed to the fact the amine was in the form of the hydrochloride salt. Use of Schotten-Baumann conditions (two-phase, in which the acid chloride mixture in organic solvent is added directly to a mixture of the target amine dissolved in concentrated aqueous NaOH over several additions) resulted in a more efficient synthesis.

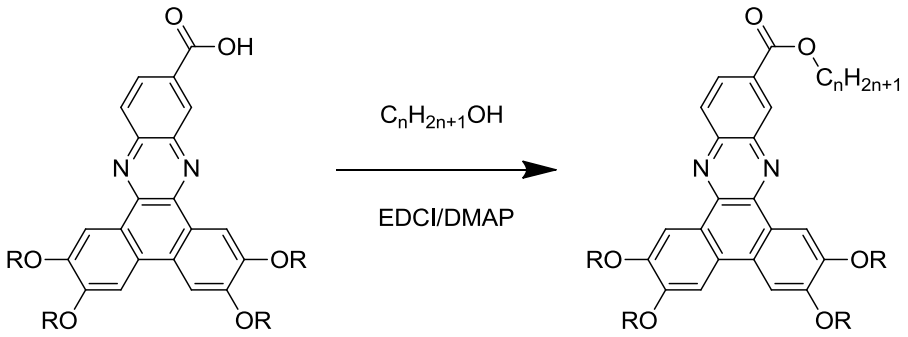

Scheme 3.3: Esterification pathway developed in Williams lab by Kevin Bozek.

However, both methods were ineffective in reactions with longer chain amines. Other workers in the Williams Group had been studying esterification reactions from the same DBP starting point (Scheme 3.3). They found that the use of EDCI/DMAP greatly simplified the reaction as well as improved the yield. This method turned out to have similar outcomes for the amidation reactions and was used in the final synthesis of all molecules except Mono-2, for which sufficient material had already been produced using the pathway described in Scheme 3.4(b).

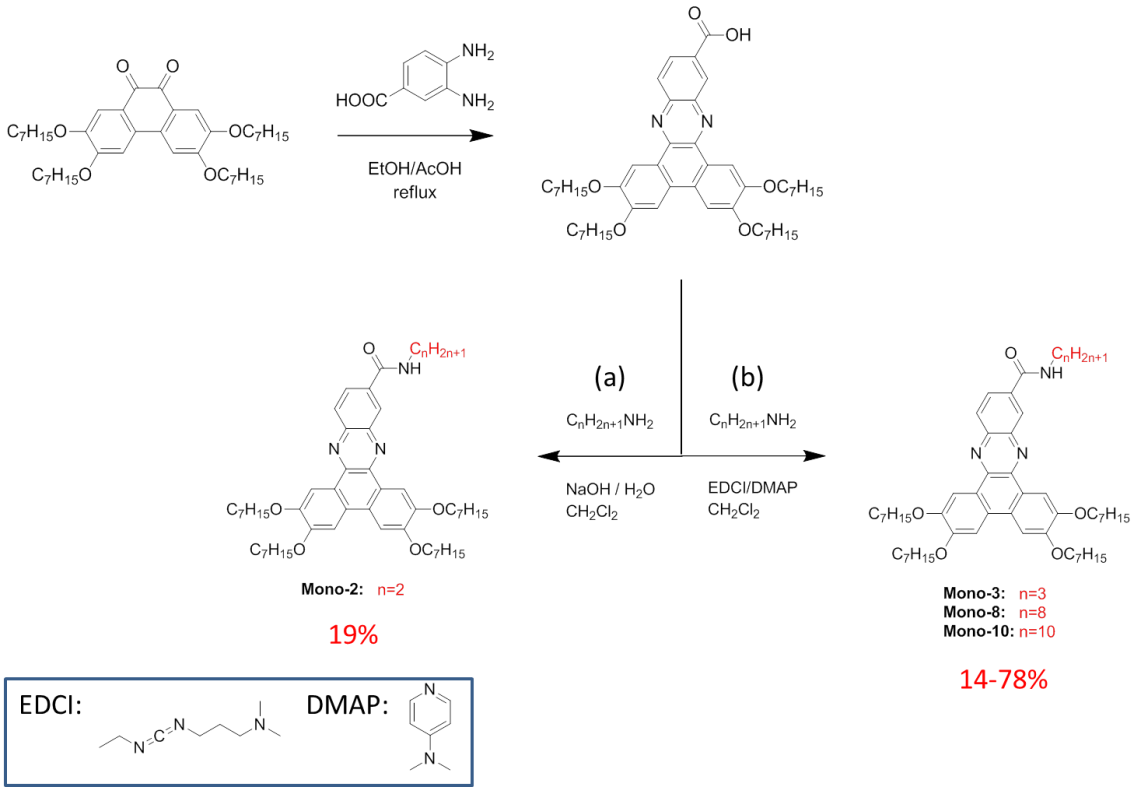

Scheme 3.4: Final synthetic pathways utilized. The first approach (a) used Schotten-Baumann conditions (addition to aqueous NaOH) with the acid chloride added as prepared to afford Mono-2. The second approach (b) used the EDCI/DMAP pathway for the remaining molecules.

3.3. Results and Discussion

The liquid crystalline properties of each molecule were characterized by polarized optical microscopy (POM, 1.5.1), differential scanning calorimetry (DSC, 1.5.2) and variable-temperature X-ray diffraction (VT-XRD) as described in the introduction (1.5.3).

In order to better illuminate the trends in phase behaviour for amide monomers, it is useful to include other molecules that can fill in the gaps between the short-chain and long chain amide monomers presented in this thesis even though these molecules are yet to be reported. Additional amide monomers have been synthesized by other members of the Williams group, including C_6 and C_{14} (prepared by Komi Chandi) as well as the C_6, phenyl, and diisopropyl monomers (prepared by Karl Kuppers) and pertinent

information from those studies will be used to provide context for results discussed in this thesis where appropriate.

3.3.1. Polarized Optical Microscopy

Generally the photomicrographs taken of the compounds through crossed polarizers had a distinct lack of texture, with only a few small and scattered needle-shaped areas that possessed birefringence. A representative POM image is shown in Figure 3.2.

Figure 3.2: POM images of Mono-2, textures shown were typical for the monomer series. A birefringent portion of a domain is outlined (circle) for reference. Left: Ambiguously textured growth of birefringent texture (147.4° C, 20x magnification, Crossed, -1° C/min) Right: Formation of homeotropically aligned dendritic textures with six-fold symmetry. (147.4° C, 20x magnification, Uncrossed, -1° C/min)

Recall that liquid crystal phases are inherently birefringent – therefore the textures observed through crossed polarizers provide important information about the potential presence and possible structure of liquid crystal phases. Thus, the absence of structure when observed through crossed polarizers indicates either the presence of a isotropic phase or sample-wide homeotropic alignment. Photomicrographs taken through parallel polarizers (Figure 3.3) show the presence of domains that grow in a dendritic manner and appear to possess six-fold symmetry.

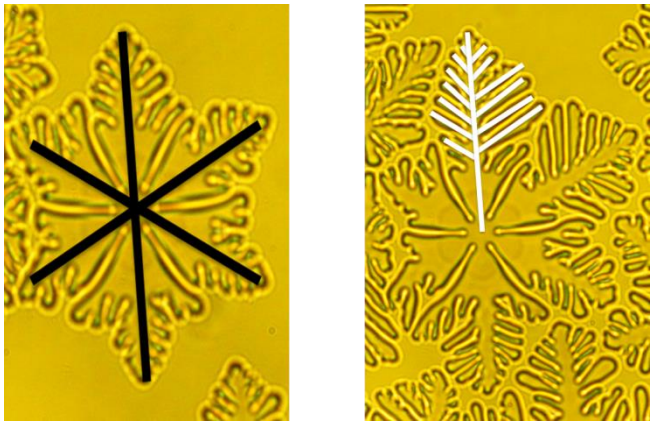

Figure 3.3: Detailed view of dendritic structures shown in Figure 3.2. Left: six-fold symmetry emphasized with black lines indicating first branching point of dendritic texture. Right: secondary dendritic branch formation, highlighted by white lines showing similar inclination angles to the primary branching.

Assuming that the domains are columnar, the only way they would result in no texture is if we are viewing them top-down along the long-axis of the columns, much like looking down the shaft of an arrow. Therefore from the POM observations we can reasonably conclude that the domains are homeotropically aligned with the substrate.

The presence of homeotropic alignment for all members of the series is significant since this type of self-assembled structure is desirable for many organic semiconducting applications as described in previous sections (1.4.2). At this point it is useful to consider the other amide monomers synthesized in the Williams lab. All of these examples possess some degree of homeotropic alignment with the exception of the extremely long chain C_{14} molecule. On one hand, the presence of the amide group appears to have some role in the molecule's tendency to align with the underlying substrate since such alignment is observed for the majority of molecules studied, and similar alignment is not observed for comparable ester monomers published by previous group members.

Amide-amide intermolecular interactions are classically thought to be stronger than those between esters since non-tertiary amides may undergo hydrogen bonding in addition to resonance-stabilized dipole-dipole interactions[101]. However, even without hydrogen bonding, the smaller C-N dipole of the amide cancels out less of the dominant C=O dipole which is why amides typically have boiling points higher than those of

carboxylic acids[102]. Thus, a reasonable assertion is that the larger dipole of the amide group is largely responsible for the high degree of homeotropic alignment in the amide monomer series.

Although it is reasonable to infer that the amide group has some role in homeotropic alignment, it is probably not due to hydrogen bonding effects due to that particular group since the unpublished Kuppers monomer di-substituted with isopropyl groups (Mono-DiPr) maintains homeotropic alignment.

The absence of aligned domains for the sample decorated with the longest alkyl chain (the C_{14} monomer synthesized by Komi Chandi, Mono-14) indicates that there is some threshold length for the peripheral alkyl chain after which the spontaneous orientation of the film is disrupted.

An important note is that even at long chain lengths, the textures seen consistently exhibited six-fold symmetry and dendritic growth whether the domains were random or aligned. These observations usually point towards the presence of a columnar hexagonal phase which is the most common morphology observed for discotic mesogens[103]. Therefore, beyond the presence of spontaneous alignment perpendicular to the substrate, no unusual phases were suggested by POM data.

3.3.2. Differential Scanning Calorimetry

DSC analysis was performed on the synthesized molecules. Typical traces (Figure 3.4) revealed a distinct difference between the behaviour of the short-chained amides (C_2 and C_3) versus long-chain amides (C_8 and C_{10}). Most notably, the C_2 and C_3 molecules exhibited two significant peaks on heating whereas the C_8 and C_{10} molecules had at least three. Recall that multiple peaks in these traces suggest the presence of a liquid crystalline phase, which supports the POM observations.

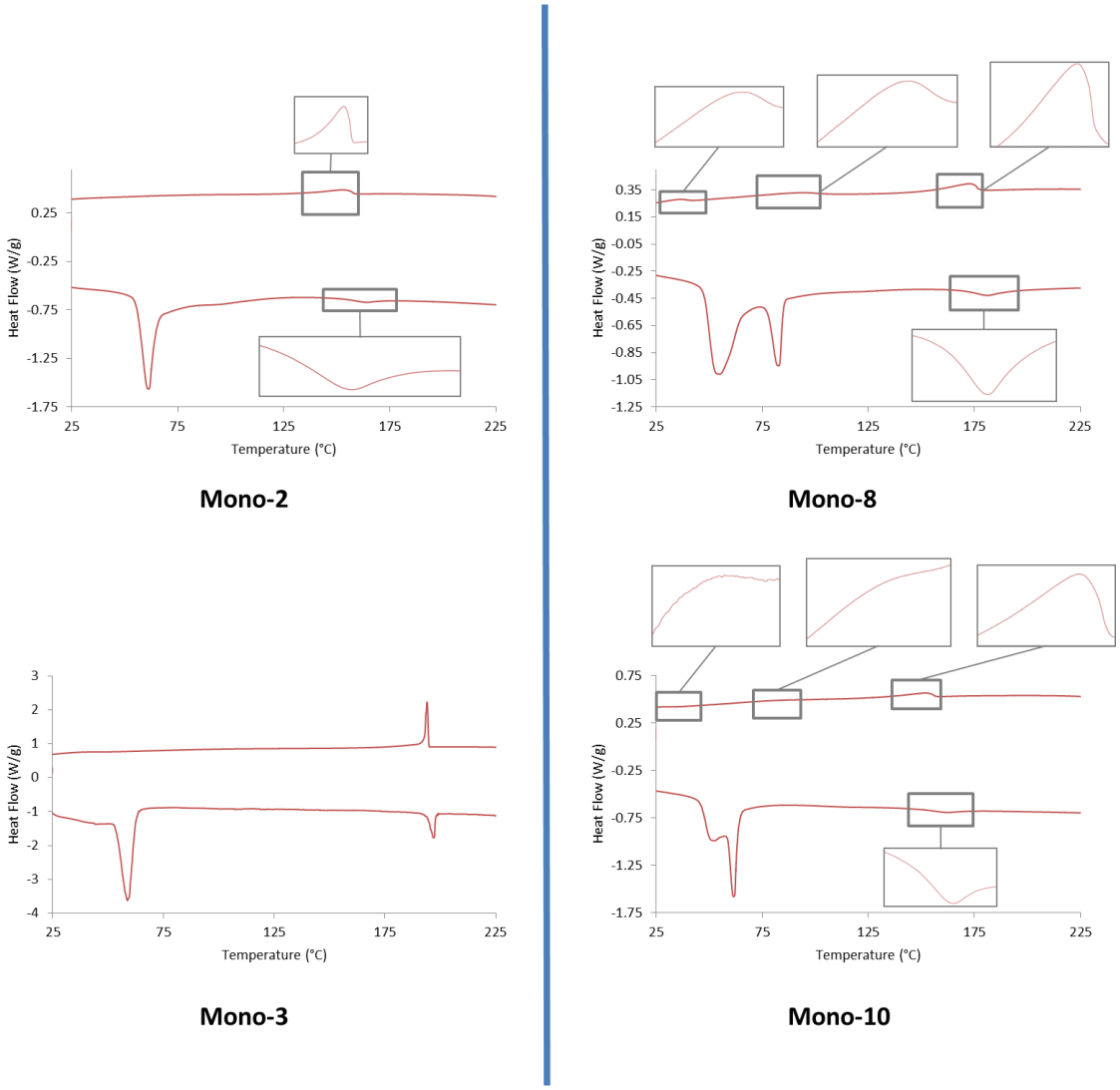

Figure 3.4: Second heating cycle DSC traces for the monomer series. Left: Mono-2 (top) and Mono-3 (bottom) with two peaks on heating and one on cooling. Right: Mono-8 (top) and Mono-10 (bottom) with two significant peaks where the melting transition is expected, and three peaks on heating overall. The long chain molecules also have three diffuse peaks on cooling.

However, upon careful re-analysis of the data it was apparent that many of the diffuse peaks reported, while unquestionably present, had erroneous enthalpy values. This error was a result of assuming that the baselines for the data were flat, when in fact they were sloped. This assumption led to the integration of peaks over unreasonable temperature ranges; in turn the reported enthalpies were inflated.

Like the dimer series, thermal history of the DSC samples is an important consideration. Unlike the dimer series the first heating data obtained for the monomer series were affected by faulty calibration of the instrument after it had been moved in the lab. All first heating traces are included in Appendix B for examination, but that data was deemed unsuitable for interpretation due to extremely sloped baselines and unrealistically low millijoule values for all enthalpies. This was confirmed by comparison to a known Mono-6 compound synthesized by Karl Kuppers (Table 3-1). This experiment revealed that the location of the peaks was consistent despite the machine falling out of calibration but the enthalpy was off by two orders of magnitude. The traces presented in Figure 3.4 are the second heating cycle for all compounds performed after the apparatus had been re-calibrated.

Table 3-1: Comparison of DSC results for known compound Mono-6 before and after apparatus was moved. Left: Temperature results before (T_{known}) and after (T_{test}). Right: Enthalpy results before (ΔH_{known}) and after (ΔH_{test}).

	T_{known}	T_{test}	ΔT
Heating	79.3	79.1	0.2
	223.0	223.2	-0.2
Cooling	227.0	226.6	0.4
	144.2	129.6	14.6

	ΔH_{known}	ΔH_{test}	% Error ΔH_{known} / ΔH_{test}
Heating	11.7	0.2	1.4%
	5.5	0.1	1.3%
Cooling	2.8	0.04	1.5%
	59.1	0.3	0.5%

Since first heating results were not available, the traces were integrated again taking into account that the peaks were forming out of sloped baselines (Figure 3.5). In the case of virtually every broad peak, the values observed after repeating integration were so low that they could not be considered to be significant. Taking into account the sloped baseline, the enthalpy decreased from 1.2 J/g to 0.3 J/g and was removed from the analysis as a major transition on that basis. Culling these peaks vastly simplified the DSC data, and the final assignment is reported in Table 3-2.

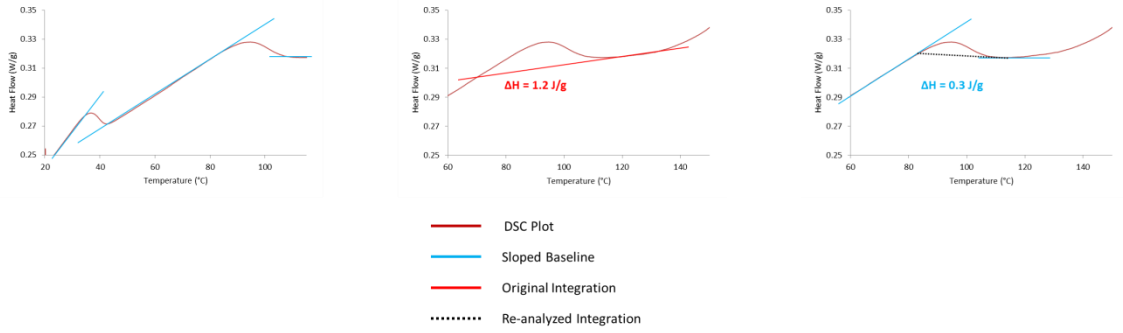

Figure 3.5: Typical peak analysis using Mono-8 data from Figure 3.4. Left: Zoomed view of cooling curve showing sloped baselines. Center: Original integration limits. Right: Integration limits after re-analysis.

Since assignment of a second columnar hexagonal phase was based primarily on the existence of distinct peaks with expected enthalpy values, it is far more plausible that there is only one Col_h phase and that the initial assignment of a second liquid crystal phase was mistaken. As will be discussed in detail in the next section (3.3.3), this simpler phase behaviour also explains the lack of dimensional variation in the XRD results.

Despite the multiple heating and cooling cycles, the presence of a liquid crystal phase is bolstered by the general trend in the enthalpy data – in every case the observed transitions decrease in enthalpy, as expected for a progression from a highly ordered crystalline solid to a liquid crystal phase and to an isotropic liquid. The individual enthalpies are also within the range of commonly accepted values for melting (20-30 kJ/mol) and clearing (1-5 kJ/mol) temperatures for liquid crystal phases[104]. A notable exception is the longer chain compounds, whose lowest temperature peaks possess moderate enthalpies that would normally accompany a LC-LC transition. These peaks were determined to be Cr-Cr transitions after consideration of the X-ray data. The assignment of the second peak for these longer chain compounds as a Cr-LC transition is supported by the extremely low enthalpy of the third peak at high temperature; if such a peak represented a change from a crystalline solid to an isotropic liquid we would expect a very sharp peak with high enthalpy.

Table 3-2: DSC results for the amide monomer series at 10°C/min. Transition: T_t, °C (Enthalpy, J/g)

Compound	Phase	Transition	Phase	Transition	Phase	Transition	Phase
Mono-2 (n=C_2H_5)	Cr	61.0° (26.3) →	Col_h	163.8° (1.0) ⇌ 153.0° (0.8)	I		
Mono-3 (n=C_3H_7)	Cr	58.7° (24.1) →	Col_h	197.0° (3.8) ⇌ 194.0° (3.2)	I		
Mono-8 (n=C_8H_{17})	Cr_1	53.5° (21.0) →	Cr_2	82.9° (7.7) →	Col_h	181.4° (3.2) ⇌ 172.6° (2.7)	I
Mono-10 (n=$C_{10}H_{21}$)	Cr_1	50.5° (15.7) →	Cr_2	62.0° (12.6) →	Col_h	161.6° (1.6) ⇌ 151.7° (2.5)	I

Traces also had fewer peaks on cooling than heating, as well as a shift of the clearing transition to lower temperatures on cooling. This indicates that they all showed some degree of super-cooling which is not unusual for mesophases. However, it is significant that they maintain a glassy state on cooling since this would preserve the desirable arrangement of the aligned domains created in the liquid crystal phase.

In order to further confirm the results obtained for second heating, all compounds save Mono-10 were rerun after four months. The data is available in Appendix B but does not change the analysis presented so far. The absence of Mono-10 due to the sample being misplaced means that this new data cannot be used as a total analysis of the series. Also, despite the four month idle time Mono-2 failed to recrystallize so no T_m could be observed. Thus even the compounds tested had different thermal histories. However, for the most part features observed in the new run such as clearing temperatures and their associated enthalpies were consistent with previous runs.

3.3.3. X-Ray Diffraction

The POM and DSC data strongly implies the presence of at least one liquid crystal phase for all compounds studied. XRD provides an opportunity to quantitatively confirm the structure of these mesophases. However, the information obtained from XRD before and after such transitions was not significantly different from one another. All samples were identified as columnar hexagonal with unit cell dimensions between 21.2 Å and 23.3 Å, as summarized in Table 3-3.

Table 3-3: XRD results for the monomer series.

Compound	Temperature (°C)	d-spacing (Å)	Assignment (hkl)	Phase
Mono-2	131	18.4	(100)	Col_h
		3.5	*alkyl halo*	(a = 21.2 Å)
		3.4	*π-π*	
Mono-3	170	18.8	(100)	Col_h
		4.8	*alkyl halo*	(a = 21.7 Å)
		3.5	*π-π*	
Mono-8	161	19.5	(100)	Col_h
		11.5	(110)	(a = 22.5 Å)
		4.5	*alkyl halo*	
		3.5	*π-π*	
Mono-10	133	20.2	(100)	Col_h
		11.9	(110)	(a = 23.3 Å)
		4.6	*alkyl halo*	
		3.5	*π-π*	

The XRD data assigning a columnar hexagonal phase clearly corroborates the POM results indicating that the mesophase possessed six-fold symmetry. For all members of the series, only a minute difference (~0.1Å) in cell parameter is observed with heating and cooling.

With this knowledge, the lack of variation in the XRD data strongly reinforces the aforementioned re-analysis of the DSC data and new assignment of only a single Col_h phase. Some LC to LC transitions not associated with a change in unit cell are known[105], such as between ordered and disordered columnar phases[106] (Figure 1.6). However, it is

far more plausible that only one columnar phase exists; a transition to a more ordered column would also be accompanied by a sharpening of both the alkyl halo and π-π peaks in the diffractogram[107,108,109].

A qualitative analysis of the secondary peak is of interest here. Often (110) peaks are not seen in the X-ray data for hexagonally packed columnar mesophases since the relative lack of ordering has a deleterious effect on the amount of scattering during exposure to the X-ray beam. In this case the larger chain molecules (C_8 and C_{10}) exhibited a clear (110) peak while the shorter chains did not (Figure 3.6). This may indicate that the hexagonal structures produced by the longer chain monomers are more ordered.

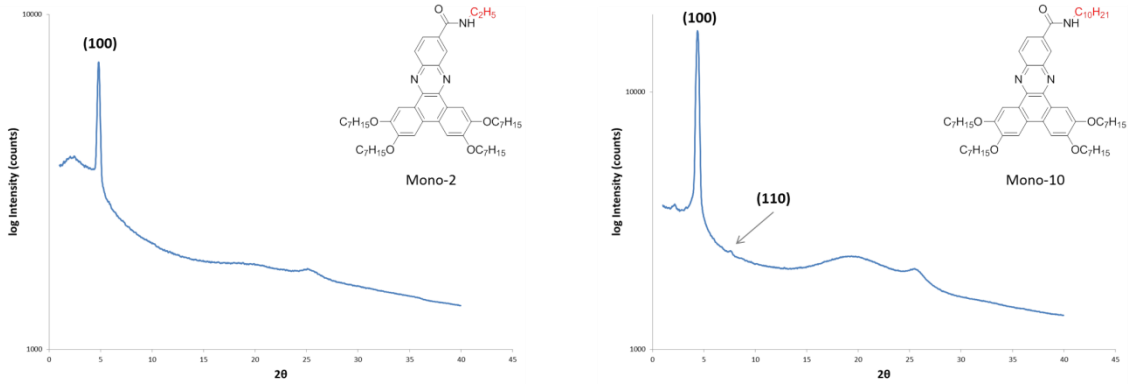

Figure 3.6: XRD diffractograms for Mono-2 (left, 131° C) and Mono-10 (right, 133° C), showing the (110) peak in the longer chain molecule.

Also of interest is the persistence of peaks at extremely low angles. Typically the hexagonal (100) peak is the sharpest and most intense, and this holds for this series of molecules. However, in all cases there is an additional peak as seen above. In the case of Mono-2 and Mono-3 the peak is broad. For the remaining monomers the peak is smaller but sharper. Since low angle peaks correspond to large structural features, this peak could represent the presence of larger geometries such as lamellae. .

3.3.4. Conclusion

The spontaneous tendency for these molecules to homeotropically align with the underlying glass substrate is a useful result that may lead us to a better understanding of how structural factors affect these types of arrangements, which are themselves

important for several semiconducting applications such as planar alignment for field effect transistors compared to homeotropic alignment for photovoltaics and light emitting devices(1.4.2). On the other hand, the actual liquid crystal phases themselves were uniformly columnar hexagonal with unit cell parameters on the order of 23 Å. Therefore the studied molecules form mesophases consistent with the majority of disc-shaped mesogens.

Finally, the molecules studied give us a baseline from which to assess future flexible and rigid dimers synthesized through the formation of amides from our preferred platform of carboxylic acid functionalized dibenzophenazine cores. Of the few dimers consisting of disc-shaped molecules reported, many tend to exhibit unconventional liquid crystal phases, but they tend to be dominated by triphenylene systems and are often unaccompanied by monomer comparison studies. In this light, should amide dimers also display phasic behaviour, the lack of similar behaviour for the monomer series would indicate dimer formation is a significant factor when inducing unusual phase behaviour in liquid crystal systems.

3.4. Synthesis

1,2-bis(heptyloxy)benzene (Alkoxy-7):

As described in Section 2.4, catechol (10.2291 g, 92.90 mmol) was reacted with heptylbromide (31.4 mL, 35.796 g, 199.9 mmol, 2.2 eq), K_2CO_3 (55.2782 g, 400.0 mmol, 4.3 eq) and NBu_4Br (2.6422 g, 8.1962 mmol, 0.1 eq), producing the final clear oil after FCC purification (19.9775 g, 65.18 mmol, 69% yield). ^{1}H NMR (600 MHz, $CDCl_3$) δ 6.91 (s, 4H), 4.01 (s, 4H), 1.88 – 1.80 (m, 4H), 1.50 (dt, J = 15.1, 7.3 Hz, 4H), 1.39 (ddd, J = 9.7, 6.8, 5.0 Hz, 4H), 1.36 – 1.30 (m, 8H), 0.92 (s, 6H).

3,3',4,4'-tetraheptyloxybenzil (Benzil-7):

As described in Section 2.4, Alkoxy-7 (19.9775 g, 65.18 mmol) along with $AlCl_3$ (5.2169 g, 39.12 mmol, 0.6 eq) and oxalyl chloride (2M, 17.92 mL, 4.551 g, 35.84 mmol, 0.5 eq) were reacted together to afford the final fluffy white solid (30.2590 g, 45.37 mmol, 70% yield). ^{1}H NMR (400 MHz, $CDCl_3$) δ 8.76 (s, 2H), 8.62 (s, 2H), 7.65 (s, 2H),

4.32 (td, J = 6.5, 3.6 Hz, 8H), 2.06 – 1.96 (m, 8H), 1.63 (dd, J = 13.6, 6.3 Hz, 8H), 1.52 – 1.39 (m, 16H), 1.37 – 1.24 (m, 8H), 0.98 (td, J = 7.0, 2.4 Hz, 12H).

2,3,6,7-tetraheptyloxyphenanthrene-9,10-dione (Quinone-7):

As described in Section 2.4, the Benzil-7 (1.938 g, 2.690 mmol) was reacted in the presence of BF_3•Et_2O (0.85 mL, 0.9809 mmol, 2.6 eq) and VOF_3 (1.6521 g, 13.3269 mmol, 5 eq) to form the final purple-red crystalline needle (1.43 g, 2.151 mmol, 80% yield). ^{1}H NMR (400 MHz, $CDCl_3$) δ 7.55 (s, 2H), 7.11 (s, 2H), 4.13 (dt, J = 45.8, 6.6 Hz, 8H), 1.97 – 1.78 (m, 8H), 1.60 – 1.43 (m, 8H), 1.44 – 1.26 (m, 24H), 0.90 (td, J = 6.8, 1.8 Hz, 12H).

2,3,6,7-Tetrakis(heptyloxy)dibenzo[a,c]phenazine-11-carboxylic acid (Acid-7):

Quinone-7 (0.980 g, 1.611 mmol) and 3,4-diaminobenzoic acid (0.320 g, 2.1032 mmol, 1.4 eq) were suspended in 75 mL of anhydrous EtOH along with a catalytic amount of glacial acetic acid (30 drops). This dark red mixture was stirred under reflux overnight. After cooling the resultant yellow suspension was poured over ice and the precipitate was collected using vacuum filtration. The yellow crystals were washed with cold EtOH, then recrystallized from hot AcOH to yield the final yellow crystalline needles (1.153 g, 1.4759 mmol, 99% yield). ^{1}H NMR (400 MHz, $CDCl_3$) δ 9.10 (s, 1H), 8.78 (s, 2H), 8.38 (d, J = 10.0 Hz, 2H), 7.71 (s, 2H), 5.30 (s, 1H), 4.33 (m, 8H), 1.99 (d, J = 6.8 Hz, 8H), 1.47 (s, 16H), 1.37 (s, 16H), 0.92 (s, 12H).

2,3,6,7-tetrakis(heptyloxy)-N-ethyldibenzo[a,c]phenazine-11-carboxamide (Mono-2):

Acid-7 (0.0621 g, 0.0795 mmol) was suspended in dry CH_2Cl_2 (20 ml) under a N_2 atmosphere in an ice-water bath. Oxalyl chloride (2M solution in CH_2Cl_2, 0.08 mL, 0.0203 g, 0.1600 mmol, 2 eq) was added dropwise by syringe. The reaction was stirred at room temperature for 2 hours. The resulting clear red solution was concentrated under reduced pressure to drive off excess oxalyl chloride, dissolved in dry ice-chilled CH_2Cl_2 (10 ml), and added dropwise to a mixture of ethylamine hydrochloride dissolved in aqueous NaOH (5M, 50 ml). After 24 hours of stirring the mixture at room

temperature, the mixture was extracted with $CHCl_3$ (50 ml) added to the remaining CH_2Cl_2 and washed with water (50 ml) once, then 10% HCl (50 ml), twice more with water (50 ml), and finally with brine (50 ml). The yellow-orange solution was dried over $MgSO_4$, gravity filtered, and concentrated under reduced pressure. Flash column chromatography was performed with an eluent system of 100% DCM, then recrystallized from hot MeOH to provide an orange-yellow solid. (0.0122 g, 0.015 mmol, 19% yield) ^{1}H NMR (500 MHz, $CDCl_3$) δ 8.77 (d, J = 4.2 Hz, 2H), 8.62 (s, 1H), 8.36 (d, J = 8.8 Hz, 1H), 8.23 (dd, J = 8.8, 1.9 Hz, 1H), 7.72 (s, 2H), 6.41 (s, 1H), 4.31 (dt, J = 22.5, 5.8 Hz, 8H), 3.67 – 3.57 (m, 2H), 1.97 (d, J = 7.9 Hz, 8H), 1.58 (s, 8H), 1.45 (s, 8H), 1.36 (dd, J = 9.4, 4.8 Hz, 19H), 0.92 (t, J = 6.1 Hz, 12H); ^{13}C NMR (151 MHz, $CDCl_3$) δ 167.07, 152.36, 152.22, 149.66, 143.09, 142.86, 142.78, 140.77, 135.01, 129.83, 127.61, 127.42, 127.10, 126.91, 123.67, 123.64, 109.04, 108.86, 106.58, 106.52, 69.79, 69.31, 35.38, 32.03, 32.01, 29.53, 29.48, 29.46, 29.32, 26.30, 26.29, 26.27, 22.81, 22.79, 15.14, 14.29, 14.27; MS-ESI for [$C_{51}H_{73}N_3O_5$] calculated (found): 807.555 (807.5564); HR-MS for [$C_{51}H_{73}N_3O_5$-H^+] calculated (found): 808.5623 (808.5636).

2,3,6,7-tetrakis(heptyloxy)-N-propyldibenzo[a,c]phenazine-11-carboxamide (Mono-3):

Acid-7 (0.0494 g, 0.0633 mmol) and DMAP (0.0353 g, 0.3152 mmol, 5 eq) were dissolved in dry CH_2Cl_2 (20 ml) under a N_2 atmosphere in an ice-water bath. The solid propylamine hydrochloride salt (0.0990 g, 0.1036 mmol, 1.6 eq) was included in the same addition. The mixture was stirred for 10 minutes while purging with N_2. EDCI (0.0252 g, 0.1315 mmol, 2.1 eq) was added under positive N_2 pressure. The mixture was left to slowly heat to room temperature under stirring for 24 hours under slow N_2 flow. The mixture was extracted with $CHCl_3$ (50 ml) added to the remaining CH_2Cl_2 and washed with water (50 ml) once, then 10% HCl (50 ml), twice more with water (50 ml), and finally with brine (50 ml). The yellow-orange solution was dried over $MgSO_4$, gravity filtered, and concentrated under reduced pressure. Flash column chromatography was performed with an eluent system of 10% OEtAc:hexanes followed by a gradient to 30% OEtAc:hexanes. The separated fractions were then recrystallized from hot MeOH to provide an orange-yellow solid (0.0405 g, 0.0493 mmol, 78% yield). ^{1}H NMR (500 MHz,

$CDCl_3$) δ 8.71 (d, J = 4.4 Hz, 2H), 8.58 (d, J = 1.8 Hz, 1H), 8.33 (d, J = 8.8 Hz, 1H), 8.22 (dd, J = 8.8, 2.0 Hz, 1H), 7.67 (d, J = 4.8 Hz, 2H), 6.51 (t, J = 5.7 Hz, 1H), 4.40 – 4.22 (m, 8H), 3.55 (dd, J = 13.7, 6.4 Hz, 2H), 2.03 – 1.93 (m, 8H), 1.59 (d, J = 1.4 Hz, 10H), 1.45 (s, 8H), 1.37 (dd, J = 6.9, 3.4 Hz, 16H), 1.08 (t, J = 7.4 Hz, 3H), 0.95 – 0.89 (m, 12H); ^{13}C NMR (151 MHz, $CDCl_3$) δ 167.26, 152.31, 152.16, 149.61, 149.59, 143.01, 142.78, 142.73, 140.71, 135.08, 129.80, 127.55, 127.42, 127.05, 126.85, 123.63, 123.57, 108.98, 108.82, 106.47, 69.75, 69.29, 42.23, 32.04, 32.02, 29.54, 29.53, 29.50, 29.47, 29.34, 26.31, 26.30, 26.27, 23.18, 22.81, 22.79, 14.28, 14.27, 11.71; MS-ESI for [$C_{52}H_{75}N_3O_5$] calculated (found): 821.571 (821.568); HR-MS for [$C_{52}H_{75}N_3O_5$-H^+] calculated (found): 822.5780 (822.5753).

2,3,6,7-tetrakis(heptyloxy)-N-octyldibenzo[a,c]phenazine-11-carboxamide (Mono-8):

Synthesis was performed as described for the final Mono-3 compound, except where octylamine (0.02 mL, 0.01562 g, 0.1209 mmol, 1.2 eq) was added via syringe to the orange solution of Acid-7 (0.0787 g, 0.1008 mmol) and DMAP (0.0408 g, 0.3643 mmol, 3.6 eq). EDCI (0.0399 g, 0.2081 mmol, 2.1 eq) was added after the first three reagents were stirred in an ice bath for 20 minutes. FCC purification (20% OEtAc:hexanes) yielded the final yellow solid (0.0129 g, 0.014 mmol, 14% yield). ^1H NMR (500 MHz, $CDCl_3$) δ 8.79 (d, J = 6.5 Hz, 2H), 8.62 (s, 1H), 8.36 (d, J = 8.8 Hz, 1H), 8.24 (d, J = 9.0 Hz, 1H), 7.73 (s, 2H), 6.41 (s, 1H), 4.32 (dt, J = 29.3, 6.4 Hz, 8H), 3.57 (d, J = 6.6 Hz, 2H), 1.97 (d, J = 6.9 Hz, 8H), 1.74 – 1.68 (m, 2H), 1.59 (s, 6H), 1.45 (s, 10H), 1.36 (s, 16H), 1.25 (s, 10H), 0.92 (s, 15H); ^{13}C NMR (151 MHz, $CDCl_3$) δ 167.14, 152.35, 152.22, 149.65, 143.07, 142.84, 142.77, 140.75, 135.10, 129.83, 127.53, 127.47, 127.11, 126.91, 123.67, 123.63, 109.04, 108.87, 106.55, 106.52, 69.78, 69.32, 40.58, 32.03, 32.02, 31.98, 29.93, 29.53, 29.49, 29.46, 29.40, 29.33, 27.24, 26.30, 26.27, 22.81, 22.79, 14.29, 14.27; MS-ESI for [$C_{57}H_{85}N_3O_5$-H^+] calculated (found): 892.656 (892.656); HR-MS for [$C_{57}H_{85}N_3O_5$-H^+] calculated (found): 892.6562 (892.6579).

2,3,6,7-tetrakis(heptyloxy)-N-decyldibenzo[a,c]phenazine-11-carboxamide (Mono-10):

Using a method identical to Mono-8, Acid-7 (0.0856 g, 0.1008 mmol) was reacted with decylamine (0.08 mL, 0.06296 g, 0.4586 mmol, 4.2 eq) in the presence of DMAP (0.0636 g, 0.5679 mmol, 5.2 eq) and EDCI (0.0463 g, 0.2415, 2.2 eq) to form an orange solution. The final product was a yellow solid (0.0217 g, 0.024 mmol, 22% yield). ^{1}H NMR (500 MHz, $CDCl_3$) δ 8.71 (d, J = 4.3 Hz, 2H), 8.56 (d, J = 1.8 Hz, 1H), 8.32 (d, J = 8.8 Hz, 1H), 8.21 (dd, J = 8.8, 1.9 Hz, 1H), 7.66 (d, J = 6.8 Hz, 2H), 6.48 (t, J = 5.6 Hz, 1H), 4.36 – 4.23 (m, 8H), 3.57 (d, J = 6.2 Hz, 2H), 2.02 – 1.93 (m, 8H), 1.60 (dd, J = 5.3, 2.5 Hz, 8H), 1.45 (d, J = 5.7 Hz, 10H), 1.40 – 1.34 (m, 20H), 1.32 – 1.27 (m, 10H), 0.95 – 0.90 (m, 15H); ^{13}C NMR (151 MHz, $CDCl_3$) δ 167.13, 152.35, 152.22, 149.65, 143.07, 142.84, 142.77, 140.75, 135.10, 129.82, 127.54, 127.47, 127.10, 126.91, 123.67, 123.62, 109.04, 108.87, 106.55, 106.52, 69.77, 69.32, 40.58, 32.05, 32.03, 32.02, 29.93, 29.85, 29.74, 29.54, 29.49, 29.47, 29.33, 27.25, 26.30, 26.29, 26.27, 22.84, 22.81, 22.79, 14.29, 14.27; MS-ESI for [$C_{59}H_{89}N_3O_5$] calculated (found): 919.680 (919.679); HR-MS for [$C_{59}H_{89}N_3O_5$-H^+] calculated (found): 920.6875 (920.6875).

4. Procedure

4.1. Experimental apparatus

4.1.1. Nuclear Magnetic Resonance

NMR spectra were obtained using several instruments in the SFU Bruker Spectroscopy Lab: ^{1}H spectra were obtained on a Bruker AVANCE III running at 500 MHz, or a Bruker AVANCE III running at 400 MHz. ^{13}C spectra were run using a Bruker AVANCE II at 150Mhz with either a TCI600 or a QNP600 cryoprobe. Chemical shifts are expressed in ppm and were calculated from a reference solvent such as $CDCl_3$ (7.26 ppm). Peak analysis is coded as follows: s = singlet, d = doublet, t = triplet, dd = doublet of doublet, q=quartet, quint = quintuplet, m = multiplet.

4.1.2. Mass Spectrometry

Mass spectrometry of small molecules (M_w < 500 g/mol) was performed using either a Varian 4000 GC/MS/MS equipped with a direct probe and ionization energy of 70 eV or a Hewlett-Packard 5985 mass spectrometer with EI of 70 eV operated by SFU technician Hongwen Chen.

Mass spectrometry of larger molecules including all dimer molecules (M_w ≥ 500 g/mol) was initially performed by MALDI-TOF using a PE Applied Biosystems Perspective Voyager-DE STR employing a nitrogen laser (337 nm) to desorb analytes from the 2,5-dihydroxybenzoic acid matrix.

Following decommissioning of this machine, all MALDI-TOF reported herein was performed by a PE Applied Biosystems Perspective Voyager-DE STR employing a nitrogen laser (337 nm) – however, further optimization and calibration allowed for the elimination of the matrix.

High Resolution Mass Spectrometry was performed by Hongwen Chen at SFU on the instruments mentioned above, unless noted. Additional high-resolution mass spectrometry (dimer series only) was performed by Nonka Sevova at the Notre Dame University Mass Spectrometry and Proteomics Facility on a Bruker microTOF-II utilizing ESI+ ionization. Analytical reports from the Notre Dame facility are available in Appendix D.

4.1.3. Elemental Analysis

Elemental analysis was carried out courtesy of Mr. Frank Haftbaradaran at Simon Fraser University with an EA1110 CHN CE Instrument and WO_3 accelerant. EA of the dimer compounds was unsuccessful, so in lieu of elemental analysis HR-MS is reported.

4.1.4. Differential Scanning Calorimetry

DSC (differential scanning calorimetry) was used to determine transition temperatures. Initial analyses were performed on a Perkin Elmer DSC 7 and the values for the temperatures and enthalpies of transition were recorded on the first heating/cooling cycle at a rate of 10º C/min, then a second cycle was performed to confirm reproducibility. All values reported in this thesis were obtained using a TA Instruments Q2000 with RCS90 cooling system and T-Zero precision machined hermetically sealed aluminum sample pans.

4.1.5. Polarized Optical Microscopy

Photomicrographs were taken through crossed polarizers on an Olympus BX50 polarized optical microscope equipped with a Linkam LTS350 heating stage. Samples were prepared by placing the sample on a glass microscope slide cleaned with ethanol, then heating to the isotropic liquid phase at a rate of 20º C/min. The melt was then drawn under a cleaned glass cover slip by capillary action. In some cases cover the slip was removed and the layer was remounted under a newly cleaned slip. Several heating and cooling cycles at different cooling rates were used to make observations.

4.1.6. Variable Temperature X-Ray Diffraction

Samples were heated to the isotropic liquid phase on a hot plate and loaded by capillary action. At least four samples were prepared in case of loss. Excess material was cleaned off the sides with clean, dry tweezers. Capillaries were then cut to length and mounted in a capillary furnace.

Measurements were carried out on a Rigaku RAXIS RAPID diffractometer using Cu Kα radiation (λ = 1.5418Å), a graphite monochromator and a Fujifilm Co. Ltd curved image plate (460 mm x 256 mm). Temperature was controlled with an Omega temperature controller connected to the capillary furnace with a K-type thermocouple for feedback[48]. Owing to technical issues, the controller was set to manual mode. Due to thermal equilibration, the temperature often dropped during the course of acquisition. Only the final temperature is reported.

A 0.3 mm collimator was used and all samples were irradiated for 30 minutes except where noted.

Peaks and their respective angle measurements and d-spacings were determined using the MDL JADE software. Peak type was analyzed by taking the reciprocal d-spacings and dividing them by the highest intensity peak, unless otherwise noted. Likewise, only peaks with greater than 1% intensity in the low angle region were analyzed unless otherwise noted.

4.2. Materials

Chemicals were used as received (Aldrich, Anachemia and Fisher Scientific) unless otherwise noted. Distilled dichloromethane was dried by distillation over $CaCl_2$; some procedures used inhibitor-free CH_2Cl_2 dried in a Pure-Solv Solvent Purification System over alumina at elevated temperature and reduced pressure.

Other solvents were used without further purifications. Nitrogen gas was purchased from Praxair. Silica (230-400 mesh) was sourced from Silicycle Inc. Deuterated solvents ($CDCl_3$, acetone-d6, and DMSO-d6) from Cambridge Isotope Labs were purchased from Aldrich.

The following solvents and reagents are listed by their manufacturer.

Aldrich : $C_2H_3NH_2$•HCl, $C_3H_7NH_2$•HCl, $C_6H_{13}NH_2$, $C_8H_{17}NH_2$, $C_6H_{13}Br$, $C_7H_{15}Br$, $C_8H_{17}Br$, $C_{10}H_{21}Br$, BF_3•Et_2O, VOF_3, $SnCl_2$, H_2O_2, BBr_3, NBu_4Br, butanone, H_2SO_4, HNO_3, catechol, $FeCl_3$, I_2, HBr.

Alfa-Aesar: VOF_3

Caledon: citric acid, K_2CO_3, Na_2SO_3, NaCl, $MgSO_4$, $NaHCO_3$, NaOAc, $Na_2S_2O_3$, methanol, anhydrous ethanol, acetic acid, HCl.

Eastman Kodak: *o*-phenylenediamine.

Fluka: DMAP

Strem Chemicals: $FeCl_3$.

VWR: DMF, THF, DCM, hexanes, ethyl acetate, DMSO, pyridine.

5. Conclusion and Future Work

As organic materials become more prominent, it will be advantageous to have a comprehensive understanding of the factors governing self-assembly in liquid crystals. This is especially true for discotic mesogens in particular since their raw charge transfer ability provides advantages above even many conducting polymers. In addition, the one-dimensional nature of such charge transport is extremely advantageous for most organic semiconducting applications such as photovoltaics and OLEDs.

The ability to design mesogens beyond the usual modifications in alkyl chain length would enable the production of custom geometries, each optimized for a certain application. The results of the studies contained herein show that rigid dimers consisting of discrete disc-shaped mesogenic units connected via a rigid covalent bond can be used to elongate the overall shape of the molecule and induce unusual liquid crystalline phase behaviour namely, the formation of mesophases that are usually more associated with rod-shaped molecules such as the nematic phase.

The project also shows that these types of dimers formed from disc-like units spontaneously align in a homeotropic way between a glass substrate and cover slip without surface modification. This is important for the formation of large oriented monodomains without the usual thermomechanical treatment such as annealing.

In terms of rigidly linked dimers, there are a number of possible avenues for future exploration. In order to achieve a longer bridge than the single C-C sigma bond studied in this report, an unsaturated connector is necessary. Potential bridging groups include triazoles that are accessible by azide click chemistry. If maintenance of the current condensation approach is desired, simple cyclic molecules or fused benzene rings with alcoholic substituents would attain the same results (Figure 5.1).

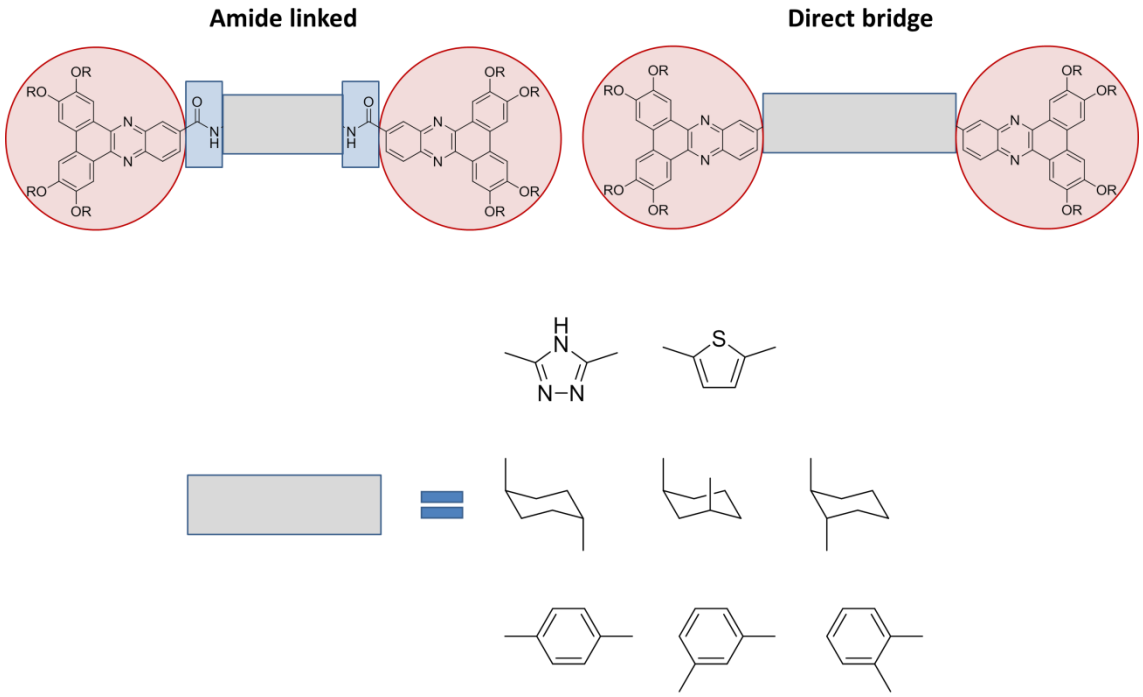

Figure 5.1: Some possible linking moieties for future rigid dimers.

Many avenues for further investigation exist on a device-oriented level. An interesting experiment would be the systematic spin coating of various thicknesses of the dimer. This would allow us to determine if homeotropic alignment in these molecules is valid in the bulk material as opposed to a thin film[110], each of which has its own corresponding applications.

A series of amide-functionalized DBP monomers was also synthesized with a series of short and long alkyl chains. These molecules represent a baseline set of phase behaviour against which future dimer molecules (Figure 3.1) can be compared. Only the normal columnar hexagonal phase was observed for these molecules but in a fascinating turn of events they were also shown to exhibit a spontaneous tendency to homeotropically align with the underlying substrate.

With the monomer series in hand and further populated by other workers in the Williams lab, it is natural to continue the work by synthesizing DBP dimers linked by amide-bridged alkyl chains. These compounds could then be compared to more rigid dimers utilizing saturated or unsaturated cyclic linkers such as benzene. Even more

studies await if the already mentioned possibilities were used to produce asymmetrical dimers.

By coincidence we observed that homeotropic alignment was repressed by the presence of greasy contaminants attributed to the plasticizer compounds found in common organic solvents. This observation highlights the requirement for extremely pure compounds in order to observe homeotropic alignment but it also illustrates how mixtures or guest molecules could be used to promote or repress that alignment as well as create future mesostructures[111]. These are potential areas for future investigation.

Furthermore, POM images of impure samples of the series suggest intriguing tendencies. DBPD-6 appeared to form an optically isotropic monodomain, and the remaining compounds did not display any homeotropic alignment. Compared to textures observed for repurified compounds, the sudden ability to align suggests that although monodomain formation was not hindered for DBPD-6, it was for the overall series. Considering that many applications utilize long alkyl chain alcohols or silanes to achieve monodomain formation for samples that display a tendency to align, the seemingly opposite effect seen in these dimers is interesting.

Appendices

Appendix A: Fitting of XRD patterns

General Fitting Methodology

The Bragg scattering condition is described in Equation A-1.

Equation A-1

$$n\lambda = 2d\sin\theta$$

When an X-ray diffraction pattern is indexed, the goal is to relate the observed scattering angles θ to the interplanar spacing 'd' which will give us a quantitative measure of the periodicity present in the material. However, scattering of most materials is dependent on the direction of travel within the bulk. It is thus important that we have an understanding of which diffracted lines correspond with a given direction vector.

The standard method of describing periodic arrangement in a material is the Miller Index. the fundamental equation for the general indices h, k, and l and their corresponding interplanar angles α, β, and γ is given below.

Equation A-2

$$\frac{1}{d^2} = \frac{1}{\left(1 + 2cos\alpha cos\beta cos\gamma - cos^2\alpha - cos^2\beta - cos^2\gamma sin^2(\gamma)\right)} \times \left\{ \frac{h^2 sin^2\alpha}{a^2} + \frac{k^2 sin^2\beta}{b^2} + \frac{l^2 sin^2\gamma}{c^2} - \frac{2hk}{ab}(cos\alpha cos\beta - cos\gamma) + \frac{2kl}{bc}(cos\beta cos\gamma - cos\alpha) + \frac{2lh}{ac}(cos\gamma cos\alpha - cos\beta) \right\}$$

This equation simplifies easily for arrangements where the interplanar angles are orthogonal. For example, for a cubic system can be considered a special case where a=b=c and α=β=γ=90°:

Equation A-3

$$\frac{1}{d^2} = \frac{h^2 + k^2 + l^2}{a^2}$$

Hexagonal arrangements are commonly observed for disc-shaped mesogens, in the case where a=b≠c and α=β=90° γ=60°:

Equation A-4

$$\frac{1}{d^2} = \frac{(h^2 + k^2)}{a^2} + \frac{l^2}{c^2}$$

Since most discotic mesophases are one-dimensional liquids (or two-dimensional solids), in most cases we can ignore the third dimensional parameter *l* and treat the problem as being ordered in only two dimensions. Then, if we isolate the interplanar distance 'd' we see that the equation is dependent only on the Miller index (hk), since a is the unit cell constant.

Equation A-5

$$d = \sqrt{\frac{a^2}{(h^2 + k^2)}}$$

Since we expect the strongest diffraction power to be along certain Miller indices depending on the type of packing present, it is of interest to look at the ratios of these d-spacings.

Equation A-6

$$\frac{d_{100}}{d_{110}} = \frac{\sqrt{\frac{a^2}{(1^2 + 0^2)}}}{\sqrt{\frac{a^2}{(1^2 + 1^2)}}} = \sqrt{\frac{2}{1}}$$

We can see that a whole number is obtained inside the root. If the most intense peak is assumed to be (100), then characteristic whole number ratios are obtained for certain packing arrangements – in fact, many common arrangements have specific

combinations of these indices based on which are present and which are missing – also called systematic absences. Using these ratios and the systematic absences gives us a way to analyze diffraction patterns without resorting to solving systems of equations with large numbers of variables.

The Bragg condition tells us that the diffraction angles observed in a diffractogram are inversely proportional to the periodicity along a certain direction of travel through the material.

Equation A-7

$$d = \frac{n\lambda}{2sin\theta}$$

Similar to Equation A-1, the spacing is dependent only on θ since the remaining factors n and λ are constants. Taking the ratio of these angles gives us the reciprocal ratio of the d-spacing and the related Miller indices.

Equation A-8

$$\frac{d_{100}}{d_{110}} = \sqrt{\frac{\frac{n\lambda}{2sin\theta_{100}}}{\frac{n\lambda}{2sin\theta_{110}}}} = \sqrt{\frac{sin\theta_{110}}{sin\theta_{100}}} = \sqrt{\frac{2}{1}}$$

We expect the integer value obtained to increase with the observed diffraction angle – which leads to the practical method of analyzing a XRD pattern. Signals are arranged by increasing diffraction angle. Software used to determine the integration of the signals gives an indication of the intensity of each peak. By taking the ratios of each ascending angle (or d-spacing calculated from it) compared to the most intense peak at low angles gives all possible ratios from the data. These ratios can then be compared to the calculated values for increased Miller indices compared to that for 100 or 200.

Systemic absences for a number of commonly observed liquid crystal packings are in Table 2-3. For the most part such indexing is straightforward since the most

intense low-angle peaks is usually the (100). There is some difficulty when the (200) or (110) directions give the largest diffraction peak, but this is easily overcome.

Oblique Phases

In an oblique phase all indices are allowed and therefore we cannot take advantage of the Debye-Scherrer method, in which ratios of either θ or d-spacing are compared to systematic absences that arise from symmetry operations on various unit cells. Typically comparisons are made to the simplest possible unit cells such as the cubic series, then applied to progressively less symmetric arrangements if the fit is not satisfactory. This is because the angle γ can theoretically have any value between 90° (as seen in the orthorhombic packing types) and 0°. Note that the special case of a hexagonal packing occurs when γ=60°. Since this angle is variable, we must use the more general form of Equation A-3:

Equation A-9

$$\frac{1}{d^2} = \frac{1}{sin^2(\gamma)}\left(\frac{h^2}{a^2} + \frac{k^2}{b^2} - \frac{2hkcos(\gamma)}{ab}\right)$$

With some manipulation we can isolate for the interplanar spacing ‘d’ as in Equation A-10. As many fractional terms have been eliminated as possible for the sake of computational convenience.

Equation A-10

$$d = absin\gamma\left(h^2b^2 + k^2a^2 - 2abhkcos\gamma\right)^{-1/2}$$

Unfortunately the result is an equation of several variables (a, b, h, k and γ). In conventional XRD analysis we can remove three variables by assuming that certain low-valued Miller indices are the most intense – which is also borne out in practice. However, as mentioned in the XRD chapter, liquid crystals do not have the intrinsic amount of ordering necessary to provide a large number of intense peaks. Since all indices are possible, there is no guarantee that the most intense peak will correspond to (100) as in the Debye-Scherrer method. Finally, since oblique packing is not symmetric, negative indices are not equivalent and the last term of Equation A-10 has a sign-dependent contribution to the spacing.

The problem before us in the analysis of oblique X-ray diffractograms is the number of variables and the large number of possible (and unknown) Miller indices. Luckily, we can take advantage of the following factors:

- Higher Miller Indices normally do not contribute significantly in relatively disordered samples such as liquid crystals. Thus, there is a calculation-friendly and finite number of possible initial peaks.
- The sample is likely two-dimensional.
- The observed angle of diffraction rings increases with increasing absolute value of the corresponding Miller index.

Assuming that we can assign arbitrary values for hkl, there is still a problem: even making hkl values constant, the interplanar spacing is still an equation with three unknowns – a, b, and γ.

At this point, we require two experimentally determined values to provide two equations which will enable us to solve for the two unknowns, 'R' and 'γ'.

Taking a cue from the Debye-Scherrer method we can take the ratio of the most intense peaks which also happen to be the most consistent and reliable. The simplest assumption is that the most intense peak is (100), but since all indices are allowed this is not assured. Further, the next most intense peak is usually (110) or (210), but again that is not certain. In theory all possible combinations of the most intense peaks should be evaluated.

It was decided to pursue a brute force iterative method. First, the most intense peak was set at a small value such as (-100) or (100). Then, a/b and γ were calculated for the ratio of that peak with the next most intense peak, for all Miller indices up to (320). This was repeated for the 3rd peak observed.

The cell parameters generated from this calculation were re-inputted into a spreadsheet to calculate the resulting d-spacing for all possible values of the Miller index up to (320). The average absolute error between the calculated d-spacing and the observed d-spacing was also calculated.

This approach generated several hundred possible solutions. Non-viable solutions were culled from the set using the following criteria:

- Only solutions with the lowest average error between calculated and observed d-spacings.
- Only solutions with γ=90°±10° since POM results indicated nearly orthogonal between the observed dendrites. As expected, these answers also had the lowest average errors as determined by the previous criteria.
- In addition, the final solutions were determined to be the ones with the lowest standard deviation in absolute error.

Despite the large number of solutions per analysis, only 1-2 candidates were identified for each XRD. The excellent agreement between calculated and observed values, as well as the small set of possible solutions suggests that the method was valid. This is illustrated graphically in (Figure A-1), showing that for DBPD-6 only one solution out of the 26 closest (there were a total of 1008 possible solutions calculated) is consistent below an absolute error level of 0.1 Å ($d_{calculated} - d_{observed}$).

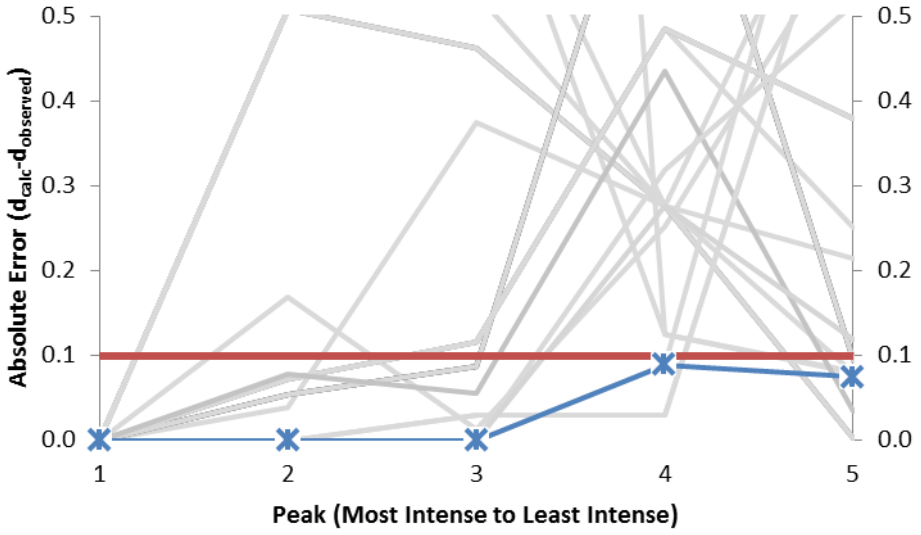

Figure A-1: Absolute error between calculated and observed d-spacings for DBPD-6 at 142° C. Peaks arranged from most intense (1) to least intense (5).

Appendix B: DSC Data

Amide Monomer Series – First Heating Data

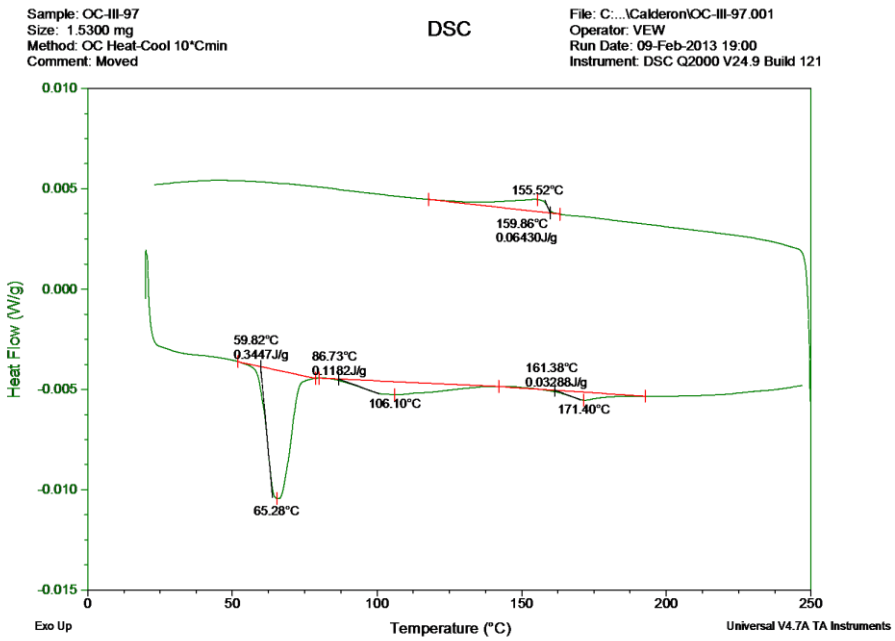

Figure B-1: First heating DSC trace for Mono-2.

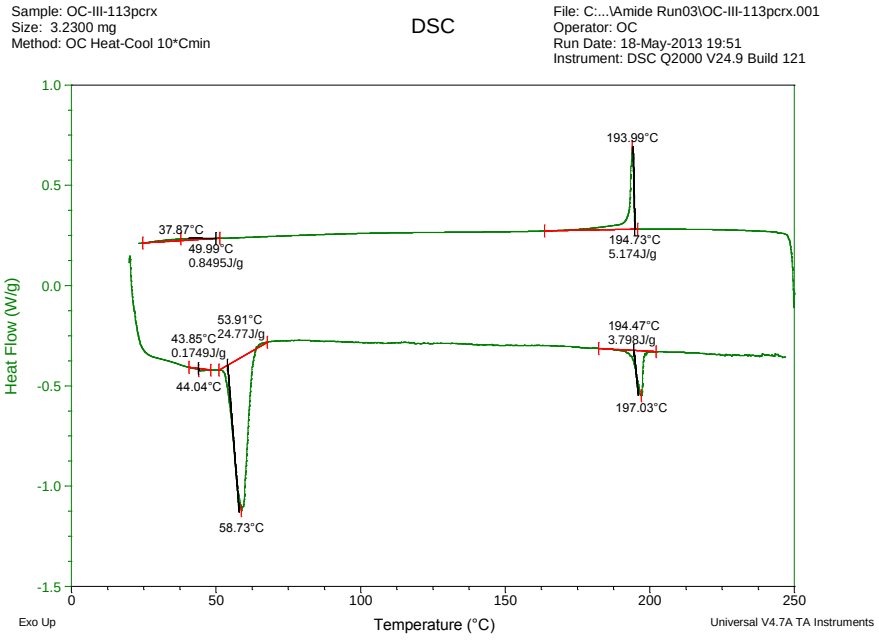

Figure B-2: First heating DSC trace for Mono-3.

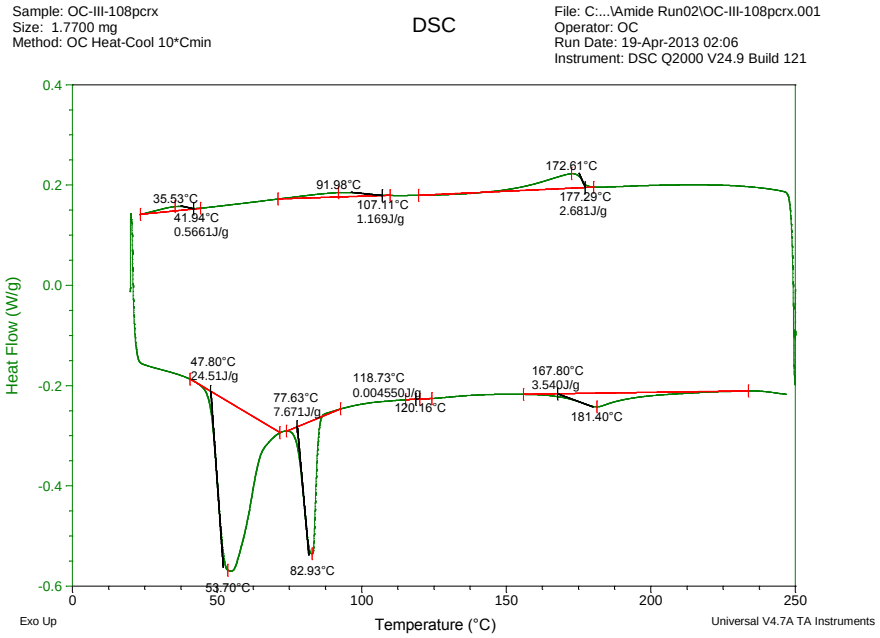

Figure B-3: First heating DSC trace for Mono-8.

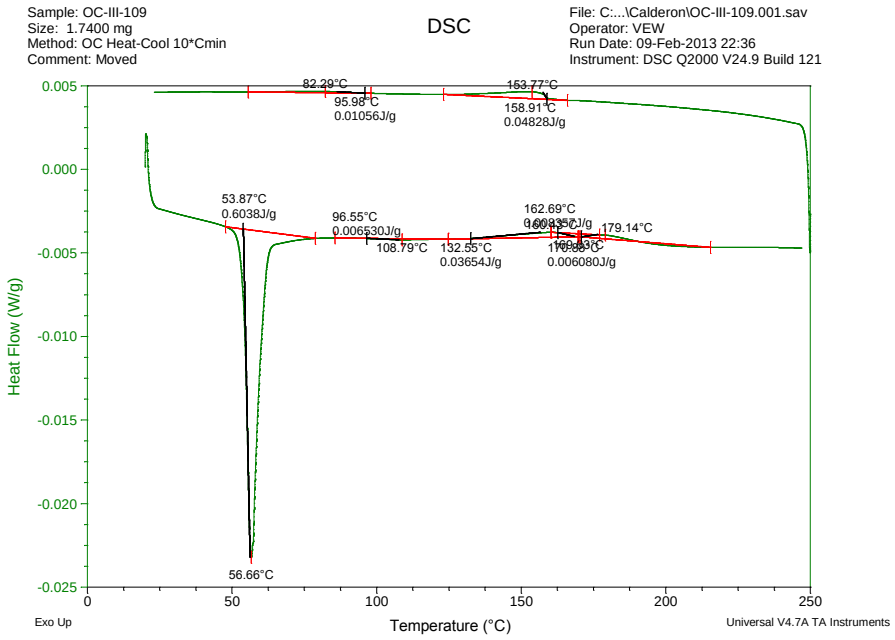

Figure B-4: First heating DSC trace for Mono-10.

Amide Monomer Series – Latest Data

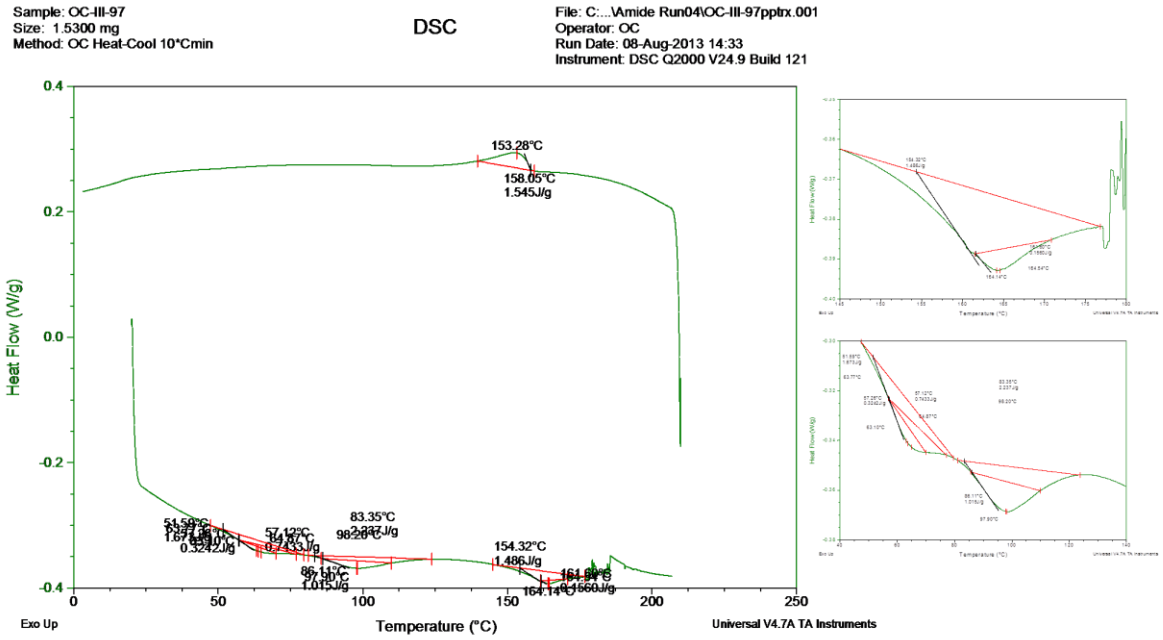

Figure B-5: Latest DSC trace for Mono-2.

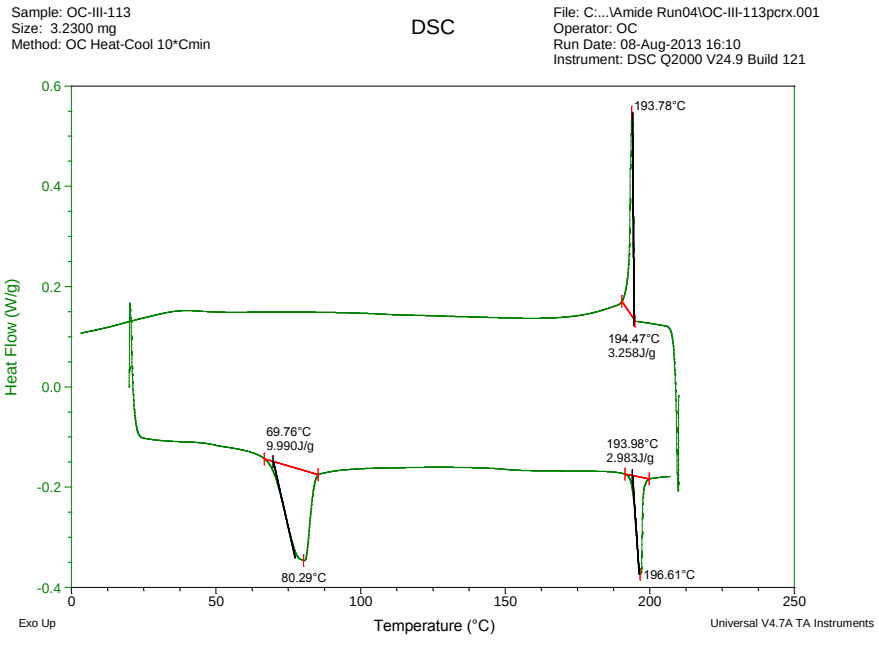

Figure B-6: Latest DSC trace for Mono-3.

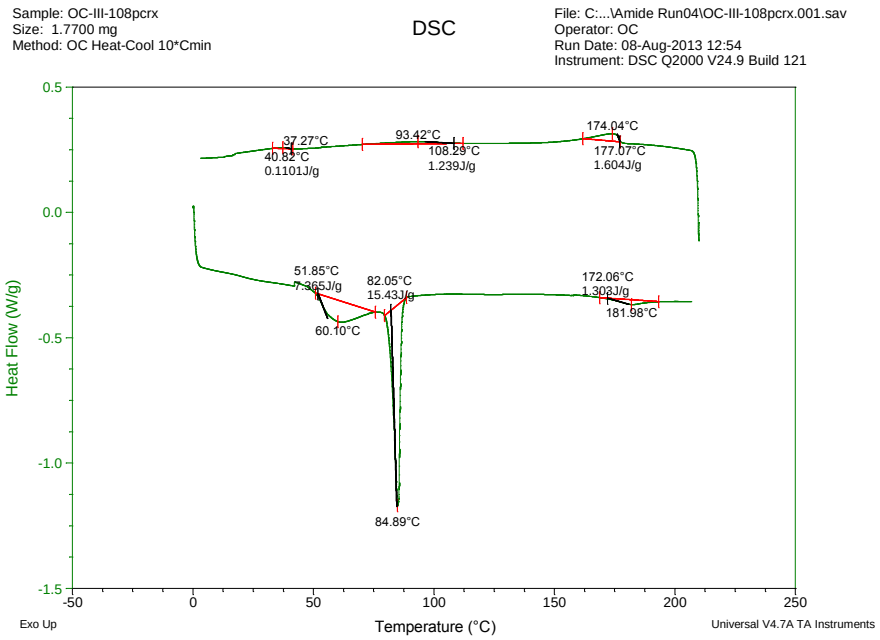

Figure B-7: Latest DSC trace for Mono-8.

Appendix C: XRD Data

DBP Dimer Series

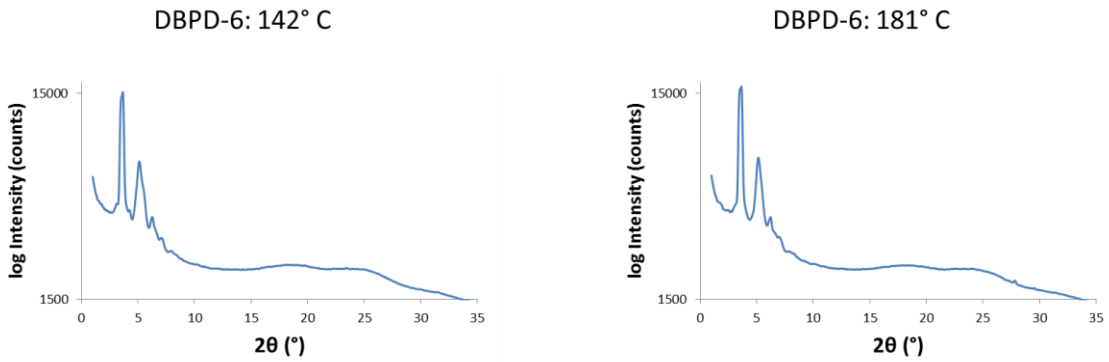

Figure C-1: DBPD-6 dimer XRD traces. Left: 142° C. Right: 181° C.

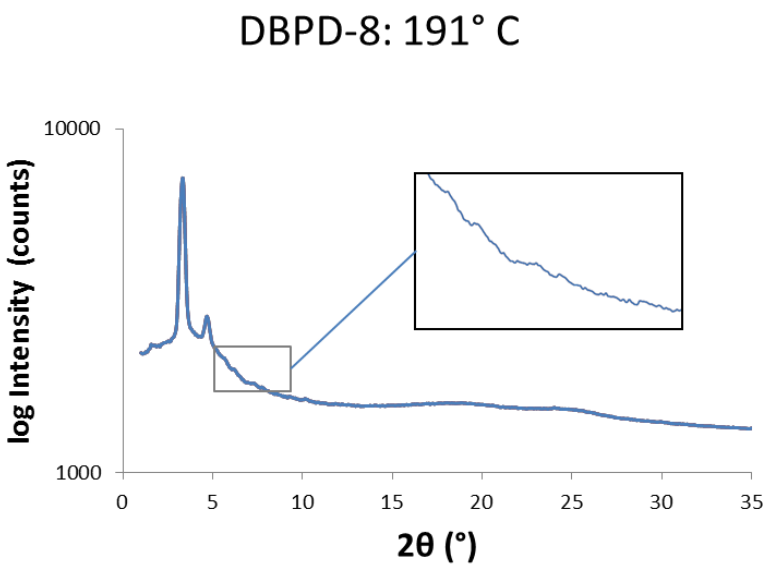

Figure C-2: DBPD-8 dimer XRD trace at 191°C.

Amide Monomer Series

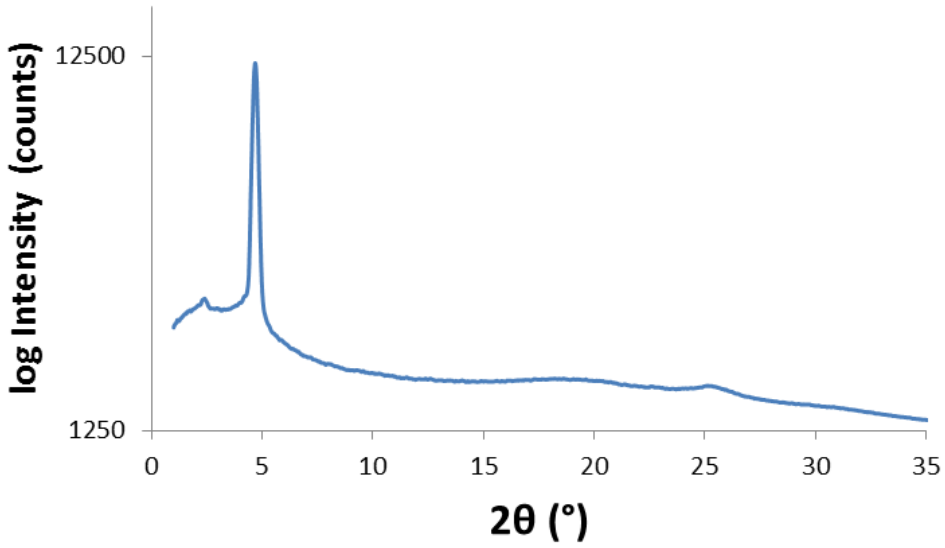

Figure C-3: Mono-3 XRD trace at 170° C.

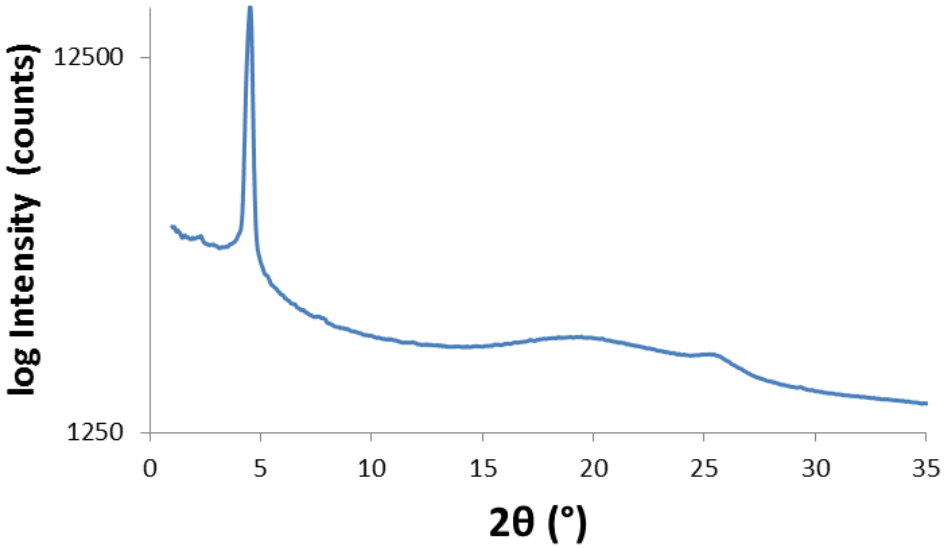

Figure C-4: Mono-8 XRD trace at 161° C.

Appendix D: External Reports for HR-MS Data

DBP Dimer Series

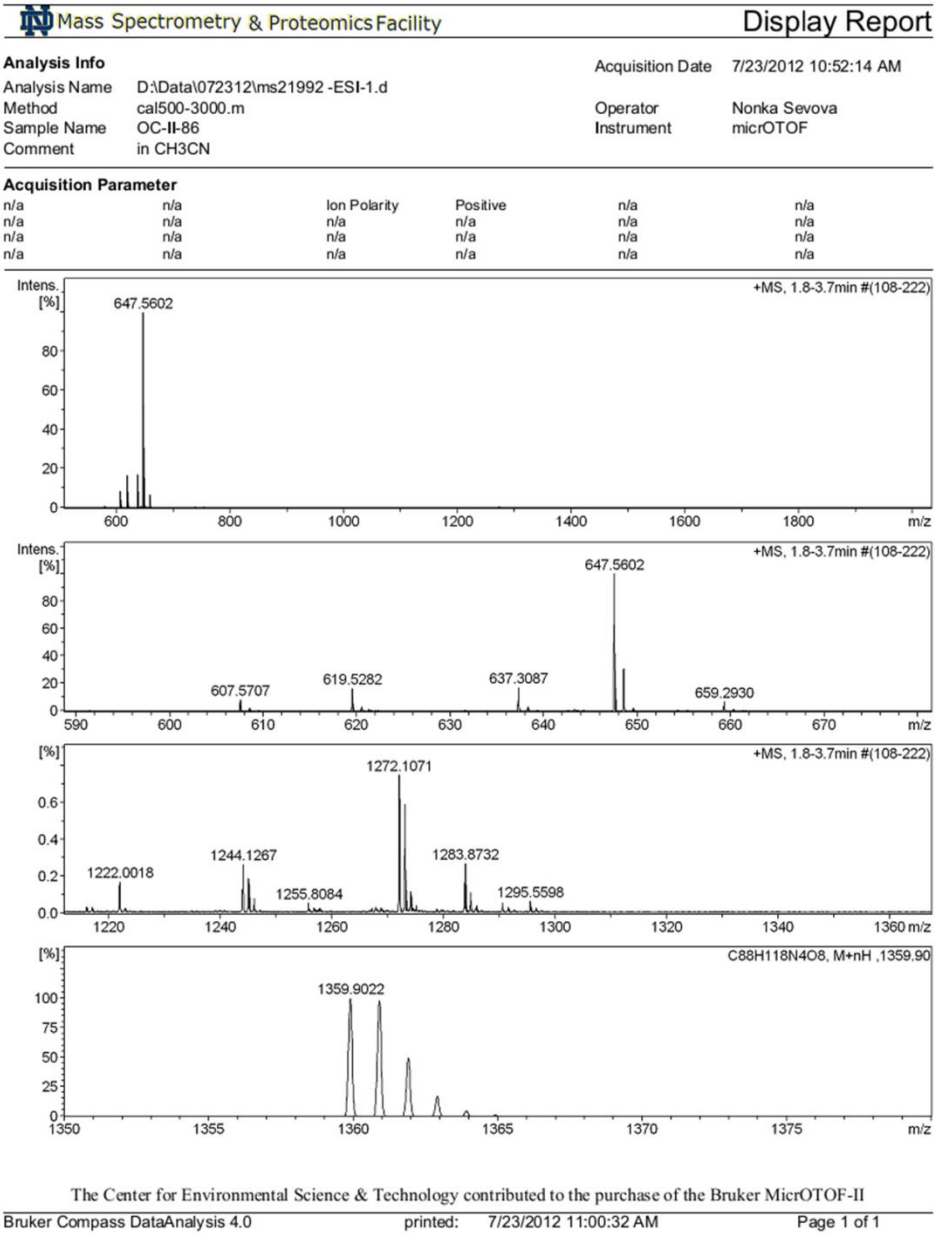

Figure D-1: HR-MS report for DBPD-6.

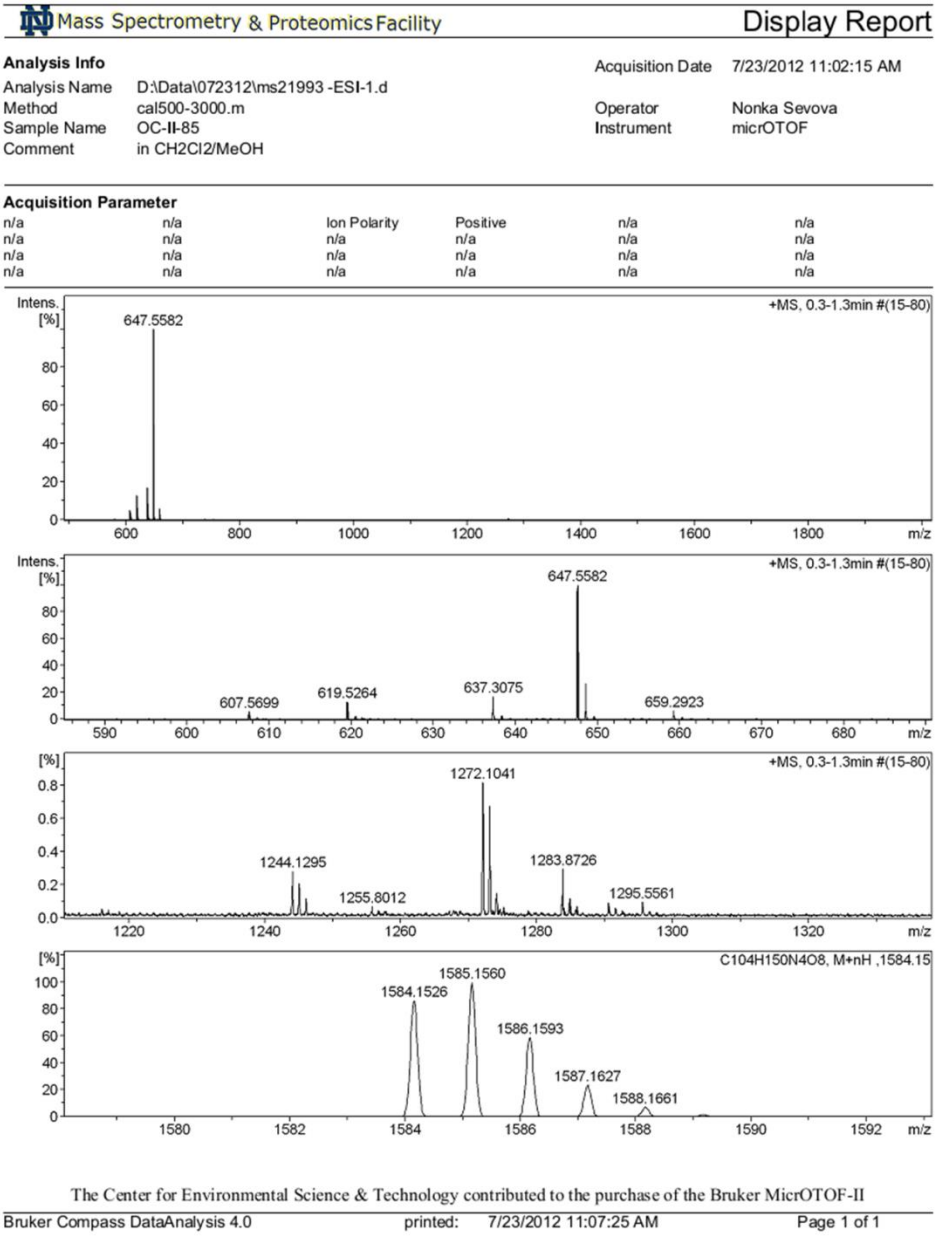

Figure D-2: HR-MS report for DBPD-8.

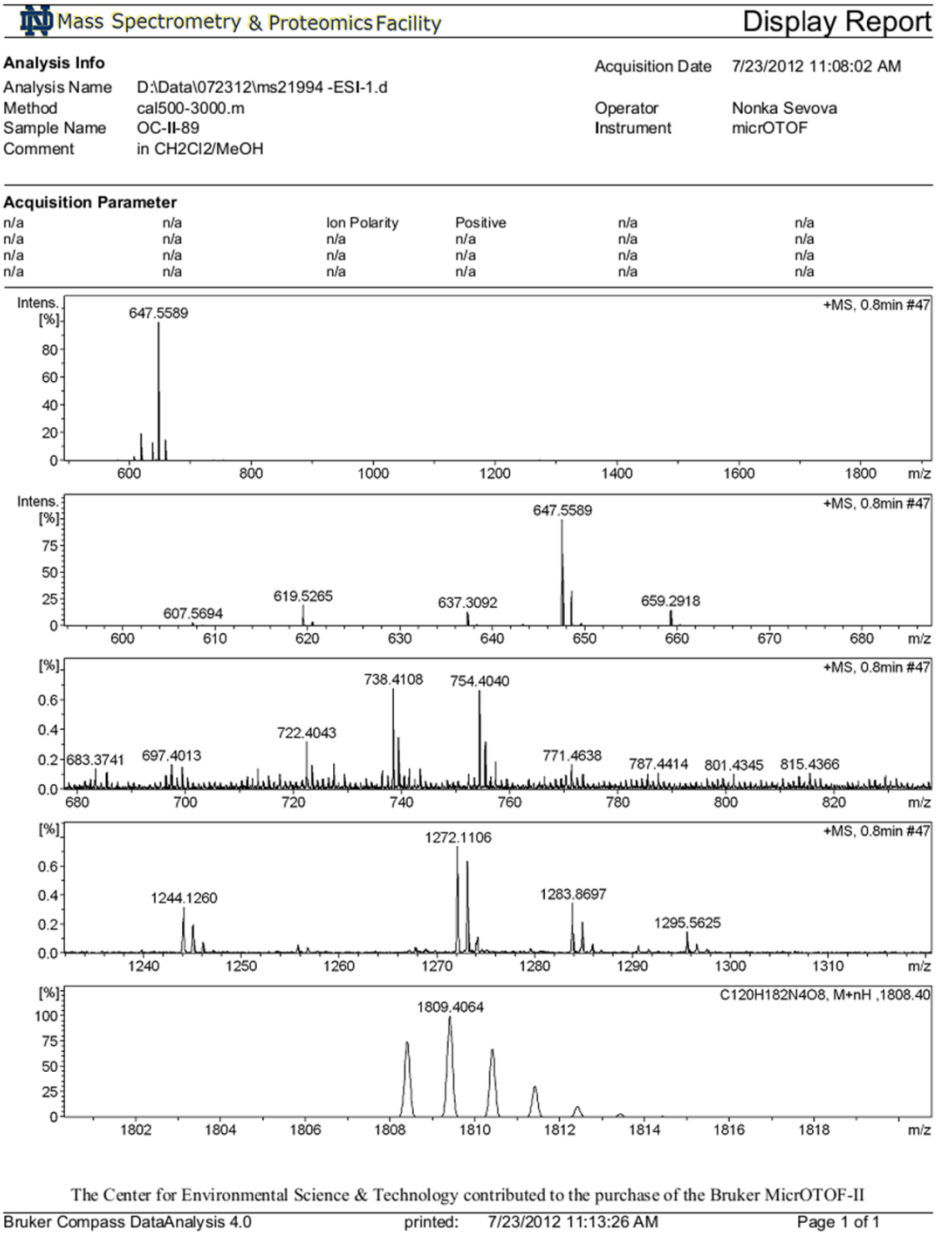

Figure D-3: HR-MS report for DBPD-10.

References

(1) Zumdahl, S. *Zumdahl Chemistry*; Houghton Mifflin, New York: , 2000; pp 451.

(2) Chang, R. *Chemistry*; McGrawHill Higher Education, New York: , 2006; pp 436.

(3) Kleman, M. *Acta. Crystallogr. Sect. A* **1981**, *37*, 607-608.

(4) Grigoriadis, C.; Haase, N.; Butt, H.-J.; Müllen, K. ; Floudas, G. *Adv. Mater.* **2010**, *22*, 1403-1406.

(5) Kelly, S. ; O'Neill, M. *Handbook of advanced electronic and photonic materials and devices*; Vol. 7 Academic Press Japan, Tokyo: , 2000; pp 2-66.

(6) Versnyder, F. I. ; Shank, M. *Mat. Sci. Eng.* **1970**, *6*, 213-247.

(7) Tschierske, C. *J. Mater. Chem.* **1998**, *8*, 1485-1508.

(8) Zhang, L.; Hughes, D. L. ; Cammidge, A. N. *J. Org. Chem.* **2012**, *77*, 4288-4297.

(9) Goodby, J. W.; Mehl, G. H.; Saez, I. M.; Tuffin, R. P.; Mackenzie, G.; Auzély-Velty, R.; Benvegnu, T. ; Plusquellec, D. *Chem. Comm.* **1998**, , 2057-2070.

(10) Pelzl, G.; Diele, S. ; Weissflog, W. *Adv. Mater.* **1999**, *11*, 707-724.

(11) Pelzl, G.; Wirth, I. ; Weissflog, W. *Liq. Cryst.* **2001**, *28*, 969-972.

(12) Lehmann, M. *Chem.-Eur. J.* **2009**, *15*, 3638-3651.

(13) Meier, H.; Lehmann, M.; Holst, H. ; Schwfppe, D. *Tetrahedron* **2004**, *60*, 6881-6888.

(14) Vosel, A. ; others *J. Chem. Soc., Chem. Commun.* **1990**, , 163-165.

(15) Yao, D. S.; Li, F.; Wang, H. J.; Li, X. Y.; Tian, M.; Zhou, A. J. ; Hu, J. S. *Adv. Mater. Res.* **2012**, *396*, 2202-2205.

(16) Belaissaoui, A.; Saez, I.; Cowling, S. ; Goodby, J. *Macromolecules* **2013**, *46*, 1268-1273.

(17) Marcos, M.; Martin-Rapún, R.; Omenat, A. ; Serrano, J. L. *Chem. Soc. Rev.* **2007**, *36*, 1889-1901.

(18) Chandrasekhar, S. *Liq. Cryst.* **1993**, *14*, 3-14.

(19) Sörensen, T. J.; Hildebrandt, C. B.; Elm, J.; Andreasen, J. W.; Madsen, A.; Westerlund, F. ; Laursen, B. W. *J. Mater. Chem.* **2012**, *22*, 4797-4805.

(20) Craats, A. v. d.; Warman, J.; Fechtenkцtter, A.; Brand, J. D.; Harbison, M. ; Müllen, K. *Adv. Mater.* **1999**, *11*, 1469-1472.

(21) D. W. Bruce, J. W. Goodby, J. R. Sambles and H. J. Coles, Introduction: New directions in liquid crystal science, *Philos. Trans. R. Soc. London, Ser. A*, 2006, **364**, 2567–2571.

(22) Geelhaar, T.; Griesar, K. ; Reckmann, B. *Angew. Chem., Int. Ed.* **2013**, Early View.

(23) Laschat, S.; Baro, A.; Steinke, N.; Giesselmann, F.; Hegele, C.; Scalia, G.; Judele, R.; Kapatsina, E.; Sauer, S.; Schreivogel, A. ; others *Angew. Chem., Int. Ed.* **2007**, *46*, 4832-4887.

(24) Sergeyev, S.; Pisula, W. ; Geerts, Y. H. *Chem. Soc. Rev.* **2007**, *36*, 1902-1929.

(25) An, Z.; Yu, J.; Jones, S. C.; Barlow, S.; Yoo, S.; Domercq, B.; Prins, P.; Siebbeles, L. D.; Kippelen, B. ; Marder, S. *Adv. Mater.* **2005**, *17*, 2580-2583.

(26) Tsivadze, A. Y.; Nosikova, L. ; Kudryashova, Z. *Prot. Met. Phys. Chem. Surf.* **2012**, *48*, 135-157.

(27) Bundgaard, E. ; Krebs, F. C. *Sol. Energy Mater. Sol. Cells* **2007**, *91*, 954-985.

(28) Scharber, M. C.; Mühlbacher, D.; Koppe, M.; Denk, P.; Waldauf, C.; Heeger, A. J. ; Brabec, C. J. *Adv. Mater.* **2006**, *18*, 789-794.

(29) Bushby, R. J. ; Lozman, O. R. *Curr. Opin. Solid State Mater. Sci.* **2002**, *6*, 569-578.

(30) O'Neill, M. ; Kelly, S. M. *Adv. Mater.* **2003**, *15*, 1135-1146.

(31) Hahm, S. G.; Ko, Y.-G.; Rho, Y.; Ahn, B. ; Ree, M. *Curr. Opin. Chem. Eng.* **2012**, 71-78.

(32) Gearba, R. I.; Anokhin, D. V.; Bondar, A. I.; Bras, W.; Jahr, M.; Lehmann, M. ; Ivanov, D. A. *Adv. Mater.* **2007**, *19*, 815-820.

(33) Grell, M.; Knoll, W.; Lupo, D.; Meisel, A.; Miteva, T.; Neher, D.; Nothofer, H.-G.; Scherf, U. ; Yasuda, A. *Adv. Mater.* **1999**, *11*, 671-675.

(34) Hara, M.; Nagano, S. ; Seki, T. *J. Am. Chem. Soc.* **2010**, *132*, 13654-13656.

(35) Herzog, H.; Meldon, J. ; Hatton, A. *Clean Air Task Force* **2009**, 1-39.

(36) Bara, J. E.; Camper, D. E.; Gin, D. L. ; Noble, R. D. *Acc. Chem. Res.* **2009**, *43*, 152-159.

(37) Oztek, M. T.; Hampton, M. D.; Slattery, D. K. ; Loucks, S. *Int. J. Hydrogen Energy* **2011**, *36*, 6705-6710.

(38) Yoshio, M.; Kagata, T.; Hoshino, K.; Mukai, T.; Ohno, H. ; Kato, T. *J. Am. Chem. Soc.* **2006**, *128*, 5570-5577.

(39) Chen, S. ; Eichhorn, S. H. *Isr. J. Chem.* **2012**, *52*, 830-843.

(40) Bobrovsky, A.; Mochalov, K.; Oleinikov, V. ; Shibaev, V. *Liq. Cryst.* **2011**, *38*, 737-742.

(41) Chen, S.; Katsis, D.; Schmid, A.; Mastrangelo, J.; Tsutsui, T. ; Blanton, T. *Nature* **1999**, *397*, 506-508.

(42) Meyer, C.; Luckhurst, G. ; Dozov, I. *Phys. Rev. Lett.* **2013**, *111*, 067801.

(43) Koizumi, N.; Shanker, G.; Araoka, F.; Ishikawa, K.; Yelamaggad, C. ; Takezoe, H. *NPG Asia Mater.* **2012**, *4*, e11.

(44) Nishikawa, H. ; Kawata, K. *J. Photopolym. Sci. Technol.* **2012**, *25*, 289-293.

(45) Granasy, L.; Pusztai, T.; Warren, J. A.; Douglas, J. F.; Bцrzsцnyi, T. ; Ferreiro, V. *Nat. Mater.* **2003**, *2*, 92-96.

(46) Libbrecht, K. G. A guide to snowflakes, 2013. SnowCrystals.com Your online guide to snowflakes, snow crystals, and other ice phenomena. http://www.its.caltech.edu/~atomic/snowcrystals/class/w050207a045.jpg (Accessed July 2013).

(47) Lepock, J. R.; Ritchie, K. P.; Kolios, M. C.; Rodahl, A. M.; Heinz, K. A. ; Kruuv, J. *Biochemistry* **1992**, *31*, 12706-12712.

(48) Lavigueur, C.; Foster, E. ; Williams, V. *J. Appl. Crystallogr.* **2008**, *41*, 214-216.

(49) Cademartiri, L.; Bishop, K. J.; Snyder, P. W. ; Ozin, G. A. *Philos. T. Roy. Soc. A* **2012**, *370*, 2824-2847.

(50) Blinov, L. M. *Structure and properties of liquid crystals*; Vol. 123 Springer: , 2011; pp 19-40.

(51) Allen, M.; Harris, K.; Kariuki, B.; Kumari, N.; Preece, J.; Diele, S.; Lose, D.; Hegmann, T. ; Tschierske, C. *Liq. Cryst.* **2000**, *27*, 689-692.

(52) Foster, E. J.; Jones, R. B.; Lavigueur, C. ; Williams, V. E. *J. Am. Chem. Soc.* **2006**, *128*, 8569-8574.

(53) Hylewska, E.; Kocot, A.; Merkel, K. ; Wrzalik, R. *Phase Transit.* **2012**, , 1-12.

(54) Michaux, F.; Stébé, M. ; Blin, J. *Microporous Mesoporous Mater.* **2012**, *151*, 201-210.

(55) Senyuk, B.; Evans, J. S.; Ackerman, P. J.; Lee, T.; Manna, P.; Vigderman, L.; Zubarev, E. R.; Lagemaat, J. v. d. ; Smalyukh, I. I. *Nano Lett.* **2012**, *12*, 955-963.

(56) Seo, J.; Kim, S.; Gihm, S. H.; Park, C. R. ; Park, S. Y. *J. Mater. Chem.* **2007**, *17*, 5052-5057.

(57) Tschierske, C. *J. Mater. Chem.* **2001**, *11*, 2647-2671.

(58) Davidson, P.; Levelut, A.; Strzelecka, H. ; Gionis, V. *J. Phys. Lett-Paris* **1983**, *44*, 823-828.

(59) Elliott, J. M.; Chipperfield, J. R.; Clark, S. ; Sinn, E. *Inorg. Chem.* **2001**, *40*, 6390-6396.

(60) Prasad, V.; Kang, S.-W.; Varshney, S. K. ; Nagaveni, N. *Liq. Cryst.* **2010**, *37*, 121-128.

(61) Norvez, S.; Tournilhac, F.-G.; Bassoul, P. ; Herson, P. *Chem. Mater.* **2001**, *13*, 2552-2561.

(62) Nguyen, H.-T.; Destrade, C. ; Malthécte, J. *Adv. Mater.* **1997**, *9*, 375-388.

(63) Grolik, J.; Dudek, Ł. ; Eilmes, J. *Tetrahedron Lett.* **2012**, *53*, 5127–5130.

(64) Kohmoto, S.; Mori, E. ; Kishikawa, K. *J. Am. Chem. Soc.* **2007**, *129*, 13364-13365.

(65) Bai, Y.-F.; Zhao, K.-Q.; Hu, P.; Wang, B.-Q. ; Redshaw, C. *Curr. Org. Chem.* **2013**, *17*, 871-885.

(66) Lee, J. H.; Jang, I.; Hwang, S. H.; Lee, S. J.; Yoo, S. H. ; Jho, J. Y. *Liq. Cryst.* **2012**, *39*, 973-981.

(67) Wang, Y.; Yoon, H. G.; Bisoyi, H. K.; Kumar, S. ; Li, Q. *J. Mater. Chem.* **2012**, *22*, 20363-20367.

(68) Zhang, L.; Gopee, H.; Hughes, D. L. ; Cammidge, A. N. *Chem. Comm.* **2010**, *46*, 4255-4257.

(69) Kumar, S. ; Naidu, J. *Liq. Cryst.* **2002**, *29*, 899-906.

(70) Kumar, S. ; Varshney, S. *Org. Lett.* **2002**, *4*, 157-159.

(71) Heravi, M. M.; Bakhtiari, K.; Tehrani, M. H.; Javadi, N. M. ; Oskooie, H. A. *Arkivoc* **2006**, *16*, 16-22.

(72) Satam, V.; Harad, A.; Rajule, R. ; Pati, H. *Tetrahedron* **2010**, *66*, 7659-7706.

(73) Nguyen, H.; Babeau, A.; Léon, C.; Marcerou, J.-P.; Destrade, C.; Soldera, A.; Guillon, D. ; Skoulios, A. *Liq. Cryst.* **1991**, *9*, 253-266.

(74) Takagi, Y.; Ohta, K.; Shimosugi, S.; Fujii, T. ; Itoh, E. *J. Mater. Chem.* **2012**, *22*, 14418-14425.

(75) Ban, K.; Nishizawa, K.; Ohta, K.; van de Craats, A. M.; Warman, J. M.; Yamamoto, I. ; Shirai, H. *J. Mater. Chem.* **2001**, *11*, 321-331.

(76) Tanaka, S.; Sakurai, T.; Honsho, Y.; Saeki, A.; Seki, S.; Kato, K.; Takata, M.; Osuka, A. ; Aida, T. *Chem.-Eur. J.* **2012**, *18*, 10554-10561.

(77) Alam, M.; Motoyanagi, J.; Yamamoto, Y.; Fukushima, T.; Kim, J.; Kato, K.; Takata, M.; Saeki, A.; Seki, S.; Tagawa, S. ; others *J. Am. Chem. Soc.* **2009**, *131*, 17722-17723.

(78) Choi, J.-W.; Ryu, M.-H.; Lee, E. ; Cho, B.-K. *Chem. Eur. J.* **2010**, *16*, 9006-9009.

(79) Kendhale, A. M.; Schenning, A. P. ; Debije, M. G. *J. Mater. Chem. A* **2013**, *1*, 229-232.

(80) Wang, T.-J.; Yang, S.-C.; Chen, T.-J. ; Chen, B.-Y. *Opt. Express* **2012**, *20*, 15853-15858.

(81) Zhang, Y.; Ortega, J.; Baumeister, U.; Folcia, C. L.; Sanz-Enguita, G.; Walker, C.; Rodriguez-Conde, S.; Etxebarria, J.; O'Callaghan, M. J. ; More, K. *J. Am. Chem. Soc.* **2012**, *134*, 16298-16306.

(82) Miyajima, D.; Araoka, F.; Takezoe, H.; Kim, J.; Kato, K.; Takata, M. ; Aida, T. *J. Am. Chem. Soc.* **2010**, *132*, 8530-8531.

(83) Fitie, C.; Roelofs, W.; Kemerink, M. ; Sijbesma, R. *J. Am. Chem. Soc.* **2010**, *132*, 6892-6893.

(84) Kumar, S. *Chemistry of discotic liquid crystals: from monomers to polymers*; Taylor & Francis: US, 2010; pp. 18-28.

(85) Vaupotic, N.; Pociecha, D. ; Gorecka, E. *Polar and apolar columnar phases made of bent-core mesogens*; Springer: , 2012; pp 281-302.

(86) Trzaska, S. T.; Zheng, H. ; Swager, T. M. *Chem. Mater.* **1999**, *11*, 130-134.

(87) Koizumi, N.; Shanker, G.; Araoka, F.; Ishikawa, K.; Yelamaggad, C. ; Takezoe, H. *NPG Asia Mater.* **2012**, *4*, e11.

(88) Bai, B.; Zhao, C.; Wang, H.; Ran, X.; Wang, D. ; Li, M. *Mater. Chem. Phys.* **2012**, *133*, 232-238.

(89) Chen, L.; Zhong, K.-L.; Jin, L. Y.; Huang, Z.; Liu, L. ; Hirst, L. S. *Macromol. Res.* **2010**, *18*, 800-805.

(90) Trzaska, S. T. ; Swager, T. M. *Chem. Mater.* **1998**, *10*, 438-443.

(91) Almenningen, A.; Bastiansen, O.; Fernholt, L.; Cyvin, B. N.; Cyvin, S. J. ; Samdal, S. *J. Mol. Struct.* **1985**, *128*, 59-76.

(92) Dorofeeva, O. V.; Moiseeva, N. F.; Yungman, V. S. ; Novikov, V. P. *Thermochim. Acta* **2001**, *374*, 7-11.

(93) Field, L. D. ; Sternhell, S. *J. Am. Chem. Soc.* **1981**, *103*, 738-741.

(94) Bisoyi, H. ; Kumar, S. *Chem. Soc. Rev.* **2010**, *39*, 264-285.

(95) Kumar, S. *Chemistry of discotic liquid crystals: from monomers to polymers*; Taylor & Francis: US, 2010; pp 370-376

(96) Voisin, E.; Johan Foster, E.; Rakotomalala, M. ; Williams, V. E. *Chem. Mater.* **2009**, *21*, 3251-3261.

(97) Foster, E. J.; Babuin, J.; Nguyen, N. ; Williams, V. E. *Chem. Comm.* **2004**, , 2052-2053.

(98) Mohr, B.; Enkelmann, V. ; Wegner, G. *J. Org. Chem.* **1994**, *59*, 635-638.

(99) Lavigueur, C.; Foster, E. J. ; Williams, V. E. *J. Am. Chem. Soc.* **2008**, *130*, 11791-11800.

(100) Iqbal, J.; Bhatia, B. ; Nayyar, N. K. *Chem. Rev.* **1994**, *94*, 519-564.

(101) Bruice, P. *Organic Chemistry*, 3rd ed.; Prentice Hall: New York, 2010; pp 712-713.

(102) Jones, M. ; Fleming, S. *Organic Chemistry*, 6th ed.; W W Norton and Company Incorporated: New York, 2003; pp 1036-1037.

(103) Al-Lawati, Z. H.; Bushby, R. J. ; Evans, S. D. *J. Phys. Chem. C* **2013**, *117*, 7533-7539.

(104) Li, Q. *Liquid Crystals Beyond Displays: Chemistry, Physics, and Applications*; John Wiley & Sons: US, 2012; pp 29-82.

(105) Ariyoshi, M.; Sugibayashi-Kajita, M.; Suzuki-Ichihara, A.; Kato, T.; Kamei, T.; Itoh, E. ; Ohta, K. *J. Porphyrins Phthalocyanines* **2012**, *16*, 1114-1123.

(106) Shimogaki, T.; Dei, S.; Ohta, K. ; Matsumoto, A. *J. Mater. Chem.* **2011**, *21*, 10730-10737.

(107) Ba, C.-Y.; Shen, Z.-R.; Gu, H.-W.; Guo, G.-Q.; Xie, P.; Zhang, R.-B.; Zhu, C.-F.; Wan, L.-J.; Li, F.-Y. ; Huang, C.-H. *Liq. Cryst.* **2003**, *30*, 391-397.

(108) Zhang, J. ; Moore, J. S. *J. Am. Chem. Soc.* **1994**, *116*, 2655-2656.

(109) Percec, V.; Peterca, M.; Tadjiev, T.; Zeng, X.; Ungar, G.; Leowanawat, P.; Aqad, E.; Imam, M. R.; Rosen, B. M.; Akbey, U. ; others *J. Am. Chem. Soc.* **2011**, *133*, 12197-12219.

(110) Jung, H.-T.; Kim, S.; Ko, Y.; Yoon, D.; Hudson, S.; Percec, V.; Holerca, M.; Cho, W.-D. ; Mosier, P. *Macromolecules* **2002**, *35*, 3717-3721.

(111) Lin, W.-H.; Chang, Y.; Liao, C.-T.; Tai, H.-S. ; Lee, J.-Y. *J. Chin. Inst. Eng.* **2013**, *36*, 391-398.